

CHARACTERIZATION AND REACTIVITY STUDIES FOR CHEMICAL LOOP  
GASIFICATION OF HIGH SULFUR LIGNITES

A THESIS SUBMITTED TO  
THE GRADUATE SCHOOL OF NATURAL AND APPLIED SCIENCES  
OF  
MIDDLE EAST TECHNICAL UNIVERSITY

BY

ARZU KANCA

IN PARTIAL FULFILLMENT OF THE REQUIREMENTS  
FOR  
THE DEGREE OF DOCTOR OF PHILOSOPHY  
IN  
CHEMICAL ENGINEERING

OCTOBER 2013



Approval of the thesis:

**CHARACTERIZATION AND REACTIVITY STUDIES FOR CHEMICAL  
LOOP GASIFICATION OF HIGH SULFUR LIGNITES**

submitted by **ARZU KANCA** in partial fulfillment of the requirements for the degree of  
**Doctor of Philosophy in Chemical Engineering Department**, Middle East Technical  
University by,

Prof. Dr. Canan Özgen  
Dean, Graduate School of Natural and Applied Sciences -----

Prof. Dr. Deniz Üner  
Head of Department, **Chemical Engineering** -----

Prof. Dr. Deniz Üner  
Supervisor, Chemical Engineering Dept., METU -----

Examining Committee Members:  
Prof. Dr. Hayrettin Yücel -----  
Chemical Engineering Dept., METU

Prof. Dr. Deniz Üner -----  
Chemical Engineering Dept., METU

Assoc.Prof. Dr. Sena Yaşyerli -----  
Chemical Engineering Dept., Gazi University

Prof. Dr. Jeffrey A. Reimer -----  
Chemical and Biomolecular Eng. Dept., University of California  
Berkeley

Prof. Dr. İnci Eroğlu -----  
Chemical Engineering Dept., METU

Date: 04 October 2013

**I hereby declare that all information in this document has been obtained and presented in accordance with academic rules and ethical conduct. I also declare that, as required by these rules and conduct, I have fully cited and referenced all material and results that are not original to this work.**

**Name, Last name: Arzu, Kanca**  
**Signature:**

## ABSTRACT

### CHARACTERIZATION AND REACTIVITY STUDIES FOR CHEMICAL LOOP GASIFICATION OF HIGH SULFUR LIGNITES

Kanca, Arzu

Ph.D., Department of Chemical Engineering  
Supervisor: Prof.Dr. Deniz Üner

October 2013, 130 pages

The objective of this study was to characterize and to determine the gasification reactivity of Tuncbilek lignites. The ultimate analysis of Tuncbilek lignite revealed that the elemental composition is 37.7% C, 3.6% H, 1.6% N, and 5.4% S, while the proximate analysis indicated  $4.7 \pm 0.9\%$  moisture  $27.9 \pm 0.1\%$  volatiles and  $37.9 \pm 0.2\%$  ash. In this context, four different reactions during gasification namely, pyrolysis, oxidation, hydrogenation, and wet air oxidation were investigated separately. Carbon residues of all these processes were analyzed by XRD, DRIFTS, and  $^1\text{H}$  and  $^{13}\text{C}$  (CP) NMR spectroscopy in order to associate between chemical structure and reactivity. A semi-batch reactor system was used for pyrolysis, oxidation, and hydrogenation experiments, while a high-pressure batch reactor was used for wet air oxidation experiments. Pyrolysis and oxidation experiments revealed that carbon conversion of Tuncbilek lignite is quite high in the presence of oxygen. In addition, hydrogenation experiments displayed that the sulfur removal is the most efficient in the presence of gas phase hydrogen. On the other hand, desulfurization yield of wet air oxidation reaction at 5 bar and  $150^\circ\text{C}$ , was lower than hydrodesulfurization yields. The results of the experiments indicated that high pressure and temperature are necessary to enhance the yield.

Co and Pb based pure and mixed metal oxides were investigated as oxygen source and sulfur trapping agents for chemical looping systems. The oxygen transfer potential of Co-Pb metal oxides was monitored by TGA and the maximum weight loss was recorded when coal to metal oxide ratio is higher than 1. Additionally, XRD revealed sulfur capturing ability of these oxides during both pyrolysis and oxidation processes. A process flow diagram is proposed to utilize the mixed metal oxides as chemical looping agents for oxygen and sulfur transfer.

Keywords: Coal characterization, coal gasification, chemical looping process, desulfurization, hydrothermal desulfurization, and high sulfur lignite.

## ÖZ

# YÜKSEK KÜKÜRT İÇEREN LİNYİTLERİN KİMYASAL ÇEMBER GAZLAŞTIRMA SÜREÇLERİ İÇİN SINIFLANDIRMA VE TEPKİME TESTLERİ

Kanca, Arzu

Doktora, Kimya Mühendisliği Bölümü  
Tez Yöneticisi: Prof.Dr. Deniz Üner

Ekim 2013, 130 sayfa

Bu çalışmada, Tunçbilek linyitlerinin karakterize edilmesi ve bu linyitlerin gazlaştırma aktivitelerinin belirlenmesi amaçlanmıştır. Elementel analiz yöntemi, Tunçbilek linyitlerinin bileşiminin %37.7 C, %3.6 H, %1.6 N ve %5.4 S olduğunu ortaya koyarken proksimet analiz, %4.7 ± 0.9 nem, %27.9 ± 0.1 uçucu madde ve %37.9 ± 0.2 kül oranlarını göstermiştir. Bu kapsamda gazlaştırma sürecinde gerçekleşen dört farklı tepkime (piroliz, oksidasyon, hidrojenasyon, ve ıslak hava oksidasyonu) ayrı ayrı ele alınmıştır. Reaksiyon testleri sonrası arta kalan katı numunelerin XRD, DRIFTS, ve <sup>1</sup>H ve <sup>13</sup>C (CP) NMR gibi spektroskopik yöntemler kullanılarak analiz edilmesi, linyitin yapısı ve reaktivitesi arasında bir bağlantı kurulmasını mümkün hale getirmiştir. Yarı kesikli reaktör sistemi piroliz, oksidasyon ve hidrojenasyon deneyleri için kullanılmıştır. Islak hava oksidasyon deneyleri ise yüksek basınçlı kapalı reaktör sisteminde yapılmıştır. Piroliz ve oksidasyon deneyleri Tunçbilek linyitinin carbon dönüşümlerinin oksijen varlığında yüksek olduğunu ortaya koymuştur. Buna ilaveten, hidrojenleme deneyleri linyit yapısında var olan kükürtü en verimli uzaklaştırmanın hidrojen gazı varlığında mümkün olduğunu göstermektedir. Öte yandan yaklaşık 5 bar ve 150°C’de gerçekleştirilen ıslak hava oksidasyon reaksiyonunun sülfürü uzaklaştırma verimi hidrojenasyondan daha azdır. Bu reaksiyonun verimini artırmak için daha yüksek basınç ve sıcaklık şartları gerekmektedir. Co ve Pb kaynaklı saf ve karışık metal oksitleri kimyasal çember gazlaştırma sistemlerinde oksijen kaynağı ve aynı zamanda kükürt tutucu olarak kullanılabilmesi incelenmiştir. Co-Pb metal oksitlerinin oksijen transfer potansiyeli TGA ile izlenmiş ve analiz sonuçları kömür metal-oksit oranının 1’den küçük olduğu durumda kütle kaybının maksimum olduğunu ortaya koymuştur. Ek olarak, XRD sonuçları Co-Pb metal oksitlerin piroliz ve oksidasyon sırasında kükürt tutma becerilerini göstermektedir. Bu malzemelerin kimyasal çember sisteminde oksijen ve kükürt tranferi için kullanılabilmesini göstermek için bir akış şeması önerilmektedir.

Anahtar Kelimeler: Kömür sınıflandırma, kömür gazlaştırma, kimyasal çember süreci, desülfürizasyon, hidrotermal desülfürizasyon ve yüksek kükürtlü linyit.

*To my mum and dad Aynur & Adnan Kanca*

*and*

*To brothers Aytunç, Alper, and Ahmet Kanca*

## ACKNOWLEDGMENTS

I would like to express my deepest gratitude to my supervisor Prof. Dr. Deniz Üner for her patience, guidance, support, and valuable comments throughout the thesis study. Her guidance motivated me in all the phases of the study.

I am grateful to my thesis examining committee members, Assoc. Prof. Dr. Sena Yaşyerli, and Prof. Dr. Hayrettin Yücel, for their valuable discussions.

I sincerely appreciate Prof. Dr. Jeffrey A. Reimer and his family for their support and interest. Also I would like to thank Reimer group members for their help and friendship.

I would like thank to all staff of METU-Chemical Engineering Department, especially thanks to Turgut Aksakal for the proximate and Eschka analyses of coal samples, Yavuz Güngör for XRD, Mihrican Açıkgoz for TGA measurements, Gülten Orakçı for GC guideline, Kerime Güney for AAS, and other stuffs İsa Çağlar, Adil Demir, Ertuğrul Özdemir, Süleyman Kuşhan, Kemal Yıldırım. I am also grateful to Özlem Güven Pak, Naciye Kaya, and Gülüstan Görmez.

I would like to thank to METU Central Laboratory for Raman and Ultimate Analyses. Special thanks to Hikmet Eren, Merve Cengiz, and Dr. Elif Ünsal.

I thank to Cactus research group members for their valuable discussions, help, and friendship. Başar Çağlar, Dr. Osman Karşlıoğlu, Orçun Ergün, Dr. Mert Mehmet Oymak, Bahar İpek, Dr. Mukaddes Can, Hale Ay, Mustafa Yasin Aslan, Atalay Çalışan, İbrahim Bayar, Nevzat Can Aksu, Necip Berker Üner, for their kind friendships. I am also grateful to Özgen Yalçın, İlker Tezsevin, and Gökçe Avcıoğlu, for their valuable friendship and their help.

I am thankful to Lale Tüzün, Seher and Kürşat Arslan for their emotional support, patience, and friendship.

I am grateful to my sisters Dr. Hatice Ceylan, Dr. Işık Haykır and Dr. Vahideh Angardi for their endless support and friendship.

Special thanks to my dear cousins Pervin and Osman Demir for their continuous support, guidance, and love. They became my parents in Ankara.

Last but certainly not least, my deepest love and thank to my family, who always supports me spiritually. I felt them near to me even we were apart.

I would like to acknowledge METU – Atatürk University and Turkish SPO support for this project was granted through ÖYP program and Tubitak for travel grant.

## TABLE OF CONTENTS

ABSTRACT .....	v
ÖZ.....	vi
ACKNOWLEDGMENTS .....	viii
TABLE OF CONTENTS.....	ix
LIST OF TABLES.....	xiii
LIST OF FIGURES .....	xiv
CHAPTER 1 .....	1
INTRODUCTION .....	1
1.1 Background.....	1
1.1.1 Coal petrography .....	3
1.1.2 Worldwide coal reserves.....	4
1.1.3 About coal in Turkey.....	5
1.2 Motivation.....	6
1.3 Objectives .....	6
1.4 Summary of the study .....	7
CHAPTER 2 .....	9
LITERATURE SURVEY .....	9
2.1 Gasification .....	9
2.2 Types of gasifiers.....	12
2.2.1 Fixed-bed (or Moving-bed) gasifier.....	12
2.2.2 Fluidized-bed gasifier.....	12
2.2.3 Entrained-bed gasifier .....	13
2.2.4 Molten-bed gasifier.....	14
2.3 Main processes taking place during gasification .....	14
2.3.1 Coal drying and pyrolysis .....	14
2.3.2 Coal oxidation .....	16
2.3.3 Catalyst utilization for coal gasification.....	18
2.3.5 Catalyst utilization during the substituted natural gas production.....	19
2.3.4 Coal liquefaction and/or hydrogenation.....	21
CHAPTER 3 .....	25
EXPERIMENTAL STUDIES .....	25
3.1. Introduction .....	25

3.2. Coal Preparation and Characterization .....	25
3.2.1 Preparation of coal samples .....	25
3.2.2 Classical coal analysis .....	26
3.2.2.1 Proximate Analysis .....	26
3.2.2.2 Ultimate Analysis .....	26
3.2.2.3 Sulfur Determination with Eschka Analysis.....	26
3.2.2.4 Pyritic, Sulfate and Organic Sulfur Analysis .....	27
3.2.2.5 Calorific Value Calculation (ASTM D-2015) .....	28
3.2.3 Volatiles and ash analyses by TGA .....	28
3.2.4 Analysis of Inorganic structure by XRF .....	28
3.2.5 Monitoring of inorganic structure by XRD .....	28
3.2.6 DRIFT spectroscopy .....	29
3.2.7 NMR spectroscopy .....	29
3.3 Coal Processes Methodology.....	29
3.3.1 Pyrolysis and Oxidation Experiments .....	29
3.3.2 Hydrogenation Experiments.....	29
3.3.3 Wet Air Oxidation Experiments .....	33
<b>CHAPTER 4 .....</b>	<b>35</b>
<b>CHARACTERIZATION OF TUNCBILEK LIGNITES.....</b>	<b>35</b>
4.1. Introduction.....	35
4.2 Results and Discussions .....	36
4.2.1 Classical Coal Characterizations-Proximate and Ultimate Analyses .....	36
4.2.2 Thermal Gravimetric Analysis TGA analysis under N <sub>2</sub> and air flow .....	38
4.2.3 XRF .....	39
4.2.4 XRD .....	40
4.2.5 DRIFTS.....	41
4.2.6 Proton ( <sup>1</sup> H) and Carbon ( <sup>13</sup> C) NMR spectroscopy .....	44
4.3 Conclusions .....	45
<b>CHAPTER 5 .....</b>	<b>47</b>
<b>GASIFICATION AND DESULFURIZATION REACTIVITY OF TUNCBILEK LIGNITE.....</b>	<b>47</b>
5.1 Introduction.....	47
5.1.1 Gasification reactivity .....	47
5.1.2 Desulfurization reactivity.....	48
5.2 Results and Discussion.....	49
5.2.1 Pyrolysis Experiments .....	49
5.2.1.1 Gaseous products during the pyrolysis process.....	49
5.2.1.2 XRD for pyrolysis residue .....	51

5.2.1.3 DRIFTS for pyrolysis residue .....	52
5.2.1.4 <sup>1</sup> H NMR and <sup>13</sup> C (CP) MAS-NMR characterization of pyrolysis residue .....	53
5.2.2 Oxidation Experiments .....	55
5.2.2.1 Gas Analysis .....	55
5.3.2.2 XRD for oxidation residue .....	57
5.3.2.3 DRIFTS for oxidation residue .....	59
5.3.2.4 <sup>1</sup> H and <sup>13</sup> C (CP) MAS-NMR characterization of oxidation residue .....	60
5.3.3 Hydrogenation Experiments .....	60
5.3.3.1 Elemental Analysis .....	60
5.3.3.2 XRD for hydrogenation residue .....	62
5.3.3.3 DRIFTS for hydrogenation residue .....	64
5.3.3.4 <sup>1</sup> H and <sup>13</sup> C (CP) MAS-NMR characterization of hydrogenation residue .....	65
5.3.3.6 Comparison of the residue of pyrolysis, oxidation, and hydrogenation processes	68
5.3.4 Hydrothermal Desulfurization (Wet Air Oxidation) Experiments .....	71
5.3.4.1 Elemental Analysis .....	71
5.4 Conclusions .....	77
<b>CHAPTER 6 .....</b>	<b>79</b>
<b>UTILIZATION of Co-Pb METAL OXIDES AS OXYGEN CARRIER IN CHEMICAL LOOPING COMBUSTION .....</b>	<b>79</b>
6.1 Introduction .....	79
6.2 Materials and Methods .....	83
6.2.1 Preparation of Co-Pb individual and mixed metal oxides .....	83
6.2.2 Characterization of Co-Pb individual and mixed metal oxides .....	84
6.3 Results and Discussion .....	84
6.3.1 Oxidation and Reduction thermodynamics of Co-Pb metal oxides .....	84
6.3.2 TGA experiments under inert atmosphere in various amount of Co-Pb metal oxide.	87
6.3.2 Characterization of Co-Pb metal oxides .....	87
6.3.2.1 XRD patterns of Co-Pb metal oxides .....	87
6.3.2.2 Raman spectra of Co-Pb metal oxides .....	88
6.3.2.3 <sup>207</sup> Pb MAS-NMR spectra of Co-Pb metal oxides .....	89
6.3.3 Gasification performance of individual Co and Pb oxides and Co-Pb mixed metal oxides .....	92
6.3.3.1 CH <sub>4</sub> and H <sub>2</sub> production under N <sub>2</sub> flow in the presence of Co-Pb individual and mixed metal oxides .....	92
6.3.3.2 CH <sub>4</sub> and H <sub>2</sub> production under air flow in the presence of Co-Pb individual and mixed metal oxides .....	96
6.3.4 Pb-based materials for sulfur recovery .....	100
6.4 Conclusions .....	103
<b>CHAPTER 7 .....</b>	<b>105</b>

DISCUSSION AND CONCLUSIONS .....	105
REFERENCES .....	109
APPENDIX A .....	119
STANDARD GIBBS FREE ENERGY OF FORMATION DATA FOR RELEVANT COMPOUNDS .....	119
APPENDIX B .....	121
MASS TRANSFER EFFECT .....	121
B.1. Pore diffusion effects: Constant N <sub>2</sub> flow rate v=200 cc/min .....	121
B.2. External mass transfer effects .....	122
APPENDIX C .....	123
CURVE FITTING .....	123
APPENDIX D .....	124
<sup>207</sup> Pb-NMR SPECTROSCOPY .....	124
<sup>207</sup> Pb MAS-NMR for the Determination of the Pulse Width and Spin-Lattice Relaxation Time .....	124
APPENDIX E .....	125
SAMPLE CALCULATION FOR SULFUR COMPOSITION .....	125
APPENDIX F .....	127
SAMPLE CALCULATION FOR CARBON CONVERSION .....	127
CURRICULUM VITAE .....	128

## LIST OF TABLES

### TABLES

Table 1.1. Mineral matter free basis humid coal composition (Kirk-Othmer, 2002a).....	4
Table 1.2. Nitrogen and sulfur compounds of coal (Spitz, 2004). .....	4
Table 2.1. Exothermic and endothermic reactions during gasification (Kabe et al., 2004b). .....	10
Table 2.2. Steam gasification reactions (Nahas, 1983).....	20
Table 4.1. Coal composition from the proximate analysis on air dried basis. ....	37
Table 4.2. Sulfur composition of coal determined by Eschka analysis on air-dried basis. ....	37
Table 4.3. Coal composition from the ultimate analysis on air-dried basis. ....	37
Table 4.4. Inorganic composition of coal determined by XRF.....	39
Table 4.5. Characteristic peak positions of coal inorganic components. ....	41
Table 4.6. Absorption bands of coal compounds. ....	43
Table 5.1. The reactions taking place during coal gasification and their thermochemical data (Molina and Mondragon, 1998, Barin, 1989).....	48
Table 5.2. Total amount of CH <sub>4</sub> and H <sub>2</sub> obtained during pyrolysis.....	51
Table 5.3. Carbon products and conversion of coal during pyrolysis. ....	51
Table 5.4. Total amount of CH <sub>4</sub> and H <sub>2</sub> under air flow. ....	57
Table 5.5. Total carbon conversion under air flow.....	57
Table 5.6. Possible Bragg angle values of coal inorganics.....	58
Table 5.7. Sulfur removal percentages determined by elemental analysis results. ....	61
Table 5.8. Bragg angle values of some components. ....	63
Table 5.9a. Total sulfur composition and heating value of wet air oxidation products.....	72
Table 5.9b. Pyritic sulfur composition of solid residue and -SO <sub>4</sub> <sup>=</sup> composition of solid and liquid residues.....	72
Table 5.10a. O <sub>2</sub> partial pressure effects at 150°C and in the presence of 50 cc water.....	73
Table 5.10b. O <sub>2</sub> partial pressure effect on pyritic sulfur and sulfate composition. ....	74
Table 5.11a. Temperature effect at 5 bar and in the presence of 50 cc water. ....	75
Table 5.11b. Temperature effect at 5 bar and in the presence of 50 cc water. ....	75
Table 5.12. Repetition experiments at 150°C and 5 bar.....	76
Table 6.1. Characteristic Raman shifts of Co <sub>3</sub> O <sub>4</sub> and PbO.....	88
Table 6.2. Total amount of CH <sub>4</sub> and H <sub>2</sub> formed under N <sub>2</sub> flow. ....	95
Table 6.3. Total carbon conversion under N <sub>2</sub> flow.....	96
Table 6.4. Total amount of CH <sub>4</sub> and H <sub>2</sub> formed under air flow. ....	99
Table 6.5. Total carbon conversion under air flow.....	100
Table A.1. Standard Gibbs free energy of formation CoO, CO, H <sub>2</sub> O, CO <sub>2</sub> , and PbO.....	119
(Journal of Physical Chemistry Reference Data) .....	119
Table A.2. Standard Gibbs free energy of formation of SO <sub>3</sub> , SO <sub>2</sub> , and PbS. ....	120
(Journal of Physical Chemistry Reference Data) .....	120

## LIST OF FIGURES

### FIGURES

Figure 1.1. Schematic diagram of coal gasification processes for electricity, hydrogen, liquid fuel production (Fan et al., 2008). .....	2
Figure 1.2. Global distribution of coal reserves (Gue, 2012). .....	5
Figure 1.3. Coal resources locations in Turkey (EUROCOAL, European Association for Coal and Lignite). .....	6
Figure 2.1. Regional distribution of operating, constructing and planning gasification plant capacity of the world (NETL, 2010). .....	11
Figure 2.2. Technology distribution of gasification (NETL, 2010). .....	11
Figure 2.3. Fixed-bed gasifier (van Dyk et al., 2006). .....	12
Figure 2.4. Fluidized-bed gasifier (Maurstad, 2005). .....	13
Figure 2.5. Entrained-bed gasifier (Kabe et al., 2004a). .....	13
Figure 2.6. Molten-bed gasifier (Kabe et al., 2004a). .....	14
Figure 2.7. Coal molecular structure simulation (Veras, 2002). .....	16
Figure 2.8. Particle size effect on the reaction regime (Wang, 2003) .....	17
Figure 2.9. Exxon Catalytic Coal Gasification Process flowchart (Nahas, 1983). .....	21
Figure 3.1. Schematic representation of experimental set up for pyrolysis and oxidation reaction tests. ....	31
Figure 3.2. Schematic representation of experimental set up for hydrogenation reaction tests. ....	32
Figure 3.3. Schematic representation of experimental set up for oxy-desulfurization reaction tests. ....	34
Figure 4.1. TGA and DTG curves of coal sample under N <sub>2</sub> flow. Solid line represents the TGA, while dotted line represents the DTG. ....	38
Figure 4.2. TGA and DTG curves of coal sample under air flow. Solid line represents the TGA, while dotted line represents the DTG. ....	39
Figure 4.3. XRD pattern of Tuncbilek lignite. ....	40
Figure 4.4. DRIFT spectrum of Tuncbilek lignite. ....	42
Figure 4.5. Proton NMR spectrum of Tuncbilek lignite. ....	44
Figure 4.6. Carbon NMR spectrum of Tuncbilek lignite. ....	45
Figure 5.1. CH <sub>4</sub> formation rates (a) and H <sub>2</sub> formation rates (b) under N <sub>2</sub> flow. ....	50
Figure 5.2. XRD pattern of unprocessed lignite and its pyrolysis residue. ....	52
Figure 5.3. DRIFT spectra of coal and its pyrolysis residue. ....	53
Figure 5.4. <sup>1</sup> H NMR spectra of unprocessed lignite and its pyrolysis residue. ....	54
Figure 5.5. Aliphatic, aromatic and C=O double bond traces of unprocessed lignite and lignite residue after pyrolysis. ....	55
Figure 5.6. CH <sub>4</sub> formation rates (a) and H <sub>2</sub> formation rates (b) under air flow. ....	56
Figure 5.7. XRD patterns of unprocessed lignite and its oxidation residue. ....	58
Figure 5.8. DRIFTS spectra of unprocessed lignite and its oxidation residue. ....	59
Figure 5.9. <sup>1</sup> H NMR spectra of unprocessed lignite and its oxidation residue. ....	60
Figure 5.10. Sulfur removal percentages of Tuncbilek lignite vs. hydrogen partial pressure. ....	61
Figure 5.11. X-ray patterns of unprocessed lignite and its hydrogenation residue. ....	62
Figure 5.12. XRD pattern of commercial PbO after hydrogenation experiment. ....	63
Figure 5.13. XRD pattern of commercial ZnO after hydrogenation experiment. ....	64
Figure 5.14. DRIFT spectra of unprocessed lignite and its hydrogenation residue. ....	65
Figure 5.15. <sup>1</sup> H NMR spectra of the unprocessed lignite and hydrogenated solid coal residue. ....	66

Figure 5.16. <sup>1</sup> H NMR spectra of the unprocessed lignite and hydrogenated liquid coal residue. ....	67
Figure 5.17. <sup>13</sup> C NMR spectra of the unprocessed lignite and hydrogenated liquid coal residue. ...	67
Figure 5.18. XRD patterns of (a) unprocessed lignite, (b) coal sample residue after pyrolysis, (c) coal sample residue after oxidation, (d) coal sample residue after hydrogenation Tuncbilek lignite. ....	68
Figure 5.19. DRIFT spectra of (a) coal samples, (b) coal sample residue after pyrolysis, (c) coal sample residue after oxidation, (d) coal sample residue after hydrogenation Tuncbilek lignite. ....	69
Figure 5.20. <sup>1</sup> H MAS NMR spectra of (a) coal samples, (b) coal sample residue after pyrolysis, (c) coal sample residue after oxidation, (d) coal sample residue after hydrogenation Tuncbilek lignite. ....	70
Figure 5.21. Inorganic structure of lignite residue after wet air oxidation for the longest and shortest duration. ....	73
Figure 5.22. Inorganic structure of lignite residue after wet air oxidation at 1 bar and 7 bar. ....	74
Figure 5.23. Inorganic structure of lignite residue after wet air oxidation at 150°C and 180°C. ....	76
Figure 6.1. Three technologies for CO <sub>2</sub> capture from fossil fuels (GCCSI, 2012). ....	79
Figure 6.2. Chemical looping combustion system. ....	80
Figure 6.3. Co-Pb metal oxide preparation steps. ....	83
Figure 6.4. Standard Gibbs free energy change during lead oxide reduction. ....	85
Figure 6.5. Standard Gibbs free energy change during Cobalt oxide reduction. ....	86
Figure 6.6. Comparison between the PbO and CoO reduction with Carbon, Hydrogen, and Carbon monoxide. ....	86
Figure 6.7. TGA pyrolysis thermograms of coal in the presence of different metal oxide contents. ....	87
Figure 6.8. XRD patterns of Co-Pb based metal oxides. ....	88
Figure 6.9. Raman spectra of Co-Pb metal oxide. ....	89
Figure 6.10. The <sup>207</sup> Pb MAS spectrum of reference compounds of PbO-Pb(NO <sub>3</sub> ) <sub>2</sub> . ....	90
Figure 6.11. The <sup>207</sup> Pb MAS spectrum of reference compounds of PbS-Pb(NO <sub>3</sub> ) <sub>2</sub> . ....	91
Figure 6.12. The <sup>207</sup> Pb MAS spectrum of reference compounds of PbSO <sub>4</sub> -Pb(NO <sub>3</sub> ) <sub>2</sub> . ....	91
Figure 6.13. The <sup>207</sup> Pb MAS spectrum of Co-Pb metal oxide- Pb(NO <sub>3</sub> ) <sub>2</sub> with spin-echo. ....	92
Figure 6.14. CH <sub>4</sub> formation rates under N <sub>2</sub> flow using the constant coal: metal oxide ratio of 10 (wt/wt). ....	93
Figure 6.15. H <sub>2</sub> formation rates under N <sub>2</sub> flow using the constant coal: metal oxide ratio of 10 (wt/wt). ....	93
Figure 6.16. CO <sub>2</sub> formation rates under N <sub>2</sub> flow in the presence and absence of metal oxide. ....	94
Figure 6.17. CO <sub>2</sub> formation rates of pure coal during air oxidation and coal/Co-Pb =1 during pyrolysis. ....	95
Figure 6.18. CH <sub>4</sub> formation rates under air flow using the constant coal: metal oxide ratio of 10 (wt:wt). ....	97
Figure 6.19. H <sub>2</sub> formation rates under air flow using the constant coal: metal oxide ratio of 10 (wt:wt). ....	97
Figure 6.20. CO <sub>2</sub> formation rate in the presence and absence of metal oxides using the fix coal: metal oxide ratio of 10. ....	98
Figure 6.21. CO <sub>2</sub> emission during air oxidation of the pyrolysis residues. ....	99
Figure 6.22. The visual and microscopic images of PbO reduction to metallic Pb during pyrolysis and oxidation reactions. ....	101
Figure 6.23. In-situ sulfur capture potential of PbO: (a) fresh Co-Pb metal oxide, (b) after pyrolysis, (c) after oxidation, and (d) after hydrogenation. ....	101
Figure 6.24. Oxidation thermodynamics of PbS. ....	102
Figure 6.25. Sulfur looping flow diagram. ....	103
Figure B.1. Pore diffusion effects on CH <sub>4</sub> (a) and H <sub>2</sub> (b) formation rates for different particle sizes. ....	121
Figure B.2. (a) CH <sub>4</sub> and (b) H <sub>2</sub> formation rates under non-isothermal condition and different flow rates. ....	122

Figure C.1. Curve fitting data for proton NMR data of unprocessed Tuncbilek lignites. ....	123
Figure D.1. Pulse length (a) and nutation time (b) experiments. ....	124

# CHAPTER 1

## INTRODUCTION

### 1.1 Background

Eighty percent of energy demand of the world is currently met by fossil fuels. Among the fossil fuels, oil constitutes 32%, coal constitutes 27%, and natural gas constitutes 21% as the primary energy carrier distribution of the world (IEA-InternationalEnergyAgency., 2012, Karakosta, 2013, Fan and Jadhav, 2002). Coal is still the cheapest fossil fuel and it is globally distributed, which makes coal utilization favorable. However, direct combustion of coal for energy generation is less desirable due to the environmental concerns and low thermodynamic efficiencies of the steam power generation cycles. Coal based power stations can cause the emission of the air pollutants like, CO<sub>2</sub>, SO<sub>x</sub>, NO<sub>x</sub> and also particulate matters. CO<sub>2</sub> is the main reason of global warming and CO<sub>2</sub> emission coal based constitutes the largest share. SO<sub>x</sub> and NO<sub>x</sub> compounds in the atmosphere cause the formation of acid rain. The particulate form of these oxides is very dangerous for human health, leading to serious illnesses such as asthma, heart attack, and stroke.

In coal-fired power plants, coal is burned to generate steam and then superheated steam in steam turbine drives a generator during the expansion of the high-pressure steam. The condensed steam is returned to the boiler to be used once again. Electricity generated by coal combustion as a result is only a third of the energy potential of coal. The remaining is discarded as heat (Fan et al., 2008). In order to increase the efficiency of the power generation advanced clean coal utilization technologies are developed. Clean coal technologies include conventional technologies with pollution prevention and new and emerging technologies. Coal washing, flue gas desulfurization, and low NO<sub>x</sub> burners are conventional technologies with pollution prevention. New and emerging clean coal technologies consist of Integrated Gasification Combined Cycles (IGCC), Pressurized Fluidized Bed Combustion (PFBC), and Integrated Gasification Fuel Cell (IGFC). Among the rivals, presently IGCC is the most popular one. This technology uses synthesis gas produced by coal gasification in gas turbines with higher thermal to electrical conversion efficiencies. The hot gases at the exit of the gas turbines are used to produce steam to be used in the Rankine cycles. As a result, the combined cycles have higher efficiencies.

A flow chart for the coal gasification process and the post processes utilizing syngas given by Fan et al. (2008) is shown schematically in Figure 1.1.

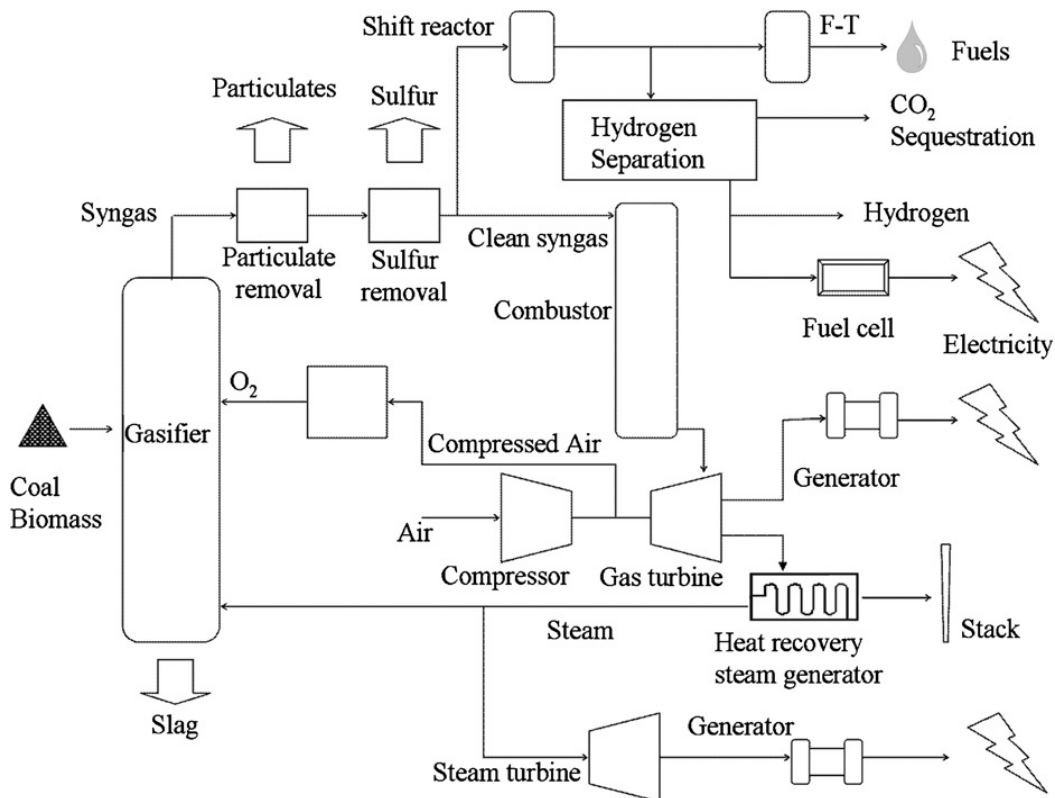


Figure 1.1. Schematic diagram of coal gasification processes for electricity, hydrogen, liquid fuel production (Fan et al., 2008).

Gasification is incomplete combustion of coal. In this process, coal reacts with sub-stoichiometric amount of oxygen, steam, and/or carbon dioxide in order to form syngas, a mixture of hydrogen and carbon monoxide. Gasification system, exhibited in Figure 1.1, serves to chemical manufacturing and electricity generation. Syngas can be used as an intermediate material to produce liquid fuels such as synthetic natural gas, methanol, and gasoline by Fisher-Tropsch synthesis. As seen in Figure 1.1, Water Gas Shift (WGS) reaction is an alternative way to produce fuels, more  $H_2$  and chemicals. Since this part leads to the more  $CO_2$  formation,  $CO_2$  sequestration is the important part of the IGCC plants (Fan et al., 2008). During gasification, sulfur in coal is converted to hydrogen sulfide ( $H_2S$ ) which is eventually extracted as elemental sulfur (S) and sulfuric acid ( $H_2SO_4$ ). These valuable byproducts are used in fertilizer industry. Non-gasified mineral compounds in coal leave the system as inert slag or solid products for cement and building materials (Gasifipedia, 2013).

IGCC is composed of two cycles, gas and steam. Coal is first gasified and cleaned from the compounds such as sulfur (S), nitrogen ( $N_2$ ) and mercury (Hg) in the first stage. The purified gasification product, syngas, is sent to the gas turbine integrated system to generate electricity. The hot effluent gas of the gas turbine is used to generate steam, which is used in a subsequent steam turbine to produce electricity as well. Thus, two combined turbines provide the higher efficiency than typical coal fired power plant (Descamps et al., 2008). The electricity efficiency of the IGCC with 250 and 335 MWe is between 38-45% (Damen et al., 2006).

The first utilization of coal was recorded by Marco Polo in the 13<sup>th</sup> century. According to his writings, coal was being used in China for heating and making iron tools and weapons. On the other hand, coal was just known as a black rock in Europe at that time. In the 18<sup>th</sup> century, Industrial Revolution took place in England due to the rich iron and coal reserves. Coal was used to boil water for steam engines in industrial and transportation applications. Thus, England obtained the economic leadership in the world. The discovery of coal in USA was in 1701, in Virginia. However, the combustible black rock was not used until Industrial Revolution reached to the USA. The common utilization of coal started in the 19<sup>th</sup> century (Hinckley, 2013). Coal became the main energy source in USA in the earlier 20<sup>th</sup> century. After the Second World War, coal lost its popularity due to the utilization of oil and natural gas in all energy platforms. Oil and natural gas have superiority compared to coal: transportation of them is easy, and their power generation efficiencies are higher. However, OPEC (Organization of the Petroleum Exporting Countries) oil embargo in 1973 increased the demand of coal especially in electricity generation. Furthermore, in 2005, oil and natural gas prices increased sharply due to another embargo, which is because of the concern about the limited oil and natural gas reserves. After the new crisis, coal based technologies are becoming popular once again.

Coal has the non-homogenous chemical structure consisted of carbon, hydrogen and oxygen elements. Sulfur and nitrogen are the other elements in the complex coal structure. Coke production is the other important application of coal.

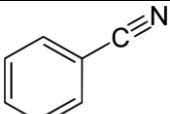
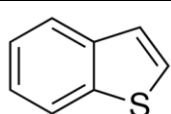
### **1.1.1 Coal petrography**

Coal petrography provides the information about origin, composition, and application of coal. Coal originates from the remains of plant matter on the ground. Biochemical and geochemical are two stages in the formation of coal. In the first stage, plants decay in the humid and warm climate because of the bacterial activities. Temperature and pressure lead to the organic decay in the geochemical stage. High pressure and temperature are required coalification conditions. Anthracite, bituminous coal, lignite, and peat are the four broad categories of coal. The types of coal or rank series are dependent upon carbon content and heating value of coal. The main properties of the coal type are summarized in Table 1.1. The organic constituents of coal derived from different parts of the plant are called as macerals. Coal types and macerals indicate the coal composition. For example, the existence of carbonyl, carboxyl, and methoxy groups gives an idea for the oxygen content of coal. Similarly, aromatic nitriles and pyridines are the identifier for nitrogen, while mercaptanes and thiols show the sulfur existence. Coal rank is also determining parameter for the utilization of coal. Since the structure of coal is more stable in the high rank coal, combustion and gasification reactivity of coal decrease with increasing rank (Kirk-Othmer, 2002a). Lastly, in Table 1.2, some of the nitrogen and sulfur compounds that can be found in coal structure are shown.

Table 1.1. Mineral matter free basis humid coal composition (Kirk-Othmer, 2002a).

Types of coal	Moisture (wt %)	Volatile Matter (wt %)	Heating value (kJ/g)	Elemental composition (wt %)			
				C	H	O	N
Peat	70-90	45-75	17-22	45-60	3.5-6.8	20-45	0.75-3.0
Lignite	30-50	45-60	28-30	60-75	4.5-5.5	17-35	0.75-2.1
Bituminous	1.0-20	11-50	29-37	75-92	4.0-5.6	3.0-20	0.75-2.0
Anthracite	1.5-3.5	3.5-10	36-37	92-95	2.9-4.0	2.0-3.0	0.5-2.0

Table 1.2. Nitrogen and sulfur compounds of coal (Spitz, 2004).

Nitrogen compounds	Structure	Sulfur compounds	Structure
Pyridine		Mercaptane	$R-SH$
Pyrrole		Thiophene	
Aromatic nitriles		Thiols	

### 1.1.2 Worldwide coal reserves

Coal is a globally distributed energy source. USA, Russia, and China have the largest coal reserves of the world. The distribution of the coal reserves by country is shown in Figure 1.2. Turkey is placed in 20% slice of other countries with a 1% coal.

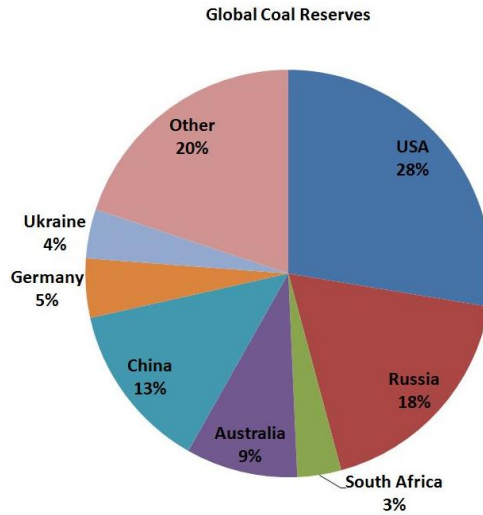


Figure 1.2. Global distribution of coal reserves (Gue, 2012).

### 1.1.3 About coal in Turkey

Coal and lignite meet the demands for nearly 25% of Turkey's electricity generation. According to Turkish Coal Enterprises (TKI), Turkey has approximately 13.9 billion tons lignite and 1.3 billion tons hard coal reserves. This corresponds to 1.8% of the world's useable coal and 7.1% of the world's global lignite reserves. With the new mining (drilling) studies, Turkey's coal reserve estimates have increased by 5.8 billion tons in past 5 years. The location of coal reservoirs are indicated in Figure 1.3. Zonguldak, in northwest of Turkey is the hard coal reservoir of Turkey. The calorific value of this hard coal is between 6200 and 7200 cal/g. On the other hand, lignite reserves are spread all around the county. The largest lignite reserves are Afsin-Elbistan lignite basin of southeastern Anatolia. Soma basin is the second largest area followed by Tunçbilek, Seyitömer, Bursa, Çan, Muğla, Beypazarı, Sivas and Konya Karapınar basins. Heating value of Turkish lignite is approximately 3000 cal/g. 6% of the reserves have calorific values more than 3000 cal/g (EURACOAL, 2013).



Figure 1.3. Coal resources locations in Turkey (EUROCOAL, European Association for Coal and Lignite).

## 1.2 Motivation

Lignite is one of the major domestic energy resources in Turkey. Lignite reserves have been widely spread across the country. Since it has very high amount of ash and low heating value, lignite is called a low quality coal. Additionally, high sulfur content in Turkish lignite is the other drawback of the utilization. As a result, coal gasification comes out as a promising and environmentally effective clean coal technology. Since the physical and chemical properties of coal determine its processing fate, a detailed characterization is very important prior to any coal carbonization, oxidation, and gasification and/or liquefaction. In addition, understanding desulfurization behavior of the lignites offers new insights when processes are evaluated for their feasibility.

## 1.3 Objectives

The aim of this Ph.D project was to develop a fundamental understanding of Tuncbilek lignite gasification and desulfurization processes. Pyrolysis, oxidation, and hydrogenation were studied as the main processes taking place during the gasification. Furthermore, hydrogenation and hydrothermal desulfurization processes were compared for their efficiencies. In order to achieve this aim, the following activities were conducted:

The pyrolysis, oxidation, and hydrogenation reactions taking place during gasification process were investigated, separately. The relationship between the structural changes of Tuncbilek lignite and its reactivity was determined. XRD, DRIFTS and solid state  $^1\text{H}$  and  $^{13}\text{C}$  NMR were used to monitor the structural changes after each process.

Three processes, pyrolysis, hydrogenation and hydrothermal treatment, were examined for the desulfurization of Tuncbilek lignite. Sulfur contents of the lignite residues were determined by elemental analysis and Eschka methods.

Co-Pb based metal oxides were employed as oxygen and sulfur chemical looping agents. The increase in CO<sub>2</sub> formation rates with increasing amount of Co-Pb metal oxides indicated the oxygen exchange potential of these metal oxides. In addition, XRD patterns of the lignite residues revealed that PbS formation is inevitable.

#### **1.4 Summary of the study**

Chapter 2 summarizes the previous studies about the coal gasification, coal characteristics, and the relationships between the coal structure and reactivity under different reaction environments such as, N<sub>2</sub>, air, CO<sub>2</sub>, hydrogen, and steam. Additionally, main processes during gasification, pyrolysis, oxidation, and hydrogenation and their applications and processes utilizing catalysts are discussed in this chapter.

Chapter 3 describes the materials and methods. Types of reactors, experimental conditions, and analytical and instrumental characterization methods are covered in this part. The details of coal gasification processes, i.e., pyrolysis, oxidation, hydrogenation, and wet air oxidation, are described, and the experimental set-ups used to monitor these processes are presented schematically. The methodologies are also given.

The chemical and structural characteristics of Tuncbilek lignite and the relationship between structure and reactivity is presented in Chapter 4. In this context, the results of classical and spectroscopic analyses are discussed.

The results of the gasification and desulfurization reactivity of Tuncbilek lignite are presented in Chapter 5. Pyrolysis, oxidation, hydrogenation, and wet air oxidation are studied separately and the results are compared in terms of the structural changes occurring during the processes. The gaseous products analyses during pyrolysis and air oxidation experiments mainly focused on methane (CH<sub>4</sub>) and hydrogen (H<sub>2</sub>). The XRD, DRIFTS, and solid-state proton and carbon NMR spectroscopy results of solid carbon residue are discussed for each process.

The chemical looping combustion concept based on the studies done during this thesis for high sulfur coal gasification is presented in Chapter 6. The proposal is based on the gasification and desulfurization reactivity of Tuncbilek lignite in the presence of Co-Pb based metal oxides and their oxidation and sulfur capturing ability are explained in Chapter 6.

The discussion, conclusions, and recommendations are presented in Chapter 7.



## CHAPTER 2

### LITERATURE SURVEY

#### 2.1 Gasification

Gasification is a multi-purpose coal conversion process which has been used for over a century. This old technology was applied to produce coal gas in 1850s for lightening and heating. The major aim of the gasification process is energy generation, while H<sub>2</sub> production as a type of transportation fuel and synthesis gas production as raw materials for chemicals like ammonia, methanol and oxychemicals, are other utilization purposes of gasification process. In coal gasification process, coal reacts with sub-stoichiometric amount of oxygen, steam and/or carbon dioxide to produce synthesis gas, which is the mixture of carbon monoxide and hydrogen. The main reactions taking place during gasification are listed in Table 2.1 (Kabe et al., 2004b). Thermal decomposition, oxidation, methanation, and water gas shift reactions are the important reactions during the gasification process. The greatest benefit of the gasification process is to prevent all environmental challenges caused by the common coal utilization processes (Minchener, 2005, Kirk-Othmer, 2002b, Kabe et al., 2004b). For example, gasification product of sulfur is hydrogen sulfur instead of combustion product of sulfur oxide. Similarly, nitrogen in coal converts to ammonia during the gasification process instead of nitrogen oxide, which is the combustion product (Kabe et al., 2004a, Kirk-Othmer, 2002b, Kabe et al., 2004b).

According to the World Gasification Database, the coal based gasification capacity of the world is 36,315 megawatts thermal (MW<sub>th</sub>) of syngas output. There are 53 plants operating with 201 gasifiers. Coal is the primary feedstock of the gasification plants with a 51% capacity. Petroleum, gas, petcoke and biomass wastes are also used as feedstock in the gasification plants (NETL, 2010).

When we look at the gasification plant capacity of the world in Figure 2.1, the Asia/Australia region with 11 countries is in the first position among the 29 countries. On the other hand, North America expects 63% capacity growth until 2016. The product distribution of syngas output gasification plants is also listed in the World Gasification Database as chemicals (45%), liquid transportation fuels (38%), and gaseous fuels (6%) (NETL, 2010).

Coal types and properties are the determining parameters of the technologies used. For example, high ash content is the undesired property increasing the technology cost (Minchener, 2005, Kabe et al., 2004a). Coal gasification technologies can be classified with respect to solid and gaseous reactant flow geometry mainly as fixed-bed, fluidized-bed, and

entrained-bed gasification (Kabe et al., 2004a, Minchener, 2005). In addition, Kabe, et al. (2004) includes the molten-bath gasification to this classification.

Shell entrained-bed gasification is the most common technology (~75%) worldwide. Texaco (GE, E-Gas) also use the entrained-bed technology. The Sasol Lurgi is the main user of the fixed-bed gasification technology. As seen in Figure 2.2, this design ranked second in the world (Minchener, 2005, NETL, 2010). The details of the technologies are described in the following part.

Table 2.1. Exothermic and endothermic reactions during gasification (Kabe et al., 2004b).

$C_{(s)} + O_{2(g)} \leftrightarrow CO_{2(g)}$	<i>exothermic reaction</i>	(2.1)
$C_{(s)} + 1/2O_{2(g)} \leftrightarrow CO_{(g)}$	<i>exothermic reaction</i>	(2.2)
$C_{(s)} + H_2O_{(g)} \leftrightarrow CO_{(g)} + H_2(g)$	<i>endothermic reaction</i>	(2.3)
$C_{(s)} + CO_{2(g)} \leftrightarrow 2CO_{(g)}$	<i>endothermic reaction</i>	(2.4)
$CO_{(g)} + 1/2O_{2(g)} \leftrightarrow CO_{2(g)}$	<i>exothermic reaction</i>	(2.5)
$CO_{(g)} + H_2O_{(g)} \leftrightarrow CO_{2(g)} + H_2(g)$	<i>exothermic reaction</i>	(2.6)
$CO_{(g)} + 3H_2(g) \leftrightarrow CH_4(g) + H_2O_{(g)}$	<i>exothermic reaction</i>	(2.7)
$C_{(s)} + 2H_2(g) \leftrightarrow CH_4(g)$	<i>exothermic reaction</i>	(2.8)

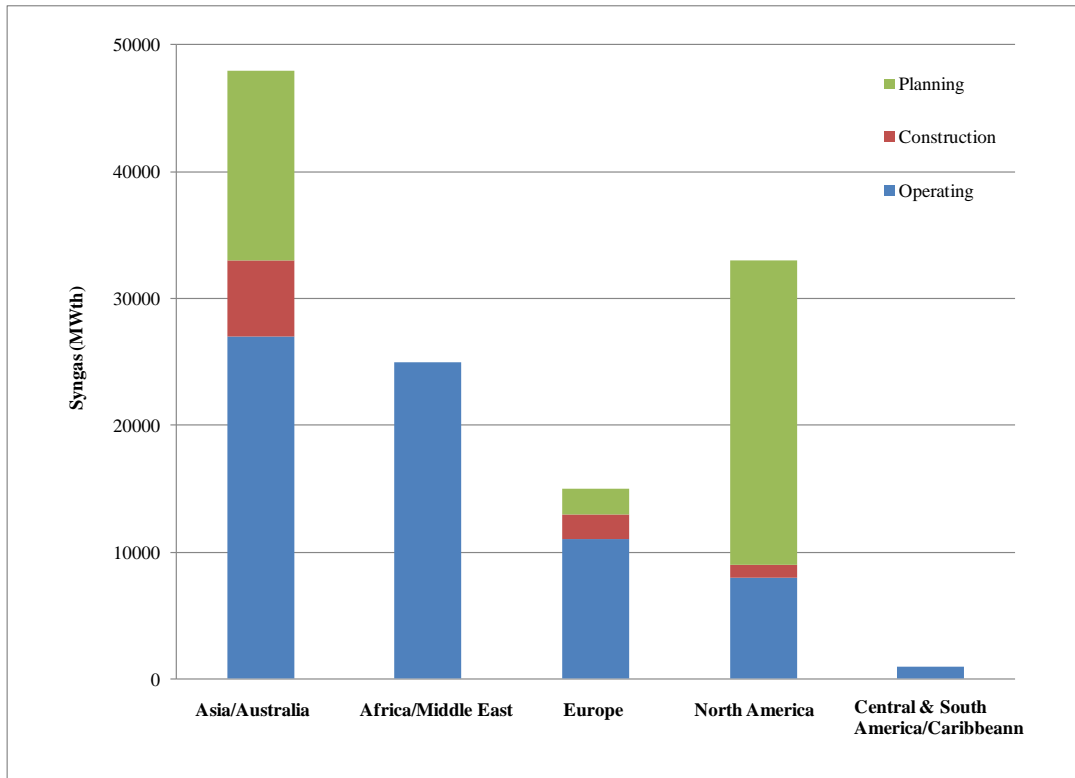


Figure 2.1. Regional distribution of operating, constructing and planning gasification plant capacity of the world (NETL, 2010).

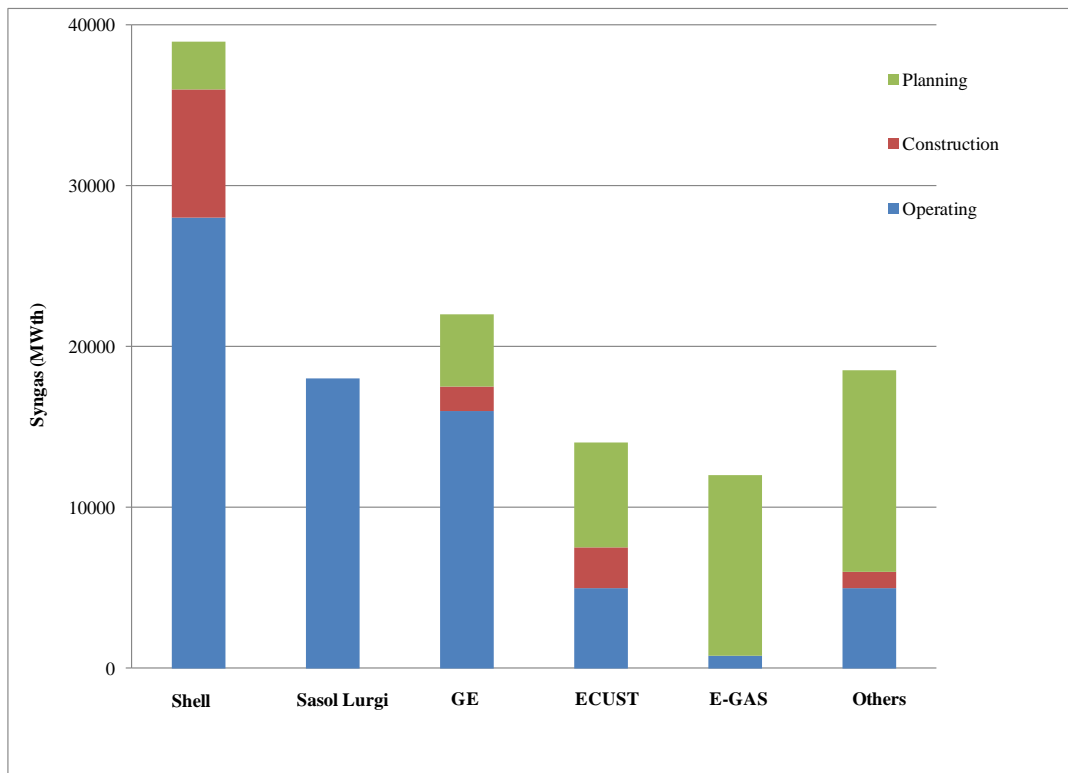


Figure 2.2. Technology distribution of gasification (NETL, 2010).

## 2.2 Types of gasifiers

### 2.2.1 Fixed-bed (or Moving-bed) gasifier

The reactant gases are fed from the bottom while coal is fed from top of the gasifier. This counter current flow provides the heat exchange between the fresh cold raw materials and hot products. Thus, the exit streams of the gasifier remains moderately cold (van Dyk et al., 2006). As seen on the right hand side of the Figure 2.3, when coal is moving downward, it starts to be heated by hot gas stream. Moisture is removed by the temperature difference, first. Devolatilization also takes place due to thermal decomposition reactions. After the exothermic and endothermic reactions occurred during gasification, ash temperature is around 400°C, while gas temperature is around 700°C (van Dyk et al., 2006, Kabe et al., 2004a).

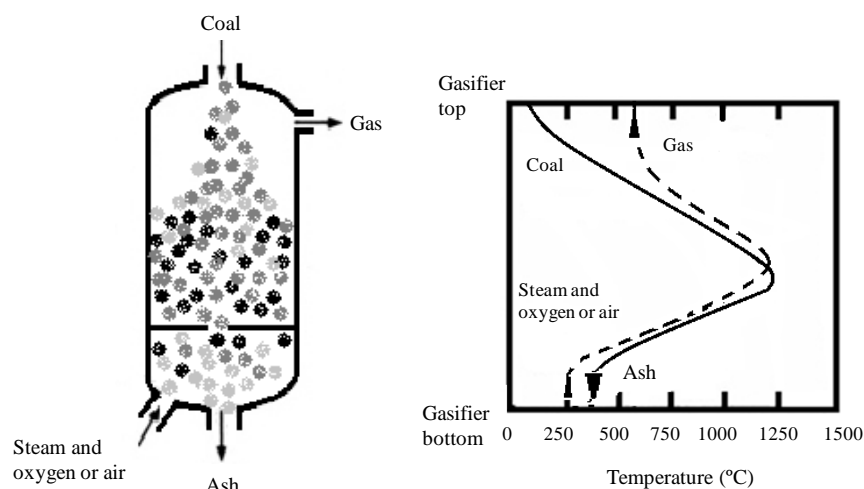


Figure 2.3. Fixed-bed gasifier (van Dyk et al., 2006).

### 2.2.2 Fluidized-bed gasifier

The fluidized-bed gasifier is shown in Figure 2.4. Pulverized coal particles are fed from the top of the reactor while the direction of the gas reactant (air, oxygen, and/or steam) is upward. Sand, coke, char, and ash can be used as bed material. Fluidization provides the longer residence time than entrained bed gasifier due to the perfect interaction of the gas-solid reactants. Similarly, mixing makes uniform temperature distribution possible along the gasifier. Operation temperature must be lower than the ash melting temperature (900°C - 1050°C) (Minchener, 2005, Lee, 2007). The continuous ash removal pattern allows the higher carbon conversion. Another advantage of this type of gasifier is that product gases including sulfur such as H<sub>2</sub>S and carbonyl sulfates (COS), can be held up by the sorbent bed material (Minchener, 2005). Fluidization, gasification and sulfur removal by limestone addition are three processes operating at the same time in the fluidized-bed gasifier. These make the fluidized-bed application more difficult than others (Maurstad, 2005).

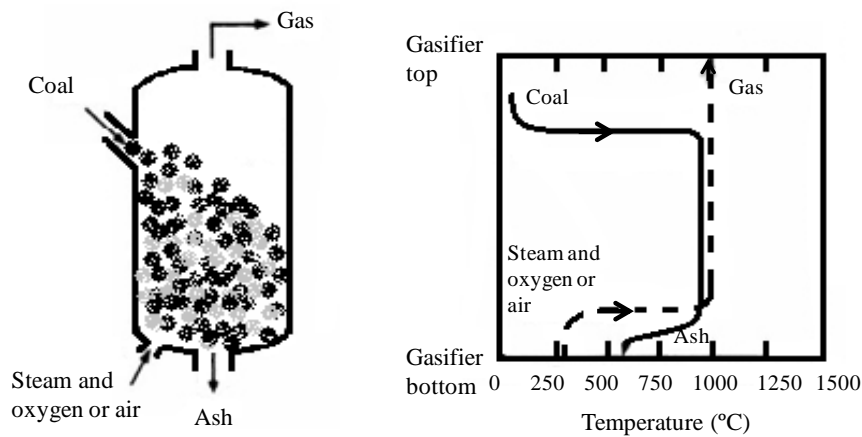


Figure 2.4. Fluidized-bed gasifier (Maurstad, 2005).

### 2.2.3 Entrained-bed gasifier

In the Entrained-bed gasifier in Figure 2.5, solid particles and gas reactant (steam, oxygen, or steam) are fed concurrently from top of the reactor. Coal can be dry or wet when it is fed into the reactor. High temperature (1200°C-1600°C) and pressure (2-8 MPa) are the operating conditions of this type gasifier. The higher temperature operation requires the higher oxygen consumption and it allows the higher carbon conversion and tar free syngas formation. However, since molten slag formation due to high temperature can be optimized to a certain degree, coal with low ash content is preferred in this technology (Minchener, 2005, Maurstad, 2005). Another challenge of the process is the hot syngas (~ 1500°C) at the end of the gasifier. The energy potential of the syngas can be used to generate steam and electricity by adding a heat recovery unit to the system (Maurstad, 2005).

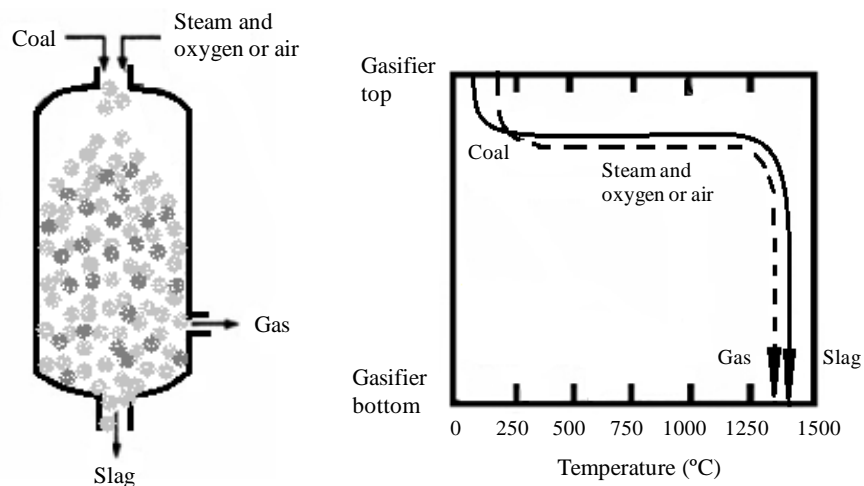


Figure 2.5. Entrained-bed gasifier (Kabe et al., 2004a).

### 2.2.4 Molten-bed gasifier

In this type of the gasifier, molten bath of salt or metal are used. The gasifier with molten iron bath (Figure 2.6) represents the molten-bed gasifier. Pulverized coal and steam and/or oxygen are fed into the gasifier concurrently. However, their contact is in the molten-bed. Operating temperature is in the range of 1000°C -1400°C, while pressure is about 3 bar. Slag including ash and sulfur is removed on the bed. Molten iron functions in this process as an oxygen carrier between the coal and steam and/or O<sub>2</sub>. Furthermore, it adsorbs sulfur compound in coal (Kabe et al., 2004a).

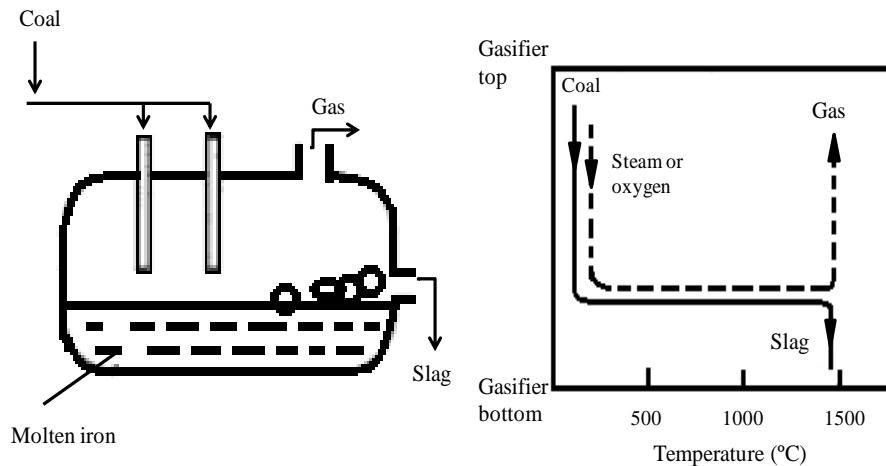


Figure 2.6. Molten-bed gasifier (Kabe et al., 2004a).

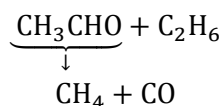
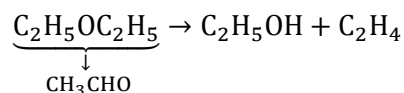
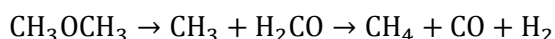
## 2.3 Main processes taking place during gasification

Drying, pyrolysis, oxidation, and gasification are the main gasification steps. The moisture content of the coal is removed during the drying process. The removal of the some organic liquids and volatiles are the pyrolysis products. During the oxidation, carbon and hydrogen based substances or char formed from pyrolysis are converted into CO<sub>2</sub> and H<sub>2</sub>O. The exothermic combustion reactions meet the heat requirement of endothermic gasification reactions. Thermal equilibrium between the exothermic and endothermic reaction leads to the high carbon conversion.

### 2.3.1 Coal drying and pyrolysis

Pyrolysis is a thermal decomposition process of the organic compounds in the oxygen free atmosphere. It can be considered as the initial stage of the coal technologies like combustion, gasification and hydrogenation. This process is a fundamental and efficient coal conversion process, which provides the coke, tar and synthesis gas production (van Heek, 2000, Arenillas et al., 2003). Figure 2.7 summarizes the structural changes of coal together with pyrolysis products (Veras, 2002 ). In this process, volatile contents of the feedstock are lost because of the rising temperature, and thus, relative amount of carbon content in the remaining part increases. Volatiles and solid residue are the main products of

pyrolysis. During the pyrolysis, the first step is desorption of water and light hydrocarbons at temperatures less than 150°C. Cracking of complex coal structure into light hydrocarbon fragments, CO<sub>2</sub> and water are the second step of pyrolysis products occurring up to 500°C. Solid coal char and CO, CH<sub>4</sub> and H<sub>2</sub>, which are the most valuable gaseous products, are formed during the third stage of the pyrolysis between 500°C and 800°C (Arenillas et al., 2003). CO<sub>2</sub> evolution at lower temperature is due to aliphatic carboxylic acids, whereas phenolic groups are converted to CO at high temperature. H<sub>2</sub> evolution begins approximately at 300°C with the destruction of the H<sub>2</sub> rich part of the coal, and it reaches a higher amounts due to the condensation of aromatic rings at 450°C. The other important gaseous product, CH<sub>4</sub>, may form in three steps. First, destruction of aliphatic and aromatic ether bonds leads to CH<sub>4</sub> formation at the temperatures in between 400°C-450°C. Then, decomposition of the strong bonds is responsible for CH<sub>4</sub> production at 500°C-550°C. Finally, at 700°C, CH<sub>4</sub> is formed due to the second stage devolatilization (Arenillas et al., 2003). The parameters affecting pyrolysis product yields are experimental conditions (pressure and temperature) and coal properties (particle size and coal types). In addition, final temperature and pyrolysis environment affect the volatiles forming during pyrolysis (Gupta, 2007). The representative thermal decomposition reaction of ether bonds are indicated by Meyers (1982) (Meyers, 1982).



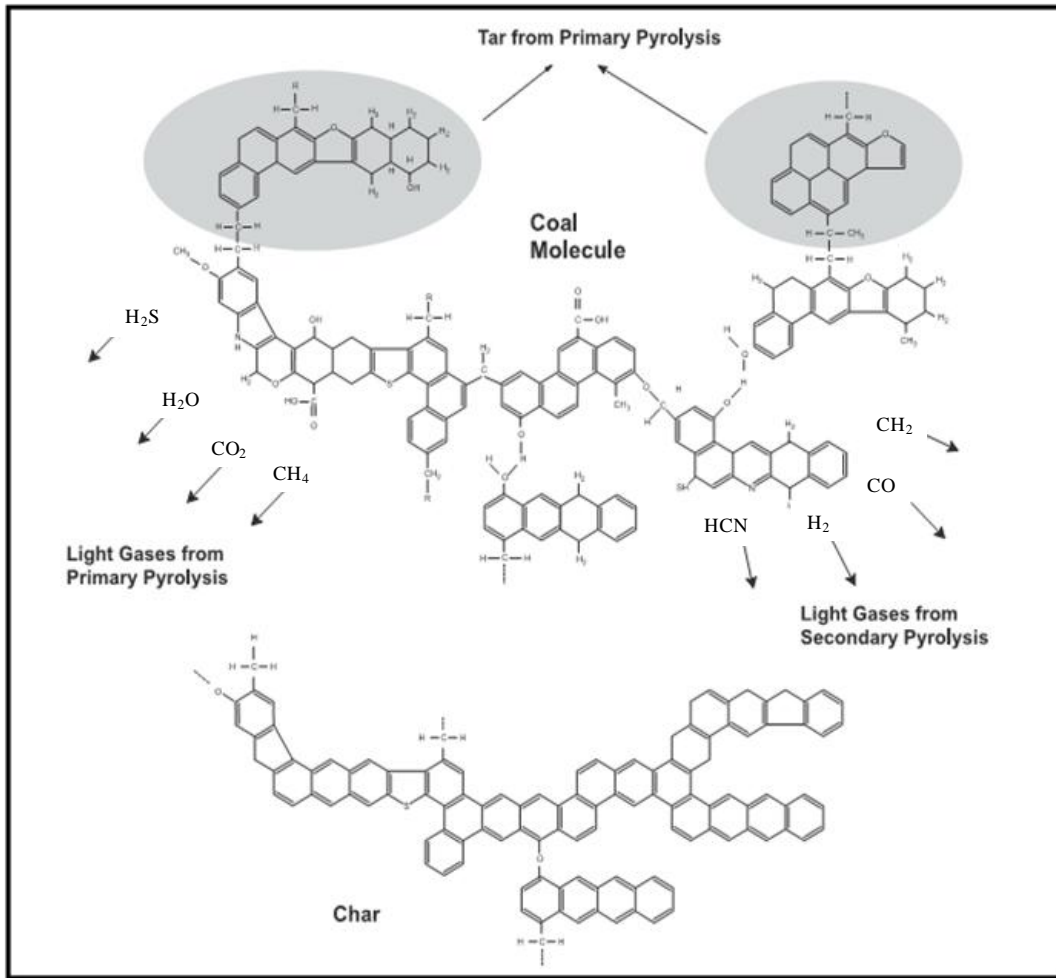


Figure 2.7. Coal molecular structure simulation (Veras, 2002 ).

### 2.3.2 Coal oxidation

Combustion or coal oxidation is the best known coal utilization technology. Chemical composition and physical structures are very complicated variables to affect the coal combustion. Wang et al. (2003) reviewed the coal oxidation literature in detail. As reported in this review, when coal is contacted with oxygen, oxidation reaction is inevitable. The occurrence of the oxidation can be followed by O<sub>2</sub> consumption initially and then oxidation products make the investigation of the process progress possible.

Coal and oxygen interaction begins with physical adsorption. Oxygen molecule is adsorbed on the coal surface by relatively weak bonds. Chemisorption, distinct from the adsorption, occurs with strong bonds at the pore surfaces. Physical adsorption is important at temperature lower than 273 K. However, chemisorption manages the oxidation process at higher temperature. Oxygen consumption can be explained by three reaction regimes including, external mass transfer, internal diffusion, and chemical reaction. External mass transfer is generally faster than other two regimes. If there is no film on the char particle surface, oxygen can move easily on to external surface. The formation of gaseous film

around the particles causes the external mass transfer resistance. In this case, reaction rate is dependent on the mass transfer coefficient and particle surface. The other two regimes depend on the Thiele Modulus, which is the ratio of reaction rate to diffusion rate. The reaction rate control regime is generally defined at low temperature and very small particle size. Since oxygen can diffuse very fast into the pores, oxygen concentration in pore is equal to gas phase bulk concentration. Therefore, diffusion rate is higher than reaction rate and Thiele modulus is lower than unity. As a result, chemical reaction controls the oxygen consumption rate. When particle size of char increases, intra molecular flow rate of oxygen decreases. Since diffusion dominates the oxygen consumption rate, Thiele modulus is higher than unity. In Figure 2.8, the effect of particles size on oxygen consumption rate is demonstrated. As seen in Figure 2.8, chemical reaction control regime is not dependent on the particle size (Wang, 2003, Di Blasi, 2009).

In order to eliminate diffusion effect, several particle sizes were examined in literature. Kovacik, et al. (1991) were determined the optimum particle size as 74-105 micrometer at 900°C (Kovacik et al., 1991). In another study conducted by Chin et al. (1983), diffusion resistance was not observed when particle size increased up to 1 mm (Chin et al., 1983).

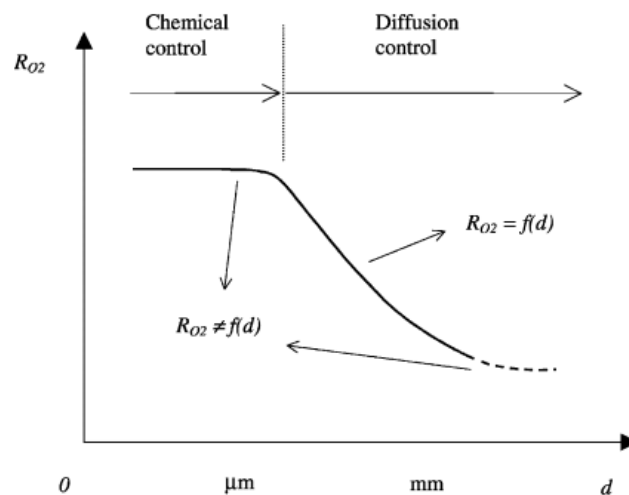


Figure 2.8. Particle size effect on the reaction regime (Wang, 2003).

Batchelder et al. (1953) studied on the heterogeneous carbon oxidation reactions. In order to determine whether the rate-controlling step is diffusion control or chemical reaction control, they changed the gas velocity at constant temperature. Mass transfer (external diffusion) effects are important when the rate of reaction increases with increasing gas velocity or vice versa. Low pressure, low temperature, and sufficiently high flow rate are needed to prevent the diffusion effects. Since carbon-oxygen reaction is very fast, they determined that diffusion controls the rate of the carbon-oxygen reaction at combustion and gasification temperatures. Because of the lower activation energy for diffusion step, as the temperature increases, the rate of the chemical reaction steps increases even more. Thus, the mechanism shifts toward diffusion control. As a result, since high temperature and relatively big

particles favor diffusion control, a lower temperature and smaller particle size are necessary in order to overcome the diffusion limitation (Batchelder, 1953).

Low temperature oxidation reactions allow the formation of both gaseous and solid products. The major gaseous products of coal combustion are  $\text{CO}_2$ ,  $\text{CO}$ , and  $\text{H}_2\text{O}$ . In addition, operating temperature determines the products fate. For example,  $\text{CO}$  concentration increases dramatically with a small amount of temperature increase. Phenolic hydroxyls ( $-\text{OH}$ ), carbonyl groups ( $\text{COO}-$ ), and carboxyl groups ( $-\text{COOH}$ ) are solid products of oxidation reactions (Wang, 2003). As mentioned in Wang et al., the formation of aliphatic and aromatic hydroxyl groups is possible coal and air interaction at ambient condition. Carbonyl and carboxyl group containing species can be generated by oxidation in the temperature range between  $40^\circ\text{C}$ - $160^\circ\text{C}$  (Wang, 2003).

### **2.3.3 Catalyst utilization for coal gasification**

In literature, catalyst utilization is found as necessary due to some important reasons. It enhances the synthetic fuel production by decreasing the high temperature and pressure gasification conditions. Additionally, it provides the high reaction rate and desired product selectivity. There is no need the high amount of oxygen in the presence of catalyst for the coal conversion and gasification processes (Kuznetsov, 2009).

Zhang et al. (2010) reported the catalytic activity of inorganic coal structure as a function of the dispersion and their chemical formulations (Zhang et al., 2010). Since brown coals or lignites have the high amount of the mineral composition with oxide form, the catalytic activity is observed during the gasification reactions. The catalytic activity of the metal oxide is based on the formation of oxidizing reagent. Fe is one of the most important metal species having the catalytic activity in coal structure. In order to keep Fe in active form, reducing conditions are necessary. The sintering effect or catalyst deactivation is a possible problem for steam gasification process in the presence of Fe (Skodras and Sakellariopoulos, 2002).

Alkali and alkaline earth metal species, especially potassium and calcium salts are preferred as catalysts for steam and  $\text{CO}_2$  gasification of coal and carbonaceous materials. Especially  $\text{CO}_2$  gasification rate increases in the presence of  $\text{CaO}$ . The catalytic activity of K and Na oxide is less than  $\text{CaO}$  due to the less amount of K and Na oxide in lignite structure (Skodras and Sakellariopoulos, 2002). In the presence of  $\text{K}_2\text{CO}_3$  catalyst, the amount of gaseous products and  $\text{H}_2$  evolution rate increase substantially by comparison without catalyst. Since the interaction between the catalyst and mineral composition in coal structure leads to catalyst deactivation, solvent extraction method can be used in order to prevent the catalyst recovery (Sharma et al., 2009). Alkali metals provide the mobility for  $\text{CO}_2$  and steam gasification processes. The eutectic mixture of alkalis ( $\text{LiCO}_3$ ,  $\text{NaCO}_3$  and  $\text{KCO}_3$ ) was found as more active catalyst than individual ones because of lower melting point of the mixture and lower activation energy. The main reason for the increase of the gasification rate was interpreted that molten phase provides the well dispersion and penetration of the catalyst on the coal structure. The formation of the intermediates with catalytic activity may be another reason of high gasification performance (Yeboah et al., 2003, Sheth et al., 2003).

Cakal et al. (2007) investigated simultaneous pyrolysis and CO<sub>2</sub> gasification behaviors of Turkish lignites by using Thermogravimetric Analysis (TGA) in the temperature range from 750°C to 1000°C. In their study, CO<sub>2</sub> gasification measurements were carried out at the final pyrolysis temperatures. Three topics were investigated: (i) the correlations between amounts of mineral constituents of coals, -especially alkali and alkaline earth metal (AAEM) elements, and some transition metals (iron, nickel, etc.),- and their reactivity; (ii) the effect of demineralization of coals on their reactivity; (iii) catalytic activity of AAEM salts on reactivity. They observed that the presence of AAEM and transition metal oxides increase the gasification reactivity of the low rank coals. However, regular behavior between gasification reactivity and calcium, potassium and sodium contents of lignites was not found, while gasification reactivity increased in the presence of iron at 1000°C. The researchers also identified the coal reactivity with the internal pore structure of coal. They concluded that reactivity is temperature dependent. Temperature increases both the catalytic activity of iron and leads to new pore formation, to open the closed pores, and to widen the present pores. (Cakal et al., 2007).

Sharma et al. (2008) performed the catalytic steam gasification of ultra clean coal by using K<sub>2</sub>CO<sub>3</sub> as a catalyst at 650°C-770°C. They observed the higher gasification rate for hyper coal (ultra clean coal) than raw coal. The important result of the study is that catalyst recycle is possible in the presence of hyper coal due to the less mineral matter content of hyper coal. In this study, it is indicated that H<sub>2</sub> rich syngas can be synthesized by using the hyper coal for both fuel cell application and for gas to liquid process (Sharma et al., 2008).

In another study, the catalytic performance of K<sub>2</sub>CO<sub>3</sub> was tested by Wang et al. (2010) in the presence of Ca(OH)<sub>2</sub> which is added to coal initially. They showed that Ca(OH)<sub>2</sub> behaves as promoter in the catalytic steam gasification of coal char and it improves the catalytic performance of K<sub>2</sub>CO<sub>3</sub> by preventing the catalyst deactivation. The addition of Ca(OH)<sub>2</sub> in the char preparation part is a novel approach and it provides the higher gasification rate (Wang et al., 2010b).

Yeboah et al. (1998) reported the catalytic effect of low melting point eutectic salt mixtures on coal gasification process. They summarized the literature results of the comparison between K<sub>2</sub>CO<sub>3</sub> and the eutectic mixtures of Li- Na- and K-carbonates in the activation energy. It was reported in the literature that eutectics have the lower activation energy and melting temperature than individual K<sub>2</sub>CO<sub>3</sub>. Yeboah et al. explained that the main reason of the increase of the gasification rate is the penetrations of the coal particles by the molten phase (Yeboah et al., 1998).

### **2.3.5 Catalyst utilization during the substituted natural gas production**

In the late 1970's coal was considered as raw material for producing methane. In thermal gasification process, endothermic gasification takes place at 900°-1600°C. In order to convert gasification products of CO and H<sub>2</sub> to methane, it is necessary to use shift reactor and methanation reactor operating at 400°-500°C. Methanation reaction is exothermic and low temperature condition favors this reaction (Hirsch et al., 1982). On the other hand, in Exxon's catalytic coal gasification technology, gasification and methanation reactions occur

in the gasifier at the same operating temperature  $\sim 700^\circ\text{C}$  in the presence of catalyst. Steam gasification reactions in Exxon's catalytic coal gasification technology are indicated in Table 2.2. According to the table, total reaction is almost thermally neutral. However, only a small amount of heat is required in the gasifier to preheat the raw coal and recycled stream of steam, CO, and H<sub>2</sub>. Since thermodynamic limitations lead to the incomplete methane production, CO and H<sub>2</sub> are recycled to the reactor. In Figure 2.9, the process details are demonstrated (Nahas, 1983). The catalyzed coal was mixed with a mixture of steam and recycled stream in the fluidized bed gasifier. The existence of gasifier consists of solid waste and gases. The solid part was separated in a cyclone and sent to the catalyst recovery unit or returned to the gasifier to further gasification operations. The gaseous products were passed through the separators to remove H<sub>2</sub>O, NH<sub>3</sub>, H<sub>2</sub>S and CO<sub>2</sub>. Cryogenic distillation column was used to separate the remaining CO, H<sub>2</sub> and CH<sub>4</sub> mixture (Hirsch et al., 1982, Nahas, 1983).

Table 2.2. Steam gasification reactions (Nahas, 1983).

$C + H_2O \leftrightarrow H_2 + CO$	<i>Gasification</i>	$\Delta H_f = 267.6 \text{ kJ/moles } C$
$CO + H_2O \leftrightarrow H_2 + CO_2$	<i>Water – gas shift</i>	$\Delta H_f = -33.5 \text{ kJ/mole } CO$
$CO + 3H_2 \leftrightarrow CH_4 + H_2O$	<i>Methanation</i>	$\Delta H_f = -225.7 \text{ kJ/mole } CH_4$
$2C + 2H_2O \leftrightarrow CH_4 + CO_2$	<i>Overall</i>	$\Delta H_f = 8.4 \text{ kJ/mole } CH_4$

One of the first catalytic substituted natural gas synthesis studies was carried out by Nahas et al. (1983) who reported that all alkali metals are active catalysts for steam gasification processes and catalytic activity increases with increasing alkalinity. Due to the enough activity and low cost, potassium was preferred as catalyst (Nahas, 1983). The principal benefits from using an alkali metal gasification catalyst are increasing the rate of steam gasification, reducing agglomeration of caking coals, and approaching gas phase methanation reaction equilibrium. Catalyst utilization provides that endothermic and exothermic reactions are conducted in the same reactor at  $700^\circ\text{C}$  and 3.5 MPa. In Exxon catalytic gasification process, carbon monoxide and hydrogen products were recycled to the gasification reactor in order to increase the methane formation (Hirsch et al., 1982, Nahas, 1978, Furlong, 1978, Nahas, 1983). Before the recycle of the CO and H<sub>2</sub> gaseous products, they were mixed with steam and thermally preheated to  $800^\circ\text{C}$  to prevent the heat loss. Since the catalyst leaving the gasifier with the ash/char residue was too costly to discard, catalyst recovery unit was required step shown on the flow diagram. (Hirsch et al., 1982, Nahas, 1978, Kalina, 1978, Furlong, 1978). Exxon proposed that the catalyst cost can be reduced by potassium recovery. In this step, slag was taken from the bottom of the gasifier and mixed with Ca(OH)<sub>2</sub>. After the mixture was washed, solid part was separated from the liquid part by using the hydro cyclones (Gallagher, 1978, Nahas, 1983).

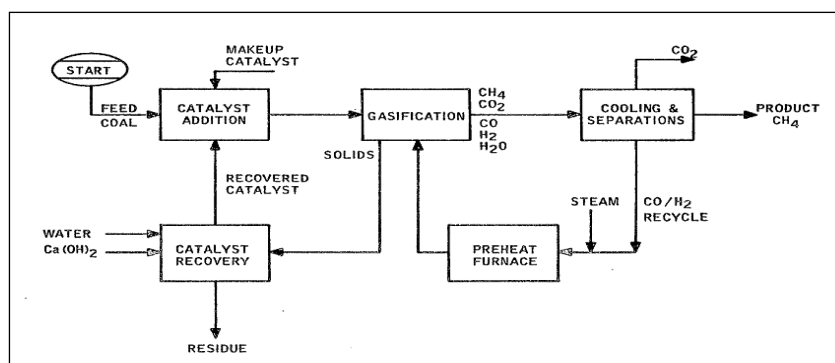


Figure 2.9. Exxon Catalytic Coal Gasification Process flowchart (Nahas, 1983).

Low temperature and high pressure make the methanation reaction favorable thermodynamically. Since catalyst utilization causes the low temperature condition, the single step methanation reaction takes place in the presence of catalyst during the gasification process. Catalytic activities of alkali and alkaline earth metal oxides and carbonates with transition metals (Fe and Ni) in the steam gasification experiments were investigated at 500 and 700°C and at 500 and 1000 psig by Hippo and Tandon (1996). They concluded that catalyst must be used in order to produce methane economically; catalyst preparation method, catalyst amount, and reaction conditions are the determining parameters for the effective methane production. The combination of alkali and transition metals provides significant synergistic effects. In addition to methane production, significant amounts of hydrogen can be produced at moderate gasification conditions (Hippo and Tandon, 1996).

### 2.3.4 Coal liquefaction and/or hydrogenation

Coal liquefaction is the conversion of coal to liquid synthetic fuels like diesel, naphtha and oil. Direct liquefaction of coal was firstly applied by German chemist Friedrich Bergius in 1913. After the direct coal liquefaction process, indirect coal to liquid technology was developed by Fischer-Tropsch in 1920s. Germany used this technology during the First and Second World Wars in order to supply their fuel demands. With a similar approach, coal liquefaction technology has been employed in South Africa due to the oil embargo, since 1950s and it meets nearly 30% of their petroleum needs (Hook and Aleklett, 2010).

A review about the conversion of coal into liquid process was published in International Journal of Energy Research. Hook and Aleklett (2010) investigated the coal liquefaction process in three ways: pyrolysis, direct coal liquefaction (DCL) and indirect coal liquefaction (ICL). Pyrolysis, the oldest one, is the heating process up to high temperatures (in this case 950°C). During this process, volatile matters of coal are removed while the carbon content of coal upgrades. Liquid products, which are generally called tar, are the side product of pyrolysis. However, there is no direct utilization of coal tar in the transportation sector. Industrial applications of tar can be listed as follows: manufacturing of roofing, waterproofing, and insulation products. It can also be used as a raw material for various

dyes, drugs, and paints. The main disadvantage of pyrolysis is the low yield of liquid product. In the DCL process, liquid yields and quality and overall thermal efficiencies are higher than in pyrolysis. Hydrogen is needed to crack the coal into synthetic fuels. Steam and methane can be used as the hydrogen source in this process. Additionally, H<sub>2</sub> can be supplied from coal by water gas shift reaction. Heat is also necessary to synthesize the liquid fuel and it can also be obtained from coal. The third technology, ICL meets the water requirement by converting coal into the synthesis gas. In order to convert coal into syngas, high amounts of steam and energy are needed for ICL process. ICL allows the production of many more than DCL systems. However, their costs are similar (Hook and Aleklett, 2010).

Coal liquefaction can be classified as direct and indirect coal hydrogenation processes. In direct coal hydrogenation process, direct interaction between the coal and hydrogen occurs in solvent slurry. It is necessary to add an extra amount of hydrogen in this process. Coal has the lower H/C ratio than petroleum-like products. Therefore, hydrogen is the main reactant used to increase H/C ratio. During this process, H<sub>2</sub> is also used to convert oxygen, sulfur, and nitrogen to hydrogen sulfide, and ammonia, respectively. In addition, the solvent serves as the transportation medium and it improves the mass and heat transfer effects. If the solvent dissolves H<sub>2</sub> from the gas phase and then carries it to the solid coal, this solvent is called a donor solvent. Coal molecules are cracked at elevated temperature thermally. High H<sub>2</sub> pressure is necessary to increase the reaction yield. Furthermore, high H<sub>2</sub> pressure stabilizes the liquid phase and prevents coke formation. The main disadvantage of the direct coal hydrogenation is its requirement for additional hydrogen. In comparison, during the indirect coal hydrogenation process, there are two steps; the synthesis gas formation by coal gasification and liquid products formation by Fischer-Tropsch synthesis. The capital cost and energy efficiency of indirect coal utilization technology are much higher than those of direct liquefaction technology (Robinson, 2009, Weller and Pelipetz, 1951).

Cracking and hydrogenating of coal and removing of O<sub>2</sub>, S and N<sub>2</sub> are the desired reactions in coal to liquids process (Robinson, 2009). However, asphalt is an undesired side product during the coal hydrogenation process (Weller et al., 1950). Weller et al. (1950) studied the optimum reaction conditions to prevent asphalt formation. Determination of the kinetics of asphalt formation is necessary to evaluate the coal hydrogenation process quantitatively. This research group used a batch-autoclave type of reactor in all their experiments. Their variables were temperature, pressure, and time. They used mass spectrometer to analyze the gaseous products. They plotted residual asphalt conversion vs. residence time in a semi-logarithmic scale at different temperatures. The linear relation indicated the first order relation between the asphalt conversion and reaction rate. High temperature dependencies were determined by controlling the specific rate constants. This implied that there is a chemical reaction in the rate-determining step. When the effect of hydrogen pressure was investigated, one temperature value was used and the reaction rate constant was observed to change almost linearly with H<sub>2</sub> pressure (Weller and Pelipetz, 1951, Weller et al., 1950).

Coal hydrogenation can be defined as a subversive process, which takes place under high H<sub>2</sub> pressure and by heating the system by Weller et al. (1951). In this process, the complex coal structure was cracked into smaller molecules. H<sub>2</sub> at high pressure reacts with unsaturated molecules, and polymerization and coke formation can be prevented. Thus, light oil

production yield can be increased. In order to increase reaction rates and selectivity, catalyst utilization is the most common way. The types of catalysts and their effects in the hydrogenation of coal were summarized as follows: (i) ammonium chloride alone had no positive effects while tin addition led to improved catalytic activity, (ii) synergy between halogen acids and tin generally caused the best catalytic activity with some exceptional halogen acids like germanium halogen acid, (iii) ammonium chloride, hydrochloric acid, carbon tetrachloride, and the chloro acetic acids were promoters of tin (Weller et al., 1951). When different chemical formations of tin compounds with ammonium chloride were tested, it was found that their catalytic activities are the same. Zinc and iron were the other metallic compounds, the catalytic activities of which were investigated at initial low H<sub>2</sub> pressure. Zinc showed moderate catalytic activity in the presence of ammonium chloride while no catalytic effect was observed for iron based components. On the other hand, high pressure tests indicated that iron based catalysts, such as ferrous sulfate, pyrite, and “red mud,” had the favorable effects, though high pressure reduced promoting effects of tin and zinc in the presence of ammonium chloride. When the ammonium chloride content in the presence of tin or zinc was tested, the production of asphalt, which is an intermediate and undesired product, decreased with the moderate amount of ammonium chloride. To sum up, tin and tin sulfide was found as equally effective catalysts while ammonium chloride did not show any catalytic activity alone. On the other hand, the synergetic effect between the tin and ammonium chloride or tin sulfide and ammonium chloride led to higher liquefaction and/or lower asphalt production. In addition, hydroiodic acid showed the unique catalytic performance among halogen acids (Weller et al., 1951).

In another article, by the same group, the distribution of catalyst on the reactivity was discussed. The coal and catalyst combination can be formed in two ways: the first is impregnation of coal with catalyst from solution and the second is spraying of the coal powders with catalyst solution. The second one is more feasible for big coal plants but catalyst solubility is necessary for this process (Weller and Pelipetz, 1951).

Guin et al. (1978) reported the catalytic effects of coal minerals on the coal hydrogenation and hydrodesulfurization processes; they demonstrated the catalytic activity of especially iron based minerals in the presence of creosote oil in the solvent recycle process (Guin et al., 1978). They defined the reaction rate-limiting step as the transfer of hydrogen to the donor solvent. Silica and alumina are in the coal structure and they are known as hydrocarbon cracking catalysts. On the other hand, cobalt-molybdenum-alumina catalyst is a commercial hydrodesulfurization catalyst. In their study, both cracking and hydrodesulfurization reactions were investigated together in the presence of iron-based catalysts. In general, metal sulfide catalysts are used as hydrogenation and hydrodesulfurization processes of petroleum fractions. The defects in crystal lattice were considered as the responsible parts of catalytic activity. Therefore, the presence of metal sulfide active sites in the structure increases the process efficiency. Since pyrite (FeS) is a metal sulfide present in the coal structure, they analyzed the catalytic activity of the pyrite in hydrogenation and hydrodesulfurization processes. They obtained a higher reaction rate in the presence of pyrite during hydrogenation process. However, they did not observe any differences in the desulfurization activity in the presence and in the absence of pyrite. They interpreted this

result that pyrite is an ineffective desulfurization catalyst since it allows the conversion from FeS to H<sub>2</sub>S (Guin et al., 1978).

In summary, there are four main technologies in coal industry, pyrolysis, combustion, gasification, and liquefaction. In order to determine which technology is the most suitable for the special type of coal, it is necessary to identify the chemical and physical structure of coal initially. Additionally, in order to predict the efficiency and environmental damages during each process, the composition of the solid residue and gaseous products should be defined properly.

## CHAPTER 3

### EXPERIMENTAL STUDIES

#### 3.1. Introduction

This chapter is organized to explain the materials and methods used in this study. Detailed descriptions of the coal characterization techniques are presented. This is followed by the methods used to test the coal reactivity during pyrolysis, oxidation and gasification.

Classical and modern characterization techniques reveal the functional groups and elemental composition of coal. Conventional analyses such as proximate analysis and ultimate analysis, assume coal as a homogenous material and they provide only bulk properties. Proximate analysis includes moisture, ash, volatile matter, and fixed carbon in coal. The ultimate analysis describes the elemental composition of coal. The most favorable advantage of this analysis is to estimate the maximum emission of sulfur and nitrogen oxides during the combustion. Inorganic matter in coal is expressed in the form of ash. Aluminum, silicon, iron, calcium, magnesium, sodium and sulfur are the main elemental mineral matter in the ash structure. X-ray fluorescence spectroscopy makes it possible to determine the amounts of these mineral matters. X-ray Diffraction is used to monitor the crystalline structure. The spectroscopic methods such as, DRIFTS and  $^1\text{H}$ ,  $^{13}\text{C}$  NMR spectroscopy can provide information on the organic structure of coal.

Four main coal conversion processes monitored in this study are pyrolysis, oxidation, hydrogenation and hydrothermal treatment. The specific details of testing procedures are described and some of the techniques mentioned above were used to characterize the carbon residue after each process.

#### 3.2. Coal Preparation and Characterization

##### 3.2.1 Preparation of coal samples

The coal sample used in this study was donated from Turkish Coal Enterprises (TKI) Tuncbilek Lignite Establishment in Turkey. To obtain a representative sample, 25 kg coal sample was crushed in a grinder, spread on a flat surface, and divided into four equal parts. After two parts were discarded, the remaining parts were mixed and the same process was repeated until 1 kg sample remained. Subsequently, the final sample was sieved to obtain particles of maximum 150  $\mu\text{m}$ . Since the sample was left to dry several months prior to processing, the reported results will be identified as dry basis.

### **3.2.2 Classical coal analysis**

Three identical samples were used for the proximate and ultimate analyses, and the average results of the three measurements were reported. Proximate analysis, ultimate analysis, and the Eschka method were used to characterize Tuncbilek lignite in two parallel experiments. In addition to the above analyses, the heating value of the lignite was measured by using a bomb calorimeter (Gallenkamp Autobomb, CAB001.AB1.C).

#### **3.2.2.1 Proximate Analysis**

In proximate analysis, moisture, volatile matter, and ash composition of the lignite samples were determined according to ASTM D-3173, D-3174, and D-3175 standards, respectively. This analysis is based on the gravimetric changes. The moisture content is the weight difference after 1 gram of sample is heated to 107°C for one hour. When the volatile matter is measured, sample in a crucible is held at 900°C for approximately 7 hr. Since ash is the combustion residue of the coal, the percentage of ash is the decrease of the weight after 1g coal is burned at 825°C. The subtraction of total amount of moisture, volatile, and ash from 100 gives the relative amount of fixed carbon of the coal sample (Speight, 2005).

#### **3.2.2.2 Ultimate Analysis**

For the ultimate analysis, a LECO-CHNS-932 analyzer at METU central laboratory was used to determine the carbon, hydrogen, nitrogen, and sulfur contents of the lignite. 15 mg sample is used for the analysis.

#### **3.2.2.3 Sulfur Determination with Eschka Analysis**

The sulfur composition was also determined with the Eschka method (ASTM 3177) (Speight, 2005). The analysis details are as follows:

1 gram 100 mesh Tuncbilek lignite is mixed with 3 g Eschka (the mixture of 2 unit MgO and 1 unit Na<sub>2</sub>CO<sub>3</sub>). The mixture is placed in a porcelain crucible, after the crucible inside is covered by ~ 3 g pure Eschka. The top surface of the sample is again covered by Eschka. The crucible is heated up to 825°C and held at this temperature for 2hr. After cooling, crucible is taken in a 400 ml beaker and 100 ml water is added. In order to oxidize the sulfur in solution 25 ml HCl is added until a yellow color was obtained. In addition to the HCl, 1 ml H<sub>2</sub>O<sub>2</sub> was added to oxidize iron present in the solution. Solution was boiled and waited till all tiny bubbles disappear. Solid particles are removed by filtration. 2-3 drop methyl orange (indicator) is dropped to the remaining solution and NH<sub>3</sub> addition allows the color change. Thus, it is possible to precipitate the particles with the exception of iron. After filtration, HCl is added to the basic solution until color turns to orange or yellow. Final solution should be acidic. The solution is boiled and 25 ml 10% BaCl<sub>2</sub> is added while stirring. The solution was kept 30 min at the same temperature, and left overnight at room temperature to form BaSO<sub>4</sub> precipitates.

BaSO<sub>4</sub> is filtered and filtrate is washed till no chlorine ions remained in solution. The presence of Cl<sup>-</sup> in solution can be tested by AgNO<sub>3</sub>. The filter paper with precipitate is burned at 825°C for at least 30 min. The weight difference of crucible between the initial and final gave the BaSO<sub>4</sub> amount.

$$\text{Total sulfur \%} = \frac{\text{Weight of BaSO}_4 \text{ (s)}}{\text{Weight of coal sample (g)}} \times \frac{32 \text{ g/mol sulfur}}{234 \text{ g/mol BaSO}_4} \dots\dots(\text{Eqn. 1})$$

### 3.2.2.4 Pyritic, Sulfate and Organic Sulfur Analysis

Approximately 2 g of lignite sample is placed into a beaker. 3ml (1/3 vol:vol) ethanol and then, 50 ml (1/3 vol) HCl are added. Beaker is covered by a watch glass and it is boiled for 20 min. After cooling to room temperature, the main solution is filtered and filtrate is washed several times until all Cl<sup>-</sup> ions are removed. The precipitate part is used to determine pyritic sulfur while the filtrate part is used for SO<sub>4</sub><sup>-</sup> analysis.

#### *i. Sulfate analysis*

1ml H<sub>2</sub>O<sub>2</sub> is added to the filtrate part of the main solution to oxidize iron in the solution. Solution is heated to boiling temperature and colored by 1-2 drops methyl orange. Boiling continues until tiny bubbles disappear. Then, 25 ml NH<sub>4</sub>OH is added to solution till precipitate forms. Solution was removed from heater. After waiting for 20 min, filtration and washing processes are completed. The volume of the liquid part or filtrate including sulfur is completed to 200 ml with water. Solution is colored by 2-3 drops methyl orange which is the best indicator of the acidity. This basic solution is acidified with 2/1 HCl till pH is 1. The color change from orange to yellow indicates the final pH values of 1. 25 ml 10% BaCl<sub>2</sub> solution is added and solution is boiled. Solution is kept overnight so that all SO<sub>4</sub><sup>-</sup> precipitate. Then solution is filtered and washed with water 6 times. Filter with its content is put in the porcelain crucible and burned at 825°C. The weight difference of crucible between the initial and final gives the BaSO<sub>4</sub> amount. Sulfate percentage is calculated again by Equation 1.

#### *ii. Pyritic sulfur analysis*

The precipitate part of the main solution, is put into a beaker. It is mixed with 100 ml 25% HNO<sub>3</sub> by magnetic stirrer for 12-24 hr. Solution is filtered and washed with cold water. Fe in solution is oxidized by 2 ml 30% H<sub>2</sub>O<sub>2</sub> by boiling the solution for 5 min. This acidic solution turns to the basic with the NH<sub>4</sub>OH addition until precipitation occurs. The solution is filtered and the filtrate is washed 6 times. Filter paper is washed with 20 ml HCl and hot water. Final solution must be yellow. The solution is boiled and SnCl<sub>2</sub> is added till a colorless solution is obtained. Then, solution is cooled immediately in an ice-water bed. 10 ml HgCl<sub>2</sub> and Zimmer solution (the mixture of 67g MnSO<sub>4</sub>.4H<sub>2</sub>O, 500 ml water, 138 ml H<sub>3</sub>PO<sub>4</sub>) are added by stirring the solution. The last step is titration with 0.02N KMnO<sub>4</sub>. Titration is completed when the color of the solution turn to light pink. The amount of pyritic sulfur can be calculated by the following formula.

$$\text{Pyritic sulfur \%} = \frac{V_{\text{KMnO}_4} \times 10^{-3}(\text{l}) \times N_{\text{KMnO}_4}}{\text{Weight of coal sample (g)}} \times \frac{56 \text{ g Fe}}{1 \text{ N KMnO}_4} \times \frac{64 \text{ g S}_2}{56 \text{ g Fe}} \dots\dots(\text{Eqn. 2})$$

**iii. Organic sulfur**

Sulfur is present in coal structure in three forms namely, pyritic, sulfate, and organic. When the amount of pyritic and sulfate sulfur is subtracted from total sulfur amount, the remaining gives the organic sulfur amount.

$$\text{Organic sulfur \%} = \text{total sulfur} - (\text{pyritic sulfur} + \text{sulfate}) \dots (\text{Eqn. 3})$$

**3.2.2.5 Calorific Value Calculation (ASTM D-2015)**

The heating value of the lignite was measured by using a bomb calorimeter (Gallenkamp Autobomb, CAB001.AB1.C). The working principle of the calorimeter is based on the energy release when 1 gram of coal is burned in a calorimeter bomb. When coal is burned in calorimeter bomb, all heat was taken by the 2.1 ml well insulated water reservoir. Well-insulation prevents the heat loss from outer surface. Thus, calorific value of coal is calculated by using the following formula.

$$\text{Calorific Value (cal/g)} = \frac{\text{Calorimeter calibration constant}}{\text{Weight of coal sample (g)}} \times \Delta T \dots (\text{Eqn. 4})$$

**3.2.3 Volatiles and ash analyses by TGA**

Thermal Gravimetric Analysis (TGA) (Shimadzu DTG 60H) experiments were conducted at a temperature between 25°C and 900°C with a heating rate of 10°C/min under 60 cc/min N<sub>2</sub> flow for pyrolysis and 60 cc/min air flow for oxidation processes in order to analyze the volatile and ash compositions of the lignite samples, respectively.

**3.2.4 Analysis of Inorganic structure by XRF**

X-ray Fluorescence (XRF) spectroscopy analyses were carried out on a Rigaku ZSX Primus II X-ray spectrometer to analyze mineral contents of the lignite. In this technique, lignite sample is mixed with wax binder in a weight ratio of 4:1 and the mixture is pressed under 15 tons into pellets with a diameter of 32 mm.

**3.2.5 Monitoring of inorganic structure by XRD**

These analyses were obtained by using a Philips model PW1840 (1729) X-ray diffractometer with Ni filtered Cu-K $\alpha$  radiation at a scan rate of 0.05°/sec. XRD

measurements were performed in the range of 5° to 90° (2 $\theta$ ). The diffractometer was operated at 30kV and 24 mA.

### **3.2.6 DRIFT spectroscopy**

The bulk properties of Tuncbilek lignite were analyzed qualitatively by Perkin Elmer Spectrum 100 FTIR spectrometry in diffuse reflectance mode. After the sample was diluted with a non-absorbing material (KBr), the mixture was placed in a sample holder. 16 scans were collected with 4 cm<sup>-1</sup> resolution in the range of 4000-450 cm<sup>-1</sup>.

### **3.2.7 NMR spectroscopy**

<sup>1</sup>H Magic Angle Spinning (MAS) and <sup>13</sup>C Cross Polarization Magic Angle Spinning (CPMAS) measurements were performed using an Apollo spectrometer (Tecmag, Houston, TX). The proton channel of the probe was tuned to 299.79 MHz while 75.39 MHz tuning was employed for the carbon channel of the probe. A 4 mm Doty Scientific probe (DSI-1231) capable of spinning the samples up to 15 kHz were used for both proton and carbon CP-MAS measurements.

## **3.3 Coal Processes Methodology**

### **3.3.1 Pyrolysis and Oxidation Experiments**

The experimental set-up used for the pyrolysis and oxidation reactions are demonstrated in Figure 3.1. Approximately 500 mg lignite sample was placed in a quartz reactor and fastened by quartz wool at both ends. The reactor was placed in a home built furnace with temperature control. Mass flow controllers (Teledyne) were used for the desired gaseous feed flow rates. Pyrolysis experiment was conducted under 200 cc/min N<sub>2</sub> flow in the temperature range of 40°C-800°C. Pyrolysis residue of lignite sample was taken after reactor was cooled to room temperature. The oxidation residue of Tuncbilek lignite was prepared by heating the sample from 40°C to 800°C at a rate of 5°C/min under 200 cc/min air flow. After cooling, solid product, remaining in the reactor was collected as the oxidation residue. During these reaction tests, CO, CO<sub>2</sub>, CH<sub>4</sub>, and H<sub>2</sub> formation rates were monitored by a gas chromatograph (HP 4890A) connected on line to the reactor equipped with a Porapak Q column. All of the residual products were analyzed by XRD, DRIFTS, <sup>1</sup>H and <sup>13</sup>C-NMR spectroscopy.

### **3.3.2 Hydrogenation Experiments**

Hydrogenation experiments were conducted in the same experimental set-up. As seen in Figure 3.2, the difference is just in the gas analysis part. Since high amounts of tar formation is observed during hydrogenation, gaseous species were not sent to the GC in order not to contaminate the transfer units. Instead, gaseous products passed through a u-tube filled by glass fractures. Commercial PbO or ZnO were also mixed with glass

fractures in order to observe the sulfur adsorption ability of these oxides. Temperature in reactor was increased from 40°C to 800°C under 5°C/min temperature ramp. High purity N<sub>2</sub> and H<sub>2</sub> gases supplied from Oksan were sent to the reactor after adjusting the flow rates by mass flow controllers (Teledyne). During hydrogenation, total flow rate was kept at 50 cc/min. H<sub>2</sub> was blended with N<sub>2</sub> at this total flow rate in order to observe the effect of hydrogen concentration on the sulfur removal in coal structure. The sulfur content of the carbon residue was determined by a CHNS analyzer. Structural changes were monitored by XRD, <sup>1</sup>H and <sup>13</sup>C-NMR spectroscopy and DRIFTS.

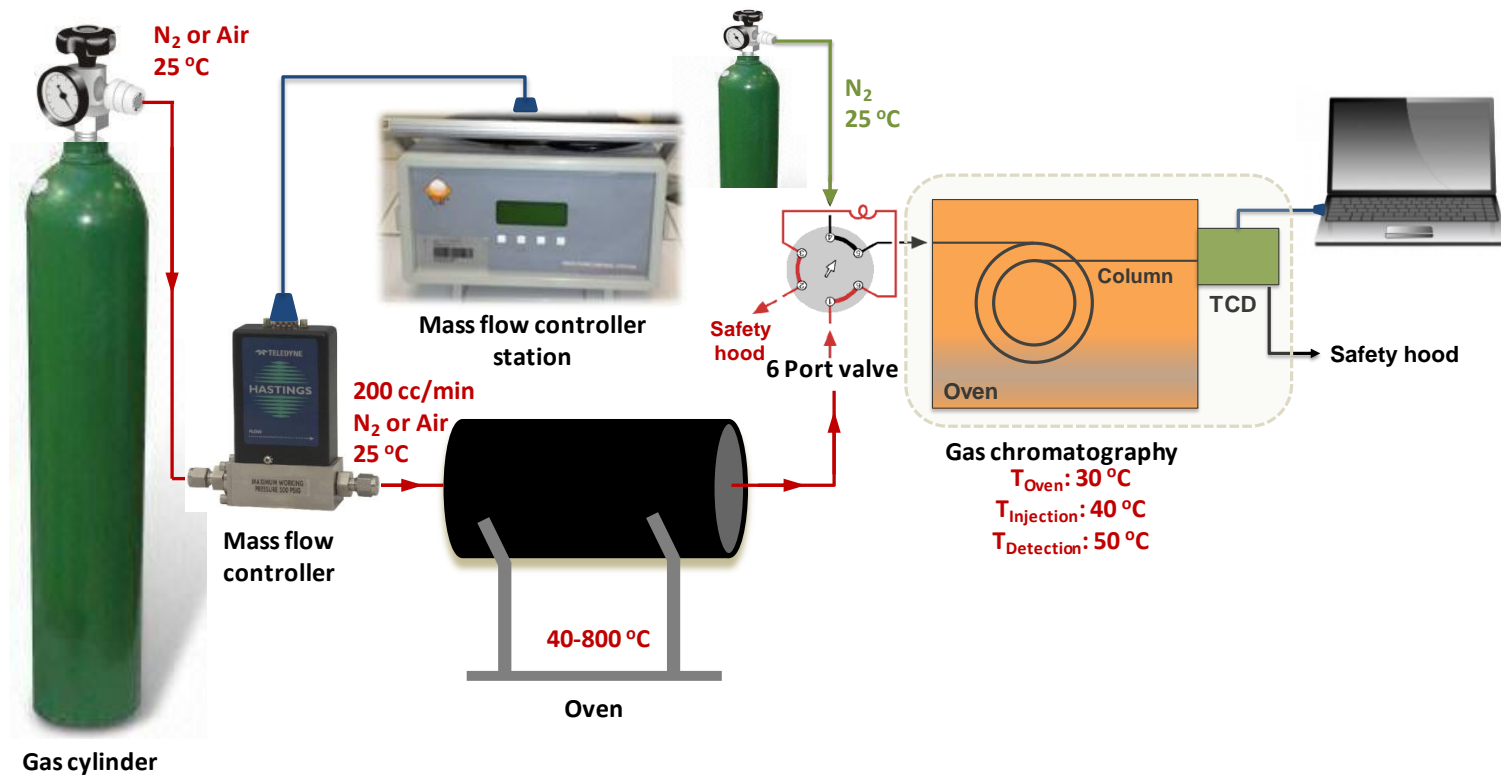


Figure 3.1. Schematic representation of experimental set up for pyrolysis and oxidation reaction tests.

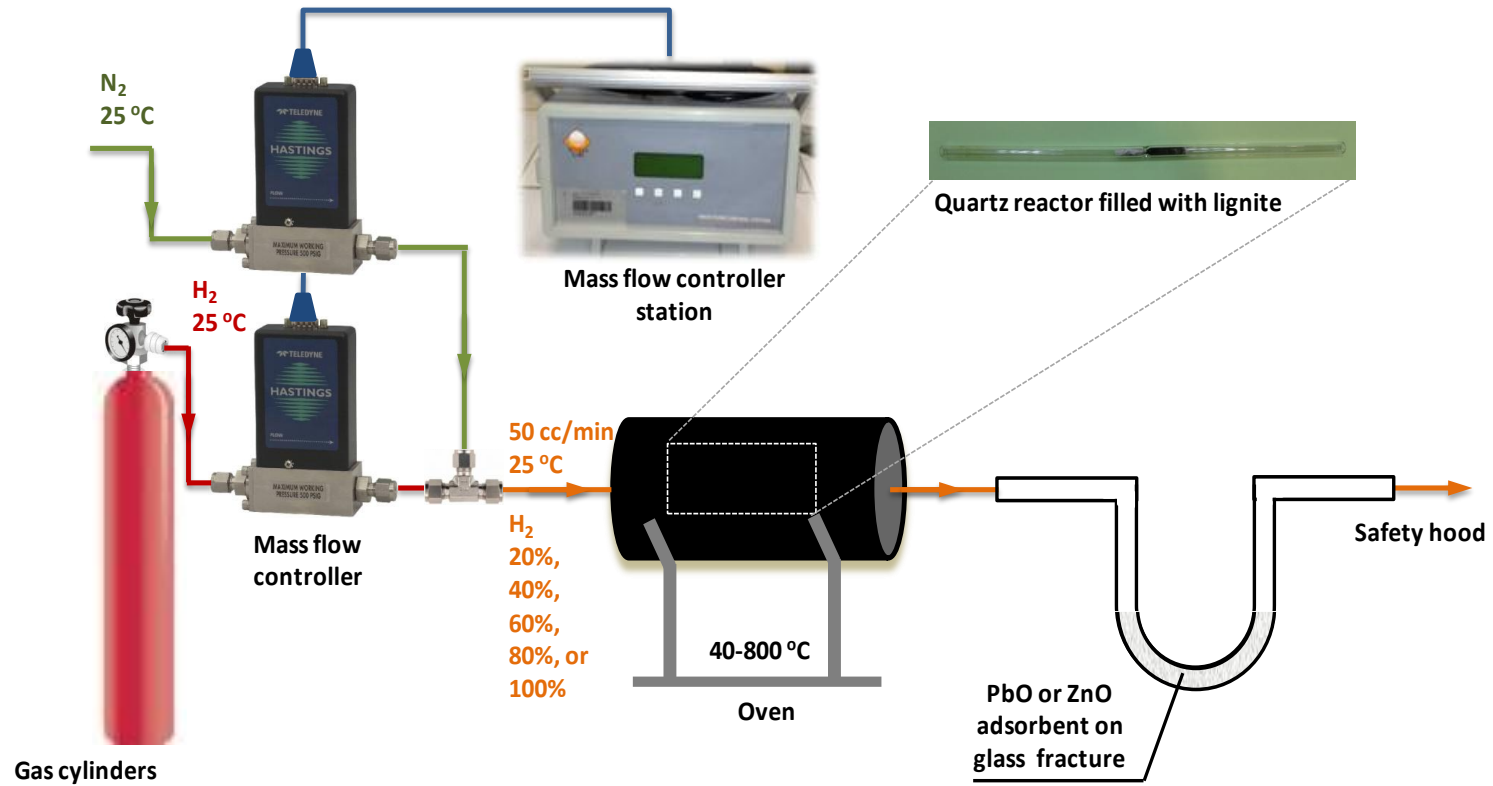


Figure 3.2. Schematic representation of experimental set up for hydrogenation reaction tests.

### 3.3.3 Wet Air Oxidation Experiments

In this part, oxy-desulfurization experiments were carried out in a 113 ml capacity, stainless steel homemade autoclave equipped with Teflon liners. The schematic design of the system is presented in Figure 3.3. Three experimental parameters (time, initial pressure, and temperature) were examined in this set-up. Approximately 5 grams of coal and 20 ml water were placed in the reactor and the system was heated up to 150°C and 5 bars final pressure. Seven different experiments were conducted as such by changing the duration of the experiment (0 min, 15 min, 30 min, 1h, 3h, 5h, and 7h). The initial (0 min) data point was collected immediately after the system reached 150°C and five bars final pressure.

In the second part of the study, the effect of O<sub>2</sub> partial pressure and temperature were investigated. 5 g coal and 50 ml water were put into the reactor and pressurized air at four different total pressure values (1, 2, 5, and 6 bars) were compressed into the autoclave. The reaction tests were conducted at 150°C. On the other hand, the effect of temperature was examined by pressurizing the system with air to five bars initially and carrying out the reaction tests at 150, 160, 165, 170, and 180°C. The system was maintained under these conditions for 15 minutes for all experiments. The sulfur composition of solid residues was determined by both Eschka analysis and ultimate analysis. Since coal crystalline structure has also changed during oxy-desulfurization, the elimination of pyritic sulfur in residual carbon was followed by the X-ray diffraction spectroscopy. In addition, -SO<sub>4</sub><sup>=</sup> formation in liquid residue was determined by using gravimetric technique. For this aim, 10 ml sample was taken and their volume was completed to 200 ml by water. Solution is colored by 2-3 drops methyl orange. This basic solution was acidified with 2/1 HCl till pH is 1. 25 ml 10% BaCl<sub>2</sub> solution was added and solution was boiled. Solution was rested overnight so that all SO<sub>4</sub><sup>=</sup> precipitate. Then solution was filtered and washed with water 6 times. Filter with its content was put in the porcelain crucible and burned at 825°C. The weight difference of crucible between the initial and final gave the BaSO<sub>4</sub> amount. Total sulfur percentage was calculated by Equation 1 on page 25. Calorific values of the residual carbons were also measured as part of this study.

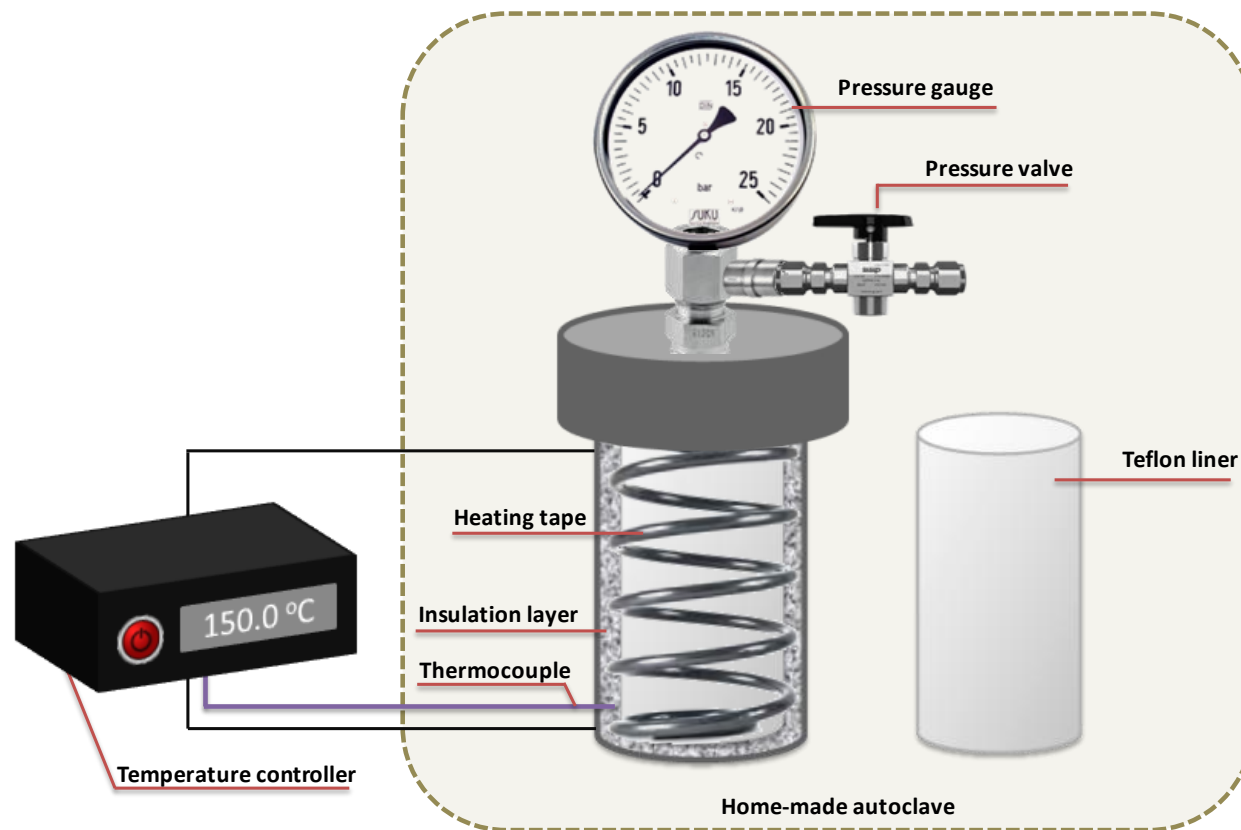


Figure 3.3. Schematic representation of experimental set up for oxy-desulfurization reaction tests.

## CHAPTER 4

### CHARACTERIZATION OF TUNCBILEK LIGNITES

#### 4.1. Introduction

Heterogeneity of coal structure requires several characterization methods for a thorough analysis. Therefore, proximate, ultimate and Thermogravimetric analyses were used to analyze the composition of the lignite sample. In addition to these analyses, XRF spectroscopy was used to determine the slag composition. X-ray diffractometer was used to monitor the crystalline structure of Tuncbilek lignite. To provide the information about the chemical structure, DRIFT and solid-state NMR spectroscopic methods were employed. The results were evaluated as an average of three independent measurements whenever possible.

The gasification reactivity of coal increases with decreasing coal rank. Lignite, as a low rank coal, is an important raw material for gasification technology. During gasification, a complex reaction network prevails. The cold solid, upon entering the reactor undergoes pyrolysis and subsequently char gasification. Pyrolysis is a thermal decomposition process-taking place between 300°C -500°C. During the pyrolysis step, H<sub>2</sub> rich volatile and aliphatic carbon fractions are removed from coal. The remaining part is fixed carbon (coal char) and ash. Coal char is more aromatic and more stable than raw sample (Molina and Mondragon, 1998, Sekine et al., 2006). The decomposition reactions of the char are dependent on the gaseous species and reaction conditions (Molina et al. 1998). As seen in Table 2.1, endothermic dry reforming and steam reforming reactions, and exothermic oxidation, water gas shift and hydrogenation reactions are possible reactions taking place during char gasification. The exothermic oxidation reaction meets the heat requirement of dry reforming of methane and steam reforming reactions. Moreover, the presence of high amounts of steam allows the water gas shift reaction, while carbon hydrogenation reaction occurs under high pressure condition (Molina and Mondragon, 1998).

Since the physical and chemical properties of coal determine its processing fate, a detailed characterization is very important prior to any coal carbonization, oxidation, and gasification and/or liquefaction. Currently, utilization of a large array of characterization techniques provides the most reliable information about the coal reactivity (Gupta, 2007). Gupta (2007) suggests that classical coal analyses (proximate, ultimate and Eschka) do not provide sufficient information about the relation between coal structure and reactivity due to the assumed homogenous structure of coal. On the other hand, Fourier transform infrared (FTIR) and <sup>13</sup>C NMR spectroscopy prove to be useful to describe the organic structure of coal.

Coal structure is shown to have organic (volatile and fixed carbon) and inorganic (ash) fractions (Molina and Mondragon, 1998, Sekine et al., 2006). During the pyrolysis, gasification and/or liquefaction processes, the more reactive volatile and aliphatic carbon fractions in the structure are removed at relatively low temperatures. The remaining part is coal char with highly ordered structure and less reactivity. The decrease in char reactivity is generally considered to be due to the decrease in surface area and in the number of active sites during heating (Kucukbayrak et al., 2001, Feng et al., 2003, Arenillas et al., 2004, Lu et al., 2001, Lu et al., 2002).

Kucukbayrak et al. (2001) investigated combustion reactivity of Turkish lignite by proximate and ultimate analyses and showed the change in surface area by BET measurement. They found that during the devolatilization, coal pores are opened and new pores formed. Since oxidation reaction takes place at the pore surface, O<sub>2</sub> can enter the pore easily and increase the reaction kinetics. As the reaction progresses, the particles shrink, their surface area decreases and their reactivity drops. Feng et al. (2003) used high-resolution transmission electron microscopy (HRTEM) to monitor structural ordering and X-ray diffraction (XRD) in order to monitor the crystal structures of various coals during gasification under air and CO<sub>2</sub> flows. They showed that since closed micropores open more slowly under CO<sub>2</sub> flow than air flow, the more ordered crystal structure could be obtained easily during the air gasification. Arenillas et al. (2004) determined the reactivity loss during the thermal treatment by TGA. In addition, they showed the decrease in surface area and carbon active sites by BET. Lu, Sahajwalla et al. (2002) used Quantitative X-ray Analysis (QXRDA) and HRTEM to determine the coal reactivity during pyrolysis and oxidation processes. The QXRDA results indicated that the average crystal size of coal chars and aromatic fraction increase during oxidation, which leads to decrease in char reactivity. A more regular coal structure is monitored under the conditions of higher pyrolysis temperature and a lower heating rate by HRTEM (Lu et al., 2002). Since aliphatic groups and amorphous carbon are removed during pyrolysis and oxidation processes, these parts can be defined as the reactive part of the coal (Lu et al., 2002, Arenillas et al., 2004).

## **4.2 Results and Discussions**

### **4.2.1 Classical Coal Characterizations-Proximate and Ultimate Analyses**

Table 4.1 presents the gathered data from the proximate analysis and Eschka analysis of lignite. Four components of coal, consisting of moisture, ash, volatile matter, and fixed carbon were determined by the analysis. Inorganic matter in coal is expressed in the form of ash. As given in Table 4.1, the volatile matter of coal sample is about 28% while ash content in coal was determined as 38% by weight. The total amounts of sulfur were determined by Eschka method as  $3.9 \pm 0.2\%$  by weight. Table 4.2 shows the sulfur composition of Tuncbilek lignite. The heating value of lignite sample is obtained as  $3680 \pm 60$  cal/g.

Table 4.1. Coal composition from the proximate analysis on air dried basis.

	Weight %
Moisture	$4.7 \pm 0.9$
Ash	$37.9 \pm 0.2$
Volatile matter	$27.9 \pm 0.1$
Fixed carbon	$29.5 \pm 0.1$

Table 4.2. Sulfur composition of coal determined by Eschka analysis on air-dried basis.

	Weight %
Total sulfur	$3.9 \pm 0.2$
Pyritic sulfur	$2.6 \pm 0.1$
Sulfates	$1.2 \pm 0.1$
Organic sulfur	$0.1 \pm 0.1$

The results of ultimate analysis are presented in Table 4.3. As seen in this table, the relative amount of carbon is  $37.7 \pm 0.7$  wt% in coal. Hydrogen and nitrogen contents of coal are  $3.6 \pm 0.1$  and  $1.6 \pm 0.1$  wt%, respectively, while sulfur content of coal is  $5.4 \pm 0.6$  wt%.

Table 4.3. Coal composition from the ultimate analysis on air-dried basis.

Elements	Weight %
Carbon	$37.7 \pm 0.7$
Hydrogen	$3.6 \pm 0.1$
Nitrogen	$1.6 \pm 0.1$
Sulfur	$5.4 \pm 0.6$

The results of these analyses indicated that Tuncbilek lignite was high in ash and sulfur contents but low in calorific value.

#### 4.2.2 Thermal Gravimetric Analysis TGA analysis under N<sub>2</sub> and air flow

The TGA thermogram of lignite under N<sub>2</sub> flow is shown in Figure 4.1. 5% weight loss at 100°C corresponds to the relative amount of moisture determined by proximate analysis. Since TGA analysis performed under the inert atmosphere represents the pyrolysis process, the remaining 28% weight loss represents the volatile content of coal. The derivative curve of the weight loss indicated that maximum weight loss occurred at 450°C.

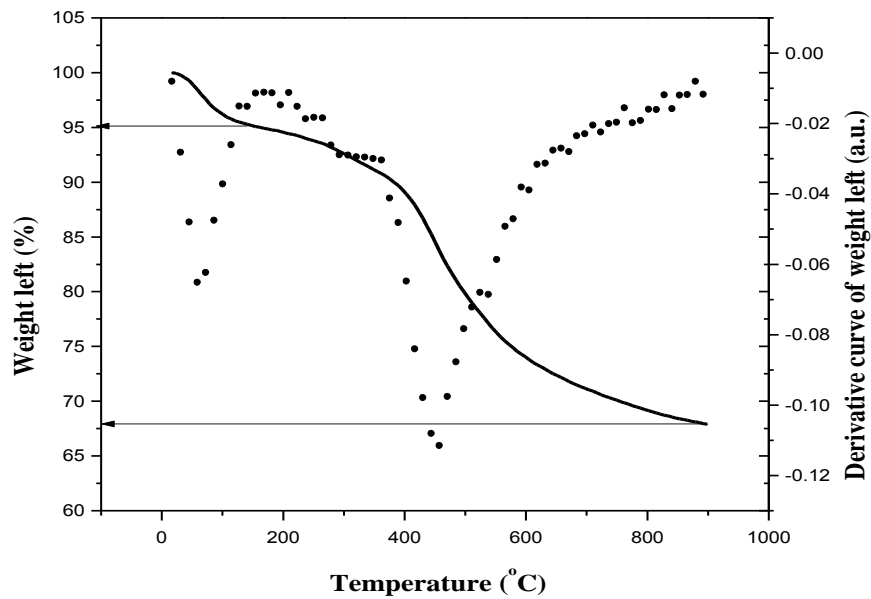


Figure 4.1. TGA and DTG curves of coal sample under N<sub>2</sub> flow. Solid line represents the TGA, while dotted line represents the DTG.

The oxidation in air thermogram of the same sample is presented in Figure 4.2. The moisture content is consistent with the results presented in Figure 4.1. The final percentage of mass (~38%) left in the pan corresponds to the ash value obtained from proximate analysis. In addition, maximum weight loss was recorded at about 480°C during oxidation.

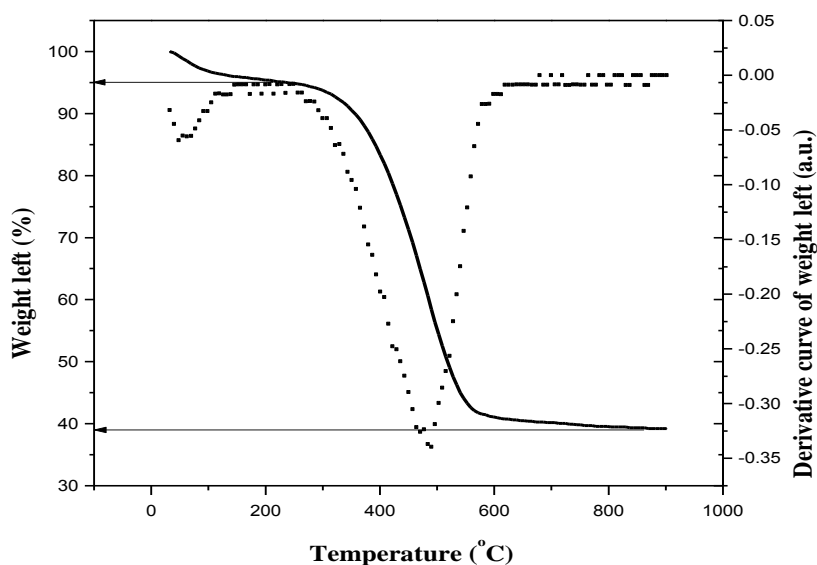


Figure 4.2. TGA and DTG curves of coal sample under air flow. Solid line represents the TGA, while dotted line represents the DTG.

#### 4.2.3 XRF

Three major components of ash in Tuncbilek lignite is shown in Table 4.4. SiO<sub>2</sub> is the main component in the ash structure, and the relative amount is about 53.6 ± 0.4 wt%. Al<sub>2</sub>O<sub>3</sub> (24.9 ± 0.2 wt%) and Fe<sub>2</sub>O<sub>3</sub> (13.0 ± 0.1 wt%) are the other important components in the ash of coal. The remaining fractions of ash are listed as B<sub>2</sub>O<sub>3</sub> (~2.2%), MgO (~1.9%), K<sub>2</sub>O (~1.2%), SO<sub>3</sub> (~0.9%) and CaO (~0.8%).

Table 4.4. Inorganic composition of coal determined by XRF.

Coal inorganics	(% Weight)
SiO <sub>2</sub>	53.6 ± 0.4
Fe <sub>2</sub> O <sub>3</sub>	13.0 ± 0.1
Al <sub>2</sub> O <sub>3</sub>	24.9 ± 0.2
MgO	1.9 ± 0.1
CaO	0.8 ± 0.0
Na <sub>2</sub> O	0.1 ± 0.0
K <sub>2</sub> O	1.2 ± 0.0
B <sub>2</sub> O <sub>3</sub>	2.2 ± 0.1
SO <sub>3</sub>	0.9 ± 0.1

#### 4.2.4 XRD

When coal characterization was conducted by XRD, two main peaks were observed between  $20^\circ$  and  $27^\circ$  due to carbon found in coal (Figure 4.3). The peak around  $20^\circ$  is related to carbons derived from aliphatic chains while the peak at  $27^\circ$  represents the crystalline carbon structure (Maity and Mukherjee, 2006, Saikia et al., 2007a, Sekine et al., 2006).

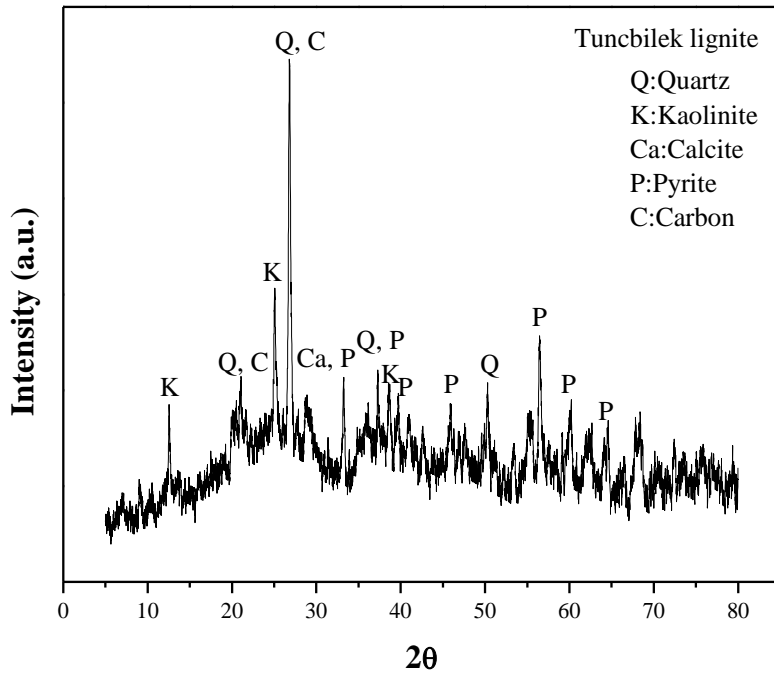


Figure 4.3. XRD pattern of Tuncbilek lignite.

The major inorganic components present in coal and their characteristic Bragg angle values are summarized in Table 4.5. XRD pattern of unprocessed coal and inorganic coal compositions reveal that quartz, kaolinite, calcite, and pyrite are the major crystalline components. XRD pattern of cubic pyrites are observed around  $29^\circ$ ,  $33^\circ$ ,  $37^\circ$ ,  $41^\circ$ ,  $47^\circ$ ,  $56^\circ$ ,  $59^\circ$ ,  $61^\circ$ ,  $64^\circ$  (JCPDS CARD NO 42-1340) (Li et al., 2011, Kar and Chaudhuri, 2005, Meng et al., 2003, Wan et al., 2003, Liu et al., 2005).

Table 4.5. Characteristic peak positions of coal inorganic components.

Substances	2 $\theta$ ( $^{\circ}$ )	References
Kaolinite $\text{Al}_2\text{Si}_2\text{O}_5(\text{OH})_4$	13, 19, 25, 36,38	(Iglesias et al., 1998)
Quartz ( $\text{SiO}_2$ )	27, 21, 50, 37, 39	(Iglesias et al., 1998)
Pyrite ( $\text{FeS}_2$ )	29, 33, 37, 41, 47, 56, 59, 61, 64	(Li et al., 2011, Kar and Chaudhuri, 2005, Liu et al., 2005, Meng et al., 2003, Wan et al., 2003)
Calcite ( $\text{CaCO}_3$ )	29, 39	(Iglesias et al., 1998)
Dolomite ( $\text{CaMg}(\text{CO}_3)_2$ )	31, 41	(Gunasekaran and Anbalagan, 2007)

Since Tuncbilek lignite contains pyrite in high amounts, the characteristic XRD peaks of pyrite are of special interest for this study. By monitoring of the changes in these peaks, it is also possible to follow sulfur removal process.

#### 4.2.5 DRIFTS

Figure 4.4 represents the characteristic absorption bands of Tuncbilek lignite. The spectrum can be evaluated in four separate regions based on the absorption bands of the lignite sample.

In the first region ( $3800\text{-}3000\text{ cm}^{-1}$ ), the broad absorption band observed around  $3300\text{ cm}^{-1}$  originated from the OH-and NH stretching vibration of coal organic fraction (Saikia et al., 2007a), while the strong absorption bands around  $3700\text{-}3400\text{ cm}^{-1}$  were assigned to aluminum silicate hydroxide (kaolinite) (Iglesias et al., 1998, Saikia et al., 2007a). These strong absorption peaks are also interpreted by Wu (1994) as superficial hydroxyl groups within pyrite (Wu, 1994). The absorption bands of the unprocessed lignite in the second region (within  $3100\text{-}2000\text{ cm}^{-1}$ ) indicated the characteristic C-H stretching vibration in aliphatic structure at  $2950\text{-}2850\text{ cm}^{-1}$  (Saikia et al., 2007a, Saikia et al., 2007b).

An examination of the third region in the  $2000\text{-}1300\text{ cm}^{-1}$  range revealed two relatively broad bands near  $1500\text{-}1600\text{ cm}^{-1}$  assigned to aromatic C=C stretching (Cetinkaya and Yurum, 2000, 2013) and  $1400\text{ cm}^{-1}$  attributed to C-H stretching and bending of aliphatic components (Francioso O., 2007). The absorption range  $1790\text{-}1150\text{ cm}^{-1}$  is labeled as

protonated carboxylic (-COOH), carboxylate anion (-COO-), and ester carbonyl groups (-COOR) by Peuravuori et al. (2006).

In the last region (1300-400  $\text{cm}^{-1}$ ), the absorption bands around 1110-1034  $\text{cm}^{-1}$  indicate the C-O, C-C or C-O-C stretching vibrations as defined by Francioso (2007). In addition to organic structure, some absorption bands represent the coal inorganic contents within the same region. The absorption bands obtained within the range of 1095-1020  $\text{cm}^{-1}$  indicate the possible presence of Si-O-Si, while the absorption bands obtained within the range of 1110-1080  $\text{cm}^{-1}$  point at the presence of Si-O-C as is stated by Peuravuori et al. (2006). The distinct absorption bands noticed at 471 and 540  $\text{cm}^{-1}$  are attributed to the different types of silicates (Peuravuori et al., 2006). The bands near 1030  $\text{cm}^{-1}$ , 535  $\text{cm}^{-1}$ , 470  $\text{cm}^{-1}$ , and 430  $\text{cm}^{-1}$  showed the presence of any silicate (clay and quartz) (Cetinkaya and Yurum, 2000). Clays are also clearly identified from the OH stretching absorption around the 3800-3400  $\text{cm}^{-1}$  region. 3697  $\text{cm}^{-1}$  is the specific kaolinite band as are the 537 and 476  $\text{cm}^{-1}$  (Iglesias et al., 1998, Breen et al., 2008).

With a similar approach, pyrite absorption bands at 1438, 872, 707  $\text{cm}^{-1}$  are associated with  $\text{CO}_3^-$  within pyrites (Wang et al., 2010a, Wu, 1994). Wang et al. also defined the strong absorption band of sulfate in the range of 1130  $\text{cm}^{-1}$  and 1080  $\text{cm}^{-1}$ . Si-O bending vibration ionic sulfate bands are at 533-471  $\text{cm}^{-1}$  (Saikia, Boruah et al. 2007). Table 4.6 summarizes the characteristic absorption bands of coal components.

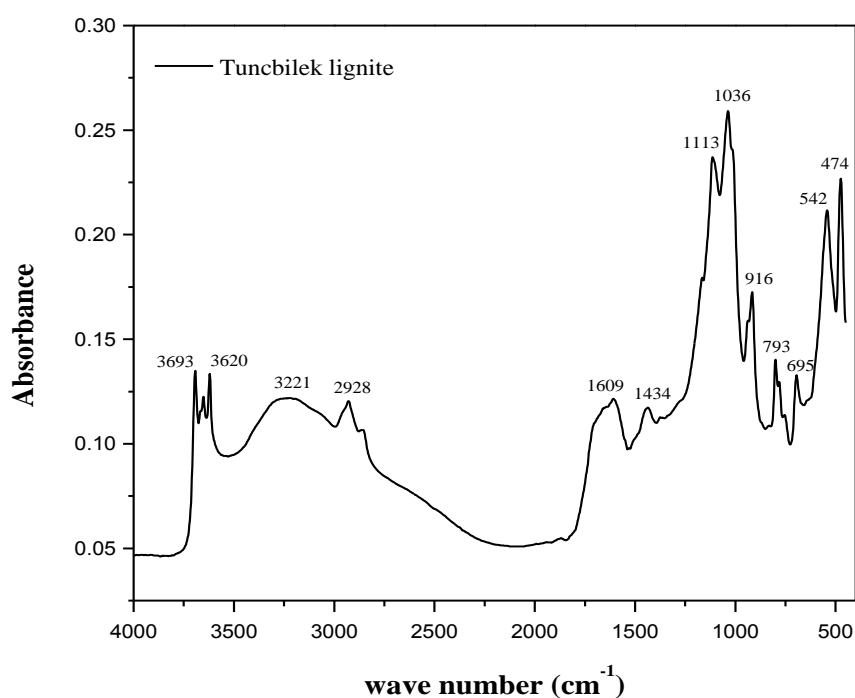


Figure 4.4. DRIFT spectrum of Tuncbilek lignite.

Table 4.6. Absorption bands of coal compounds.

Chemical structure	Frequency (cm <sup>-1</sup> )	Sources
-OH groups associated with clay minerals	3800-3400	(Saikia et al., 2007a, Iglesias et al., 1998)
-OH and -NH stretching vibrations	3853, 3752, 3622 and 3412	(Saikia et al., 2007a)
Aromatic C-H stretching band	3400-3100	(Saikia et al., 2007a)
Aliphatic CH stretching CH <sub>3</sub> , CH <sub>2</sub> , and CH groups	3100-2700	(Saikia et al., 2007a, Iglesias et al., 1998, Mursito et al., 2011)
C=O carbonyl stretching vibration and esters	1800-1600	(Saikia et al., 2007a, Iglesias et al., 1998, Mursito et al., 2011)
Aromatic C-C stretching	1600	(Cetinkaya and Yurum, 2000)
CH stretching and bending	1400	(Francioso O., 2007)
CH <sub>3</sub> asymmetric deformation and CH <sub>2</sub> group in bridges Aromatic C=C Strongly H <sub>2</sub> bonded OH	1436	(Saikia et al., 2007a)
CH <sub>3</sub> symmetric deformation -CH <sub>3</sub> and -CH <sub>2</sub> in cyclic structures	1372	(Saikia et al., 2007a)
Aromatic ring stretching vibrations	1490	(Mursito et al., 2011)
C-O-R structures of ethers	1150	(Mursito et al., 2011)
Aromatic structure Aromatic -CH out of plane bending	900-700	(Saikia et al., 2007a, Iglesias et al., 1998, Mursito et al., 2011)
Si-O-Si stretching vibration	1200-900	(Saikia et al., 2007a, Iglesias et al., 1998)
Si-O bending vibration Ionic sulfates	533-471	(Saikia et al., 2007a)
FeS <sub>2</sub>	420	(Saikia et al., 2007a)
Fe <sub>2</sub> O <sub>3</sub>	692	(Saikia et al., 2007a)
Kaolinite	537-476	(Iglesias et al., 1998, Breen et al., 2008)
Calcite and dolomite	1428, 878, 714	(Lavati, 2011, Gunasekaran and Anbalagan, 2007, Wilson, 1987)
-OH bond hydroxyl group in the organic structure of coal	3200-3400	(Iglesias et al., 1998, Mursito et al., 2011)
N-H bending N-H stretching N-O stretching	1660-1510 3500-3200 1550-1370	(Saikia et al., 2007a)

#### 4.2.6 Proton ( $^1\text{H}$ ) and Carbon ( $^{13}\text{C}$ ) NMR spectroscopy

In general, the peak positions on the  $^1\text{H}$  MAS NMR spectrum were identified to be non-polar alkyl (OCH) at  $\sim 2$  ppm (Delarosa et al., 1992, Sutcu et al., 2005), oxy-alkyl (CHO) at  $\sim 4$  ppm and aromatic protons at  $\sim 7$  ppm (Delarosa et al., 1992, Li et al., 2012, Sutcu et al., 2005). The  $^1\text{H}$  NMR spectrum of the unprocessed coal is presented in Figure 4.5. The red and blue lines were obtained by fitting Lorentzian curves with 99.2% verification. Figure 4.5 indicates two major peaks in coal structure at approximately 6.1 ppm and 1.0 ppm. The peak obtained around 1.0 ppm is considered to be an aliphatic proton evaluated in the range of 0.5-5 ppm (Sutcu et al., 2005). The second peak at 6.1 ppm is associated with aromatic protons in coal structures.

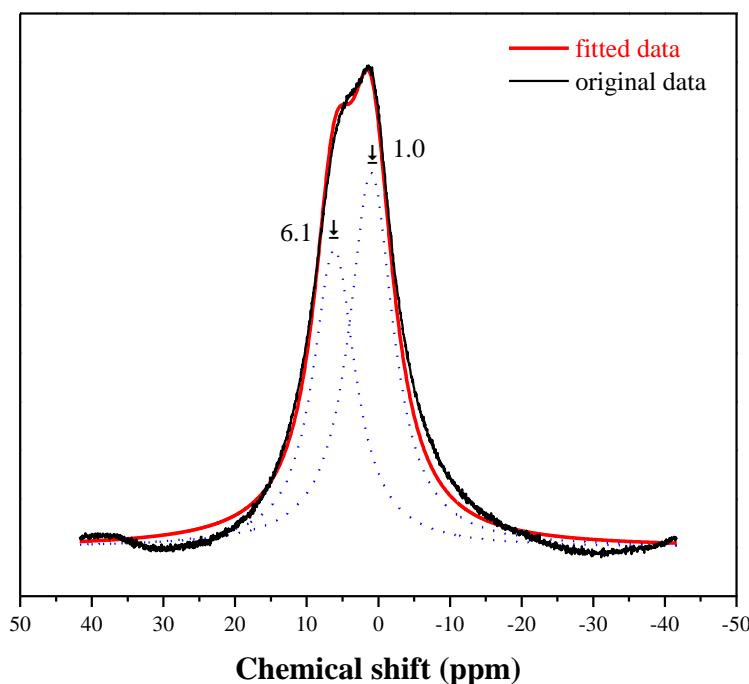


Figure 4.5. Proton NMR spectrum of Tuncbilek lignite.

The  $^{13}\text{C}$  CP-MAS NMR spectrum of the pure coal in Figure 4.6 includes two main signals indicating the aliphatic and aromatic hydrocarbon fractions of the lignite sample. In the aliphatic zone, the intense peak at approximately 20 ppm originates from the methyl ( $-\text{CH}_3$ ) groups (Simpson and Hatcher, 2004, Delarosa et al., 1992, Diaz and Blanco, 2003, Conte et al., 2002, Li et al., 2012, Kelemen et al., 2002). The largest peaks at 125 and 130 ppm are caused by protonated and non-protonated aromatic carbon structure, respectively (Orem et al., 1996, Simpson and Hatcher, 2004, Cook et al., 1996, Mao et al., 2010, Li et al., 2012, Delarosa et al., 1992, Conte et al., 2002, Kalaitzidis et al., 2006). The shoulders between 150 to 190 ppm are due to the oxygen bonded aromatic C-O (150-165 ppm), carbonyl, and  $\text{NC}=\text{O}$  groups (165-190 ppm) (Kalaitzidis et al., 2006, Keeler and Maciel, 2000, Azik et al., 1993, Conte et al., 2002, Delarosa et al., 1992).

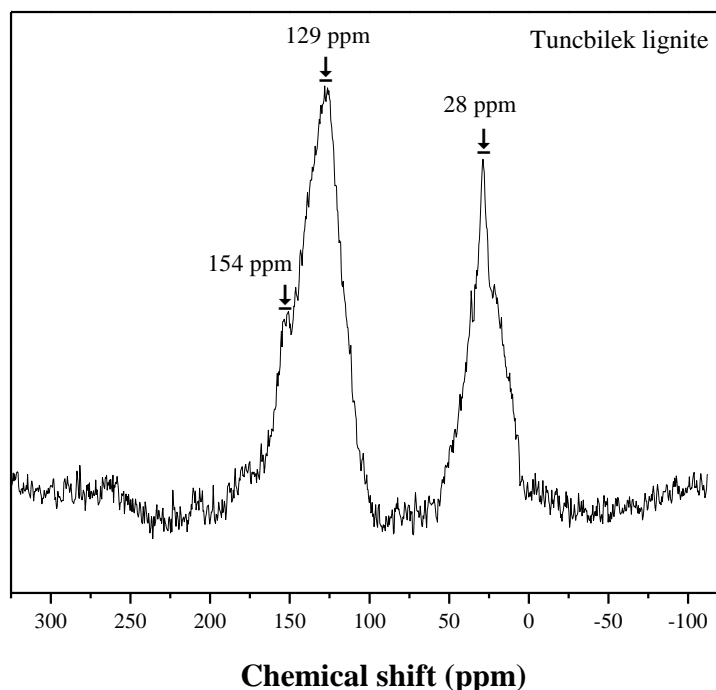


Figure 4.6. Carbon NMR spectrum of Tuncbilek lignite.

### 4.3 Conclusions

Proximate analysis and ultimate analysis and advanced characterization techniques allow a better understanding of reactivity of Tuncbilek lignite. Approximately 28% volatiles, 5% moisture, 38% ash compositions were determined through both classical proximate analysis and TGA experiments.  $\text{SiO}_2$  ( $53.6 \pm 0.4$  wt%),  $\text{Al}_2\text{O}_3$  ( $24.9 \pm 0.2$  wt%) and  $\text{Fe}_2\text{O}_3$  ( $13.0 \pm 0.1$  wt%) were the major components of lignite ash. Sulfur composition was measured by Eschka ( $3.9 \pm 0.2\%$ ) and CHNS analyzer ( $5.4 \pm 0.6\%$ ). The difference between two analyses can be due to the amount of sample used for the analyses. Approximately 1 gram of coal sample is used in Eschka analysis, while 15 mg coal sample is used in CHNS analyzer. The heating value of Tuncbilek lignite was measured by Bomb calorimetry as around 3700 cal/gram. This low value is the specific characteristic of relatively young brown coal. Both XRD and XRF data revealed that the main mineral construction of coal includes quartz, kaolinite, and pyrite. The results of two tests are consistent with each other. DRIFTS results also support these two spectroscopic analyses. The carbon structure and distribution of the functional groups are defined by DRIFTS and  $^1\text{H}$  and  $^{13}\text{C}$  NMR measurements.



## CHAPTER 5

### GASIFICATION AND DESULFURIZATION REACTIVITY OF TUNCBILEK LIGNITE

#### 5.1 Introduction

In the previous chapter, the results of XRD, DRIFTS,  $^1\text{H}$  NMR, and  $^{13}\text{C}$  (CP) MAS-NMR characterization techniques were summarized. In this chapter, these results will be compared with the structural changes occurred during gasification and desulfurization processes.

##### 5.1.1 Gasification reactivity

Gasification is a partial oxidation process, taking place at high temperature. Main aim of this process is to produce synthesis gas, which is a mixture of CO and  $\text{H}_2$ , from coal as well as energy. The gasification reactivity of coal increases with decreasing coal rank. Lignite is a low rank coal. As such, it is an important raw material for gasification technology. Gasification, the most popular clean coal technology, includes pyrolysis and char gasification steps. Pyrolysis is a thermal decomposition process taking place between  $300^\circ\text{C}$ - $500^\circ\text{C}$ . During the pyrolysis step,  $\text{H}_2$  rich volatile and aliphatic carbon fractions are removed from coal. The remaining part is fixed carbon (coal char) and ash. Coal char is more aromatic and more stable (Molina and Mondragon, 1998, Sekine et al., 2006). Molina et al. (1998) stated that the decomposition reactions of the char are dependent on the gaseous species and reaction conditions. As seen in Table 5.1, endothermic dry reforming and steam reforming reactions, and exothermic oxidation, water gas shift and hydrogenation reactions are the possible reactions taking place during char gasification. From the data presented in Table 5.1, it can be seen that exothermic oxidation reaction meets the heat requirement of dry and steam reforming reactions. Moreover, the presence of high amount of steam allows the water gas shift reaction, while carbon hydrogenation reaction occurs at high pressures (Molina and Mondragon, 1998).

Table 5.1. The reactions taking place during coal gasification and their thermochemical data (Molina and Mondragon, 1998, Barin, 1989).

Reactions	$\Delta G_{\text{Rxn}}$ (kJ/mol)	$\Delta H_{\text{Rxn}}$ (kJ/mol)
$\text{C}_{(s)} + \text{CO}_{2(g)} \rightarrow 2\text{CO}_{(g)}$	+ 120.1	+ 172.5
$\text{C}_{(s)} + \text{H}_2\text{O}_{(g)} \rightarrow \text{CO}_{(g)} + \text{H}_2_{(g)}$	+91.4	+ 131.3
$\text{C}_{(s)} + \text{O}_{2(g)} \rightarrow \text{CO}_{2(g)}$	- 394.4	- 393.5
$\text{CO}_{(g)} + \text{H}_2\text{O}_{(g)} \rightarrow \text{CO}_{2(g)} + \text{H}_2_{(g)}$	- 28.6	- 41.2
$\text{C}_{(s)} + 2\text{H}_2_{(g)} \rightarrow \text{CH}_4_{(g)}$	- 50.5	- 74.5

### 5.1.2 Desulfurization reactivity

High amount of sulfur in coal causes serious sulfur emission problems during combustion and requires post purification steps in gasification. Sulfur is present in coal structure in inorganic form as pyritic sulfur ( $\text{FeS}_2$ ) and sulfates and organic form as thiols (Baruah and Khare, 2007). Pyritic sulfur can be removed from coal by physical processes, such as coal washing, flotation, and oil agglomeration (Calkins, 1994) while chemical methods are needed to decrease the organic sulfur content. Leaching, extraction, biodesulfurization and oxidesulfurization processes can be given as examples of chemical methods (Demirbas and Balat, 2004).

Pyrolysis process is an intermediate stage of all coal carbonization, combustion and gasification technologies. This process is also accepted to be an important desulfurization step. During the pyrolysis, the major desulfurization reaction (Equation 5.1) is given below (Xu and Kumagai, 2003):



Hydrogen present in coal can lead to the pyrite reduction at temperatures higher than 600°C. In addition to thermal decomposition of pyrite, adding  $\text{H}_2$  to the environment assists pyrite decomposition as shown in the following reactions (Equations 5.2 and 5.3) (Xu and Kumagai, 2003):



According to Xu and Kumagai (Xu and Kumagai, 2003), pyrite can be converted to ferrous sulfide in the presence of  $\text{H}_2$  at lower temperature (400°C) than is the case in pyrolysis (650°C).

Baruah and Khare (2007) reported maximum sulfur emission in the form of H<sub>2</sub>S between 600°C -850°C under the pyrolysis condition. When temperature was higher than 850°C, the decrease in sulfur evolution was reported. The authors interpreted this outcome to be due to the combination of the coal matrix and sulfur and the transformation to the new sulfur compounds (Baruah and Khare, 2007).

Oxidesulfurization is another important sulfur removal process for pyritic sulfur. Since oxidation takes place in an aqueous media, it is called as wet air oxidation and/or hydrothermal treatment. This process was firstly conducted for the carbonization process in a temperature range of 320°C-400°C. The coal analysis after process revealed that the significant amount of sulfur was removed during process. Furthermore, the presence of alkaline facilitates the carbonization at relatively low temperatures (Mursito et al., 2011, Mishra et al., 1995, Yaman and Kucukbayrak, 1997). Mursito et al. (2011) studied the alkaline hydrothermal treatment of high sulfur and high ash lignite and they reported that alkaline (NaOH) addition increases the ash and sulfur removal. Mishra et al. (1995) summarized the oxidesulfurization and/or wet air oxidation process results in the presence and absence of alkaline in their review article. They reported the favorable temperature and pressure ranges as 150°C-220°C and 1.5-10.23 MPa, respectively. The absence of alkaline leads to the sulfuric acid formation, which makes the organic sulfur removal difficult. Yaman and Kucukbayrak (1997) reported that the increase in sulfate and hematite concentrations after oxidesulfurization process indicates the pyrite and sulfur oxidation. O<sub>2</sub> partial pressure, temperature and residence time are the main parameters affecting the process fate. For example, the high O<sub>2</sub> partial pressure, the temperature higher than 200°C, and the residence time longer than 30 min. cause to decrease in heating value of coal (Yaman and Kucukbayrak, 1997). In summary, pyrolysis, hydrogenation and oxidesulfurization are the common processes for the sulfur removal from fossil fuels. In the subsequent sections, the results of these three processes are discussed in detail.

## **5.2 Results and Discussion**

### **5.2.1 Pyrolysis Experiments**

#### **5.2.1.1 Gaseous products during the pyrolysis process**

CH<sub>4</sub>, H<sub>2</sub>, CO and CO<sub>2</sub> were the main products observed during temperature-programmed experiments under N<sub>2</sub> flow. The results were summarized in Figure 5.1 (a) for CH<sub>4</sub> formation rates and Figure 5.1(b) for H<sub>2</sub> formation rates. In general, total carbon conversion was calculated nearly ~20%. The maximum CH<sub>4</sub> formation was at temperatures between 450-550°C for all samples. As seen in Figure 5.1(b), H<sub>2</sub> formation started at 350°C and reached its maximum value at around 700°C.

The amounts of CH<sub>4</sub> and H<sub>2</sub> during pyrolysis are given in Table 5.2; approximately 1787 μmol/gcoal CH<sub>4</sub> and 3377 μmol/gcoal H<sub>2</sub> were synthesized under the pyrolysis condition. The observed carbon products and carbon conversion values in the gas phase of pyrolysis products are shown in Table 5.3.

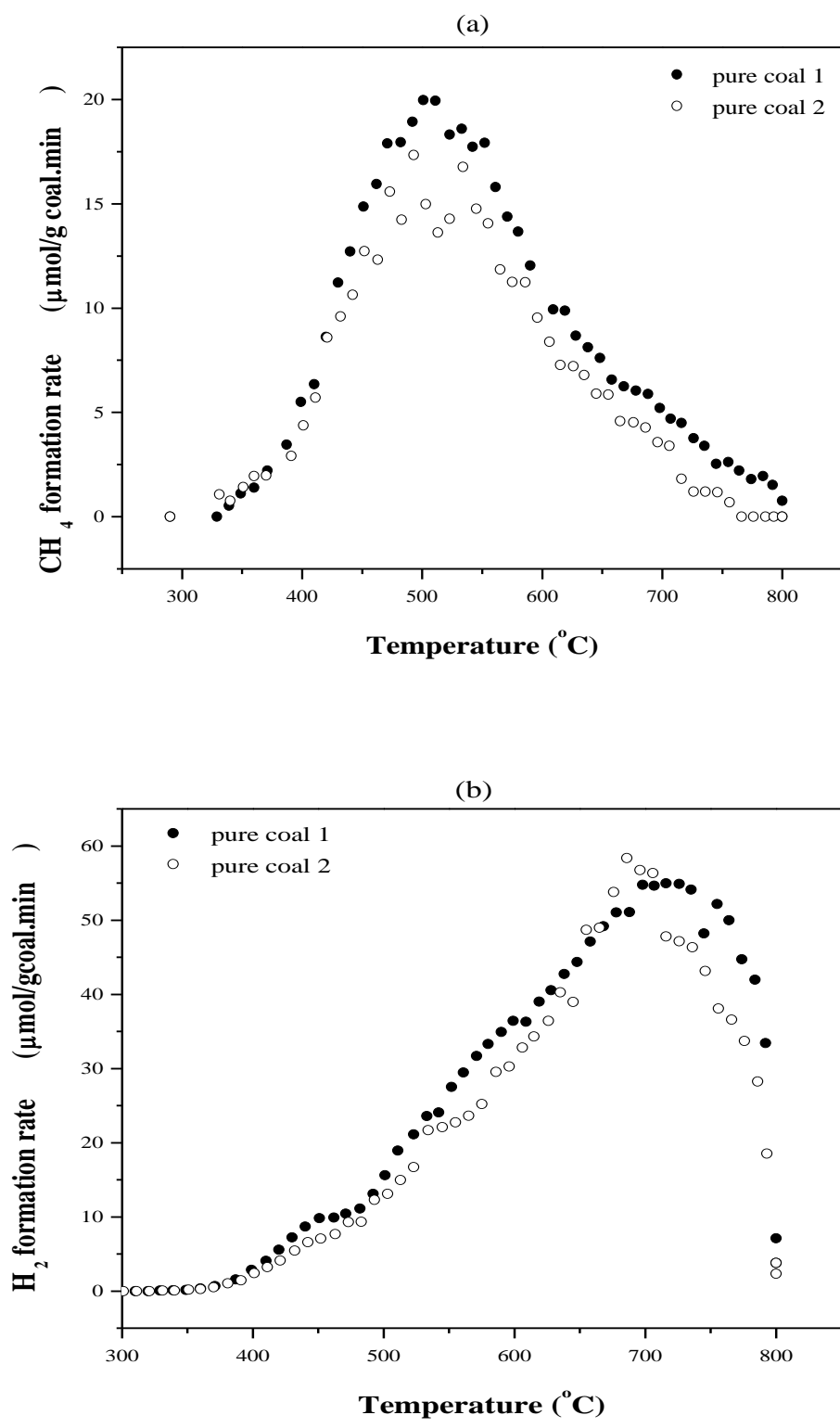


Figure 5.1. CH<sub>4</sub> formation rates (a) and H<sub>2</sub> formation rates (b) under N<sub>2</sub> flow.

Table 5.2. Total amount of CH<sub>4</sub> and H<sub>2</sub> obtained during pyrolysis.

Hydrogen containing pyrolysis product	Amount formed (μmol/gcoal)	% of hydrogen present in the coal leaving with this product
CH <sub>4</sub>	1786.8	19.8
H <sub>2</sub>	3376.7	18.7

Table 5.3. Carbon products and conversion of coal during pyrolysis.

Carbon containing pyrolysis product	Amount formed (μmol/gcoal)	% of carbon present in the coal leaving with this product
CH <sub>4</sub>	1786.8	5.7
CO	1901.5	6.1
CO <sub>2</sub>	2909.9	9.2

### 5.2.1.2 XRD for pyrolysis residue

XRD patterns of pure coal and coal pyrolysis residue were combined in Figure 5.2 in order to explain the variations in coal crystalline structure. The removal of kaolinite peak at 13° and 25° can be interpreted as due to the removal of the hydrates in its crystalline structure. After the pyrolysis process, no significant change is observed for crystalline carbon peaks at 20° and 27°. Sekine et al. (2006) suggested that carbon atoms located near the Si and Al inorganic compounds are not reactive. Since they cover the carbon surface, mass transfer resistance zone forms. The gaseous reactant cannot contact with carbon atoms covered by Si and Al (Sekine et al., 2006).

The characteristic pyrite peaks are at 29°, 33°, 37°, 41°, 47°, 56°, 59°, 61°, and 64°. When we look at the XRD pattern of the pyrolysis residue, the removal or shifting of the strong pyrite peaks can be observed at 33°, 56°, and 37°. This is the thermal decomposition effect on the sulfur removal. Elemental analysis after pyrolysis process reveals that sulfur content of the coal decreases by 25%. When sulfur removal percentage and pyrite peak removal are compared, this decrease was associated with pyrite decomposition.

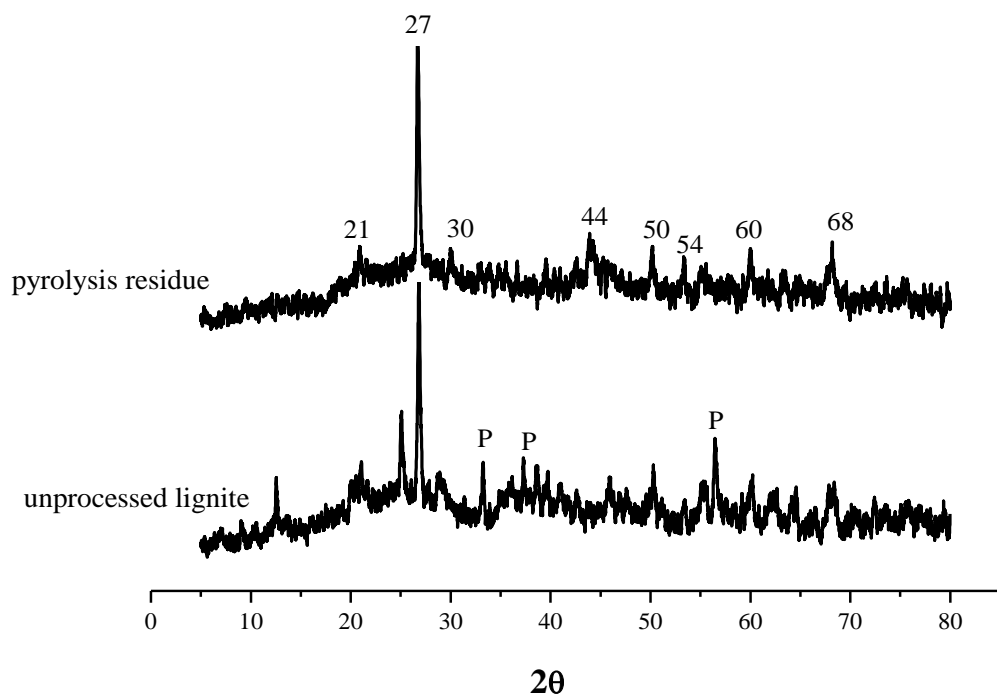


Figure 5.2. XRD pattern of unprocessed lignite and its pyrolysis residue.

### 5.2.1.3 DRIFTS for pyrolysis residue

As mentioned in Chapter 4, the characteristic absorption bands of coal components were summarized as:  $3600\text{--}3100\text{ cm}^{-1}$  region is OH or NH-stretching modes, while the broad band between  $3400\text{--}3000\text{ cm}^{-1}$  is the aromatic C-H stretching vibration region and  $2950\text{--}2850\text{ cm}^{-1}$  is the aliphatic C-H region. As seen in Figure 5.3, these bands defined in the first region disappeared after the pyrolysis process.

Wu (1984) reported that the strong absorption bands between  $1130\text{ cm}^{-1}$  and  $1080\text{ cm}^{-1}$  represent sulfate ions. The presence of absorption band around  $1116\text{ cm}^{-1}$  confirms the presence of sulfate ions after pyrolysis process.

Another important observation for pyrolysis residue is the elimination of absorption bands at  $1438\text{ cm}^{-1}$ ,  $900\text{ cm}^{-1}$ , and  $700\text{ cm}^{-1}$ . These bands are related to carbonates within pyrite (Wu, 1994). During the thermal decomposition process, carbonates are displaced from the structure.

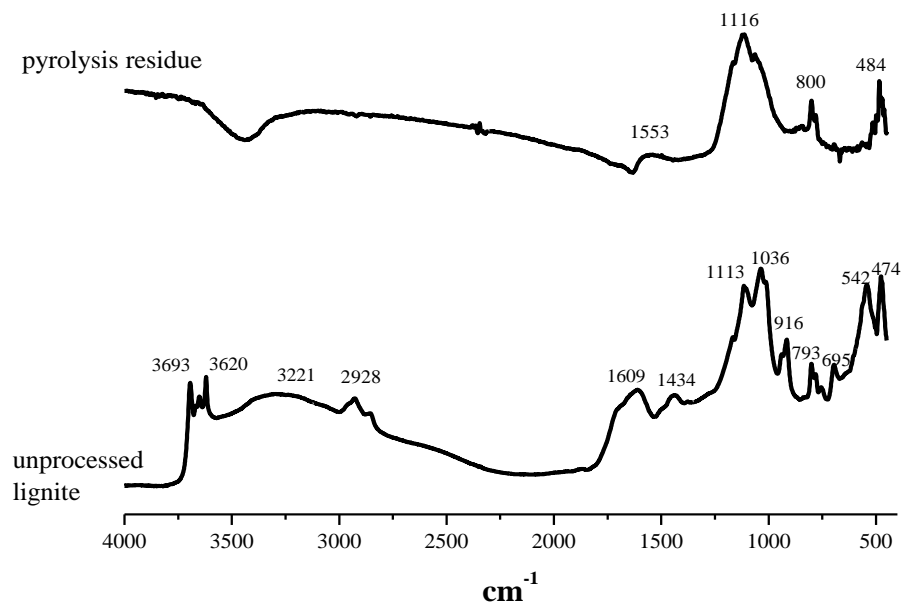


Figure 5.3. DRIFT spectra of coal and its pyrolysis residue.

#### 5.2.1.4 $^1\text{H}$ NMR and $^{13}\text{C}$ (CP) MAS-NMR characterization of pyrolysis residue

$^1\text{H}$  NMR spectrum of the unprocessed lignite in Figure 5.4 has one proton signal corresponds to aliphatic alkyl protons. After the pyrolysis process, two signals (-0.6 and 6.7 ppm) in  $^1\text{H}$  NMR spectrum are observed in Figure 5.4. Bois et al. (1994) characterized the sol-gel derived oxycarbide glasses during the pyrolysis process by proton and carbon NMR spectroscopy. They defined protons attached to silicon as Si-CH<sub>3</sub> group at 0 ppm and Si-OH group at 3 ppm (Bois et al., 1994). Since  $^1\text{H}$  NMR signal of alkyl protons and Si-CH<sub>3</sub> group between 0-20 ppm, the first signal should be correlated from  $^{13}\text{C}$  NMR data. If there is no carbon peak at aliphatic carbon region, then proton signal indicates Si-CH<sub>3</sub> group. The second peak at 6.7 ppm shows the transformation to aromatic structure. This fact can be confirmed by  $^{13}\text{C}$ -NMR spectroscopy. The proton NMR spectrum of pyrolysis residue reveals the formation of Si-CH<sub>3</sub> group around 0 ppm and aromatic protons around 6.5 ppm.

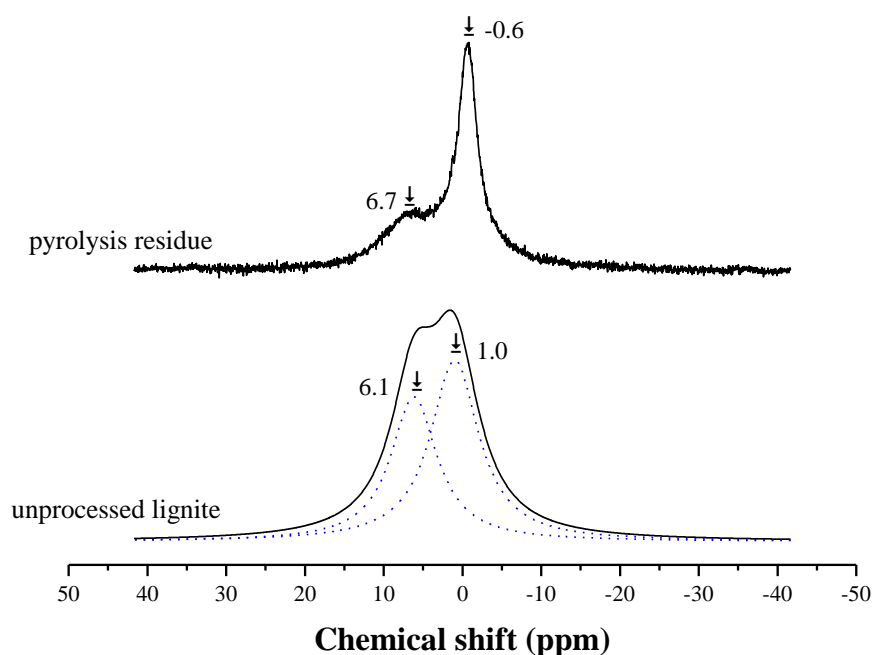


Figure 5.4.  $^1\text{H}$  NMR spectra of unprocessed lignite and its pyrolysis residue.

Analysis of the  $^{13}\text{C}$ -NMR spectrum in Figure 5.5 shows that aliphatic carbon peak at 28 ppm disappeared after pyrolysis. This is an expected result of the thermal decomposition process. During the pyrolysis, the volatile contents of coal were removed and coal aromaticity increased. The removal of aliphatics in coal structure increases the stability of aromatic bridges. Thus, more severe conditions are necessary to affect the remaining part. There is a strong relation between  $^{13}\text{C}$  peaks at aliphatic region and  $^1\text{H}$  peak at -0.9 ppm caused by non-polar alkyl protons (Li et al., 2012). After the pyrolysis process, no variation was recorded in aromatic carbon structure region centered at 125-130 ppm. However, the signal intensity in oxy-bonded alkyls region (148-165 ppm) is increased. The signal observed in pure coal in this area was lost after the pyrolysis process.

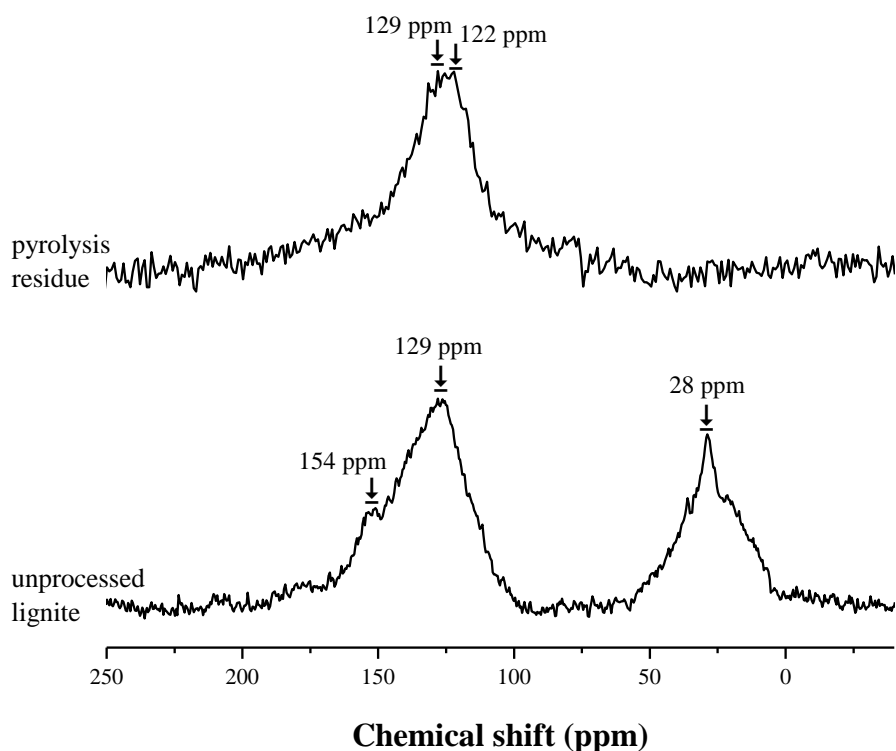


Figure 5.5. Aliphatic, aromatic and C=O double bond traces of unprocessed lignite and lignite residue after pyrolysis.

## 5.2.2 Oxidation Experiments

### 5.2.2.1 Gas Analysis

Similar to pyrolysis, CH<sub>4</sub>, H<sub>2</sub>, CO and CO<sub>2</sub> are the main products of temperature-programmed experiments under airflow. The results of two experiments performed at the same reaction conditions are presented in Figure 5.6 (a) for CH<sub>4</sub> formation rates and Figure 5.6 (b) for H<sub>2</sub> formation rates. In general, total carbon conversion was calculated to be >100%. The evolution of CH<sub>4</sub> and H<sub>2</sub> has started at lower temperatures (~200°C) than observed under N<sub>2</sub> flow.

Integrated amounts of gaseous products (CH<sub>4</sub> and H<sub>2</sub>) throughout the measurements are given in Table 5.4. According to table, approximately 81.6 μmol/gcoal CH<sub>4</sub> and 21.8 μmol H<sub>2</sub>/gcoal were synthesized under ambient atmosphere. The maximum CH<sub>4</sub> and H<sub>2</sub> formation rates under air flow were obtained as one order of magnitude lower than under N<sub>2</sub> flow. The presence of O<sub>2</sub> causes to decrease in CH<sub>4</sub> and H<sub>2</sub> formation rates while leading to the CO<sub>2</sub> and H<sub>2</sub>O formation.

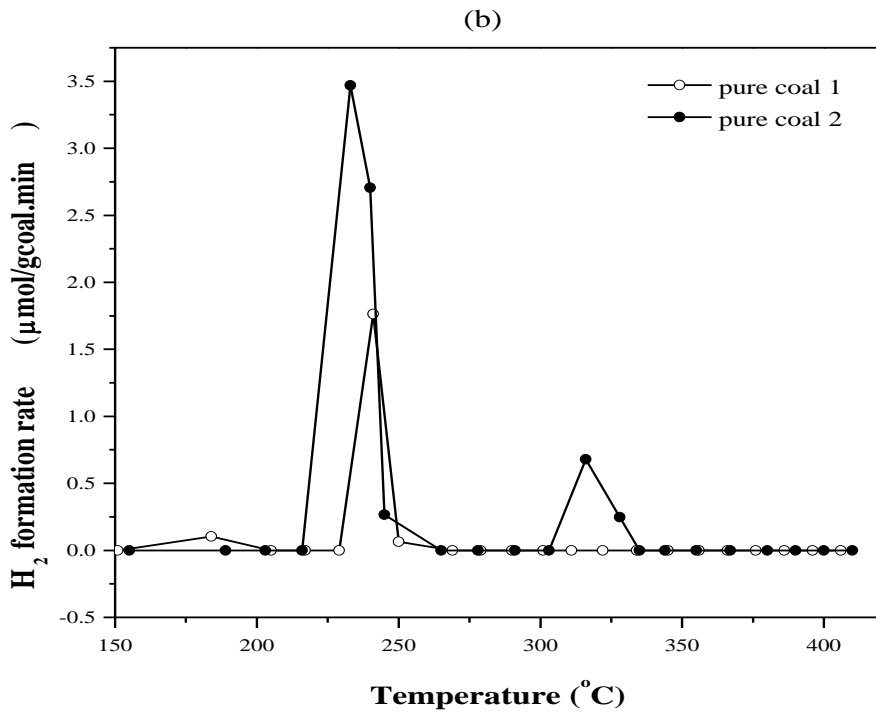
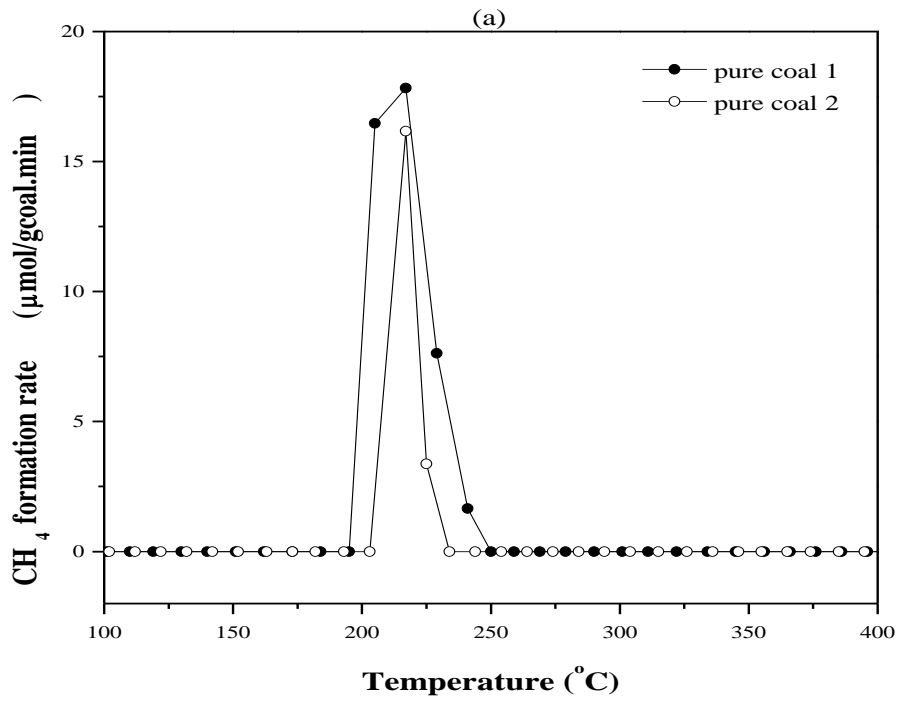


Figure 5.6. CH<sub>4</sub> formation rates (a) and H<sub>2</sub> formation rates (b) under air flow.

Table 5.4. Total amount of CH<sub>4</sub> and H<sub>2</sub> under air flow.

Hydrogen containing pyrolysis product	Amount formed (μmol/gcoal)	% of hydrogen present in the coal leaving with this product
CH <sub>4</sub>	81.6	0.8
H <sub>2</sub>	21.8	0.1

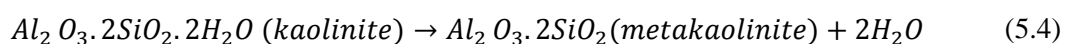
In order to determine the carbon conversion, total amount of CH<sub>4</sub>, CO and CO<sub>2</sub> are divided by the initial amount of carbon (~40%) in coal structure. The results are presented in Table 5.5. >100% carbon conversion was obtained during the oxidation experiments under air flow and in the temperature range of 40-800°C. The excess of 100% is believed to be due to higher carbon fractions present in the particular coal sample than was measured by the elemental analysis.

Table 5.5.Total carbon conversion under air flow.

Carbon containing pyrolysis product	Amount formed (μmol/gcoal)	% of carbon present in the coal leaving with this product
CH <sub>4</sub>	81.6	0.2
CO	3316.4	10.0
CO <sub>2</sub>	37106.9	110.0

### 5.3.2.2 XRD for oxidation residue

XRD patterns of unprocessed coal and its oxidation residue are presented in Figure 5.7. The characteristic kaolinite peaks at 13° and 25° disappeared during oxidation due to the loss of structural hydroxyl groups from kaolinite and transformation to metakaolinite (Lavat, 2011). The related reaction is given in equation 5.4.



The second observation is about the carbon patterns at 20° and 27°. The presence of these peaks indicates that oxidation of Tuncbilek lignite was not completed during the air treatment. As reported by Sekine et al., the presence of Al and Si can prevent the interaction between reactant gas and carbon atoms (Sekine et al., 2006). When we look at the characteristic pyrite peaks, (2θ = 33°, 56°, and 37°) most of the peaks are still present in XRD pattern of coal oxidation residue. Since pyrite oxidation is inevitable during the oxidation process, some of these peaks can be associated with the new products.

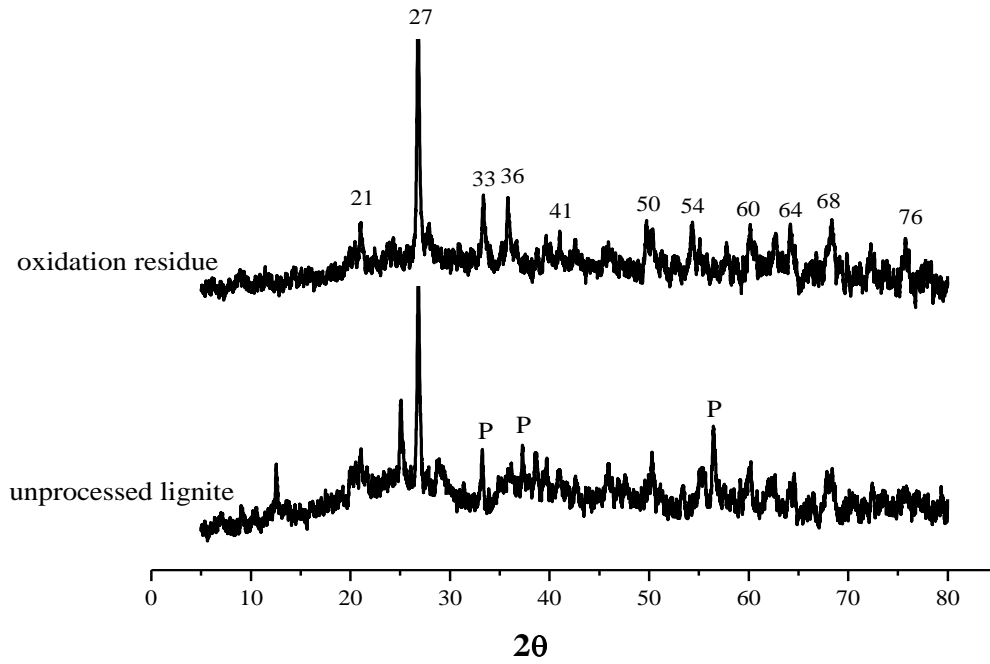


Figure 5.7. XRD patterns of unprocessed lignite and its oxidation residue.

Table 5.6. Possible Bragg angle values of coal inorganics.

Substances	$2\theta$ ( $^{\circ}$ )
Kaolinite $\text{Al}_2\text{Si}_2\text{O}_5(\text{OH})_4$	13, 19, 25, 36, 38
Quartz ( $\text{SiO}_2$ )	27, 21, 50, 37, 39
Pyrite ( $\text{FeS}_2$ )	29, 33, 37, 41, 47, 56, 59, 61, 64
Calcite ( $\text{CaCO}_3$ )	29, 39
Dolomite ( $\text{CaMg}(\text{CO}_3)_2$ )	31, 41

### 5.3.2.3 DRIFTS for oxidation residue

The relatively broad infrared absorption bands of oxidation residue are indicated in Figure 5.8. Two strong absorption bands of OH substituted inorganics ( $3693$  and  $3620$   $\text{cm}^{-1}$ ) disappear, while the broad band of OH substituted aromatics (around  $3200$   $\text{cm}^{-1}$ ) is still noticeable after oxidation. The broad absorption bands located at  $3200$   $\text{cm}^{-1}$  and  $1640$   $\text{cm}^{-1}$  are attributed to moisture adsorbed by the remaining part. Absorption bands at  $542$ ,  $695$ ,  $916$ , and  $1434$   $\text{cm}^{-1}$  are also removed after oxidation, while  $1641$  and  $1876$   $\text{cm}^{-1}$  are the new bands formed during the oxidation. Lavat et al. (2011) recorded that calcite and dolomite have a similar structure. Their infrared bands are located at the same wave numbers of  $1428$   $\text{cm}^{-1}$ ,  $878$   $\text{cm}^{-1}$ , and  $714$   $\text{cm}^{-1}$  (Lavat, 2011, Gunasekaran and Anbalagan, 2007). Additionally, pyrite absorption bands were defined by Wang et al. (2010) and Wu et al. (1994) at  $1438$ ,  $872$ ,  $707$   $\text{cm}^{-1}$  associated with  $\text{CO}_3^-$  within pyrites (Wang et al., 2010a, Wu, 1994). The removal of these bands after oxidation is due to  $-\text{CO}_3^-$  and it shows clearly the structural change of calcite and dolomite and also pyrite. A new band appeared at about  $1850$   $\text{cm}^{-1}$  after oxidation, which was attributed to non-protonated anhydrides (Iglesias et al., 1998). An examination of the DRIFTS spectra in the range of  $2000$ - $1300$   $\text{cm}^{-1}$  revealed two relatively broad aromatic C-O stretching bands near  $1600$ - $1400$   $\text{cm}^{-1}$  for the pure lignite sample and its oxidation residue (Cetinkaya and Yurum, 2000).

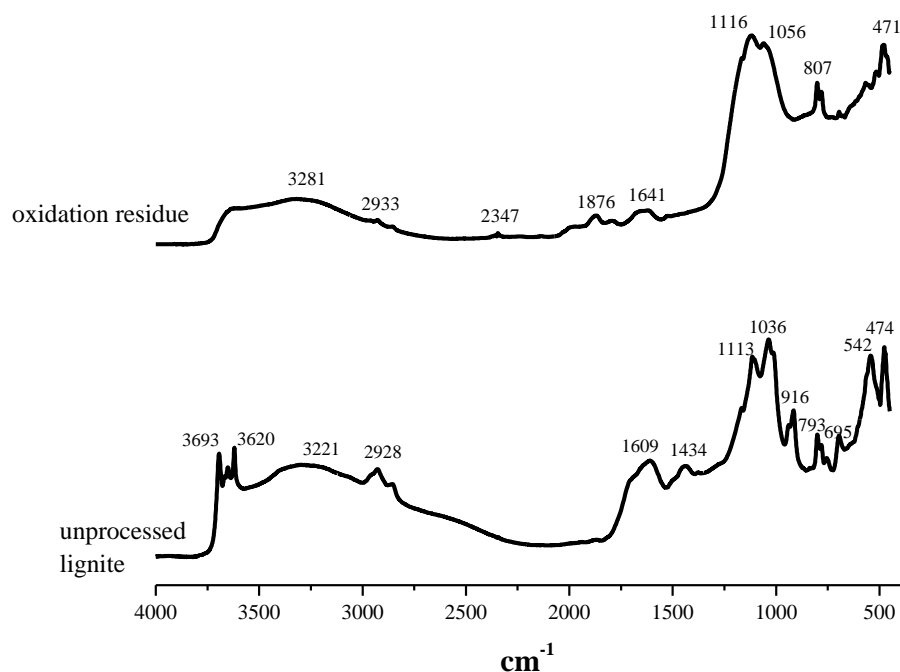


Figure 5.8. DRIFTS spectra of unprocessed lignite and its oxidation residue.

#### 5.3.2.4 $^1\text{H}$ and $^{13}\text{C}$ (CP) MAS-NMR characterization of oxidation residue

As seen in Figure 5.9, no proton signal was detected beyond the background from  $^1\text{H}$  NMR of the oxidation residues. As a result,  $^{13}\text{C}$  (CP) MAS NMR measurement was not performed.

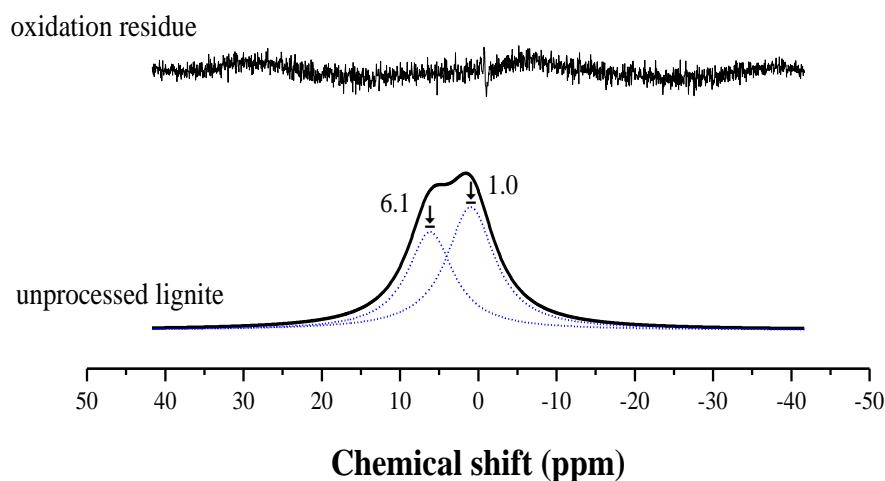


Figure 5.9.  $^1\text{H}$  NMR spectra of unprocessed lignite and its oxidation residue.

### 5.3.3 Hydrogenation Experiments

#### 5.3.3.1 Elemental Analysis

The results of the elemental analysis before and after the pyrolysis and hydrogenation processes indicated that the sulfur contents of lignite samples significantly reduced after hydrogenation. This reduction is directly related to the amount of hydrogen. The change of sulfur composition in coal structure depending on the hydrogen partial pressure during hydrogenation is listed in Table 5.7.

Table 5.7. Sulfur removal percentages determined by elemental analysis results.

H <sub>2</sub> concentration (%)	∑ sulfur removal (%)
0 (from pyrolysis experiment)	25
20	46
40	50
60	51
80	53
100	92

This change is also indicated in Figure 5.10. About 25% sulfur removal was recorded under inert atmosphere. Thermal decomposition process allows the hydrogen sulfide formation using the inherent hydrogen of Tuncbilek lignite. The addition of hydrogen accelerates the sulfur reduction. For example, sulfur concentration decreases to half of its initial concentration under 20% H<sub>2</sub> flow. However, decrease of sulfur concentration is not substantial when the H<sub>2</sub> concentration of the feed flow is between 40% and 80%. In contrast, approximately 92% sulfur removal was recorded under pure hydrogen flow.

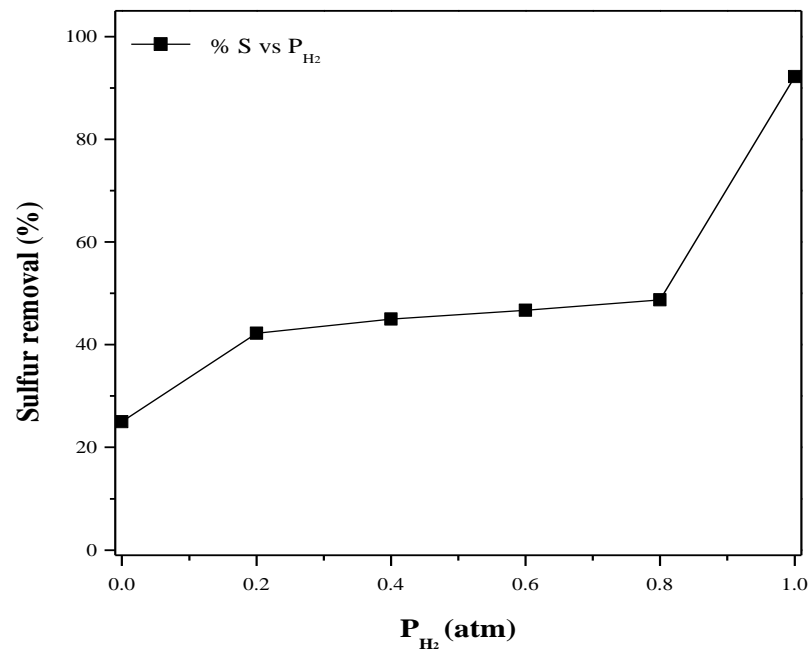


Figure 5.10. Sulfur removal percentages of Tuncbilek lignite vs. hydrogen partial pressure.

### 5.3.3.2 XRD for hydrogenation residue

XRD patterns of unprocessed Tuncbilek lignite and its carbon rich residue at the end of the hydrogenation treatment were combined in Figure 5.11. During the hydrogenation process performed under 50 cc/min pure hydrogen flow, the characteristic kaolinite peaks at 13° and 25° disappeared as well as pyrolysis and oxidation reactions. Since the common property of three processes is heating in the same temperature range, the disappearance is probably due to the thermal decomposition. In addition, the three strong and sharp pyrite XRD patterns at 33°, 56°, and 37° are not seen after the hydrogenation process. Since elemental analysis results confirm the sulfur removal, the new peak formation at 45° cannot be due to the pyrite.

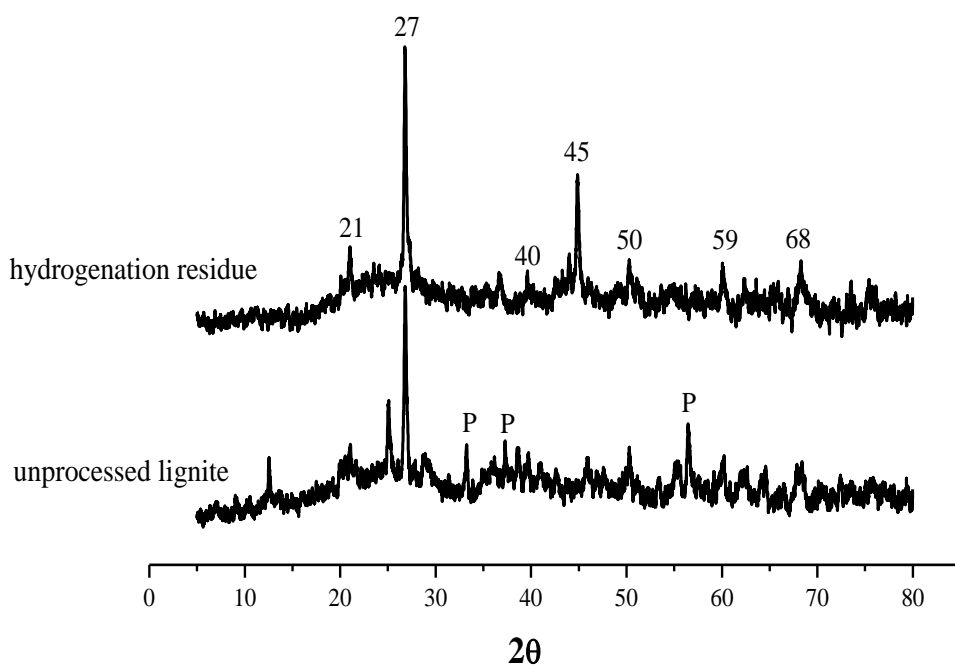


Figure 5.11. X-ray patterns of unprocessed lignite and its hydrogenation residue.

Sulfur capture ability of PbO and ZnO, located out of reactor is monitored after hydrogenation process. The characteristic XRD patterns of adsorbents including Pb, Zn, oxygen, and S are presented in Figure 5.12 for Pb and 5.13 for Zn. Furthermore, XRD databank and related articles define the most possible compounds after hydrogenation. Table 5.8 indicates the strong three-peak positions of components namely, PbO, PbS, PbSO<sub>4</sub>, and PbOSO<sub>4</sub>, ZnO, ZnS, ZnSO<sub>4</sub>, ZnS<sub>2</sub>O<sub>4</sub>.

The possible PbS peaks in literature are described at 26°, 29°, 43°, 51°, 54°, 63°, 69°, 71°, 79° (Zhang et al., 2007, Balaz et al., 2011, Pawar et al., 2011) while characteristic PbSO<sub>4</sub>

peaks are identified at 21°, 23°, 26°, 29°, 37°, 43°, and 44° (Fang et al., 2010, Zhang et al., 1994, Xiang et al., 2005). The formation of the new peaks and shifted peaks can indicate the sulfidation products Pb such as, PbS and/or PbSO<sub>4</sub>.

Table 5.8. Bragg angle values of some components.

Components	2θ (°)	2θ (°)	2θ (°)
PbO	28.6	32.8	57.0
PbS	30.1	26.0	43.1
PbSO <sub>4</sub>	43.7	29.7	26.7
PbOSO <sub>4</sub>	26.7	30.3	30.3
ZnO	33.7	58.8	62.7
ZnS	28.5	47.4	56.3
ZnSO <sub>4</sub>	21.4	35.3	41.7
ZnS <sub>2</sub> O <sub>4</sub>	25.1	21.3	33.8

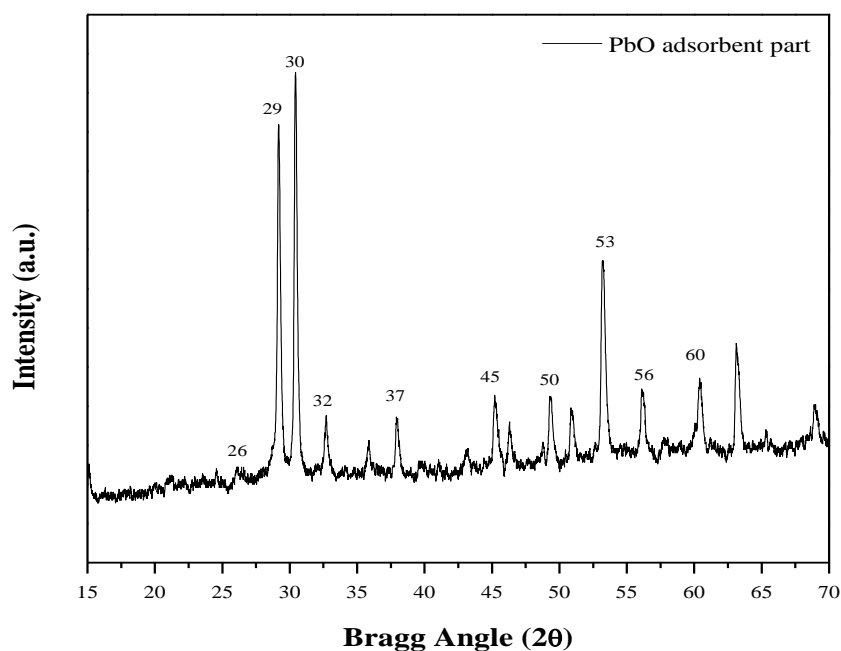


Figure 5.12. XRD pattern of commercial PbO after hydrogenation experiment

The specific Bragg angle values of ZnS were described in literature as 28.5°, 47.5°, and 56.3° (Li and Tang, 2007, Balaz et al., 1997, Nanda et al., 2000, Ashwini et al., 2012). In addition to characteristic ZnO peaks around 34°, 59°, 63°, these new peaks seen in

Figure 5.13 verify the sulfur capture ability of ZnO at ambient condition under 50 cc/min H<sub>2</sub> flow.

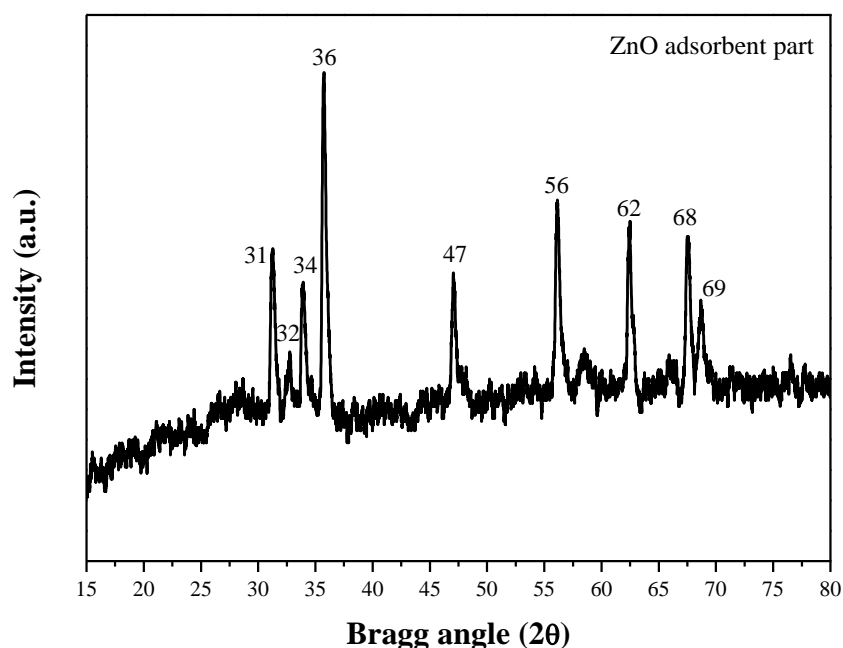


Figure 5.13. XRD pattern of commercial ZnO after hydrogenation experiment.

### 5.3.3.3 DRIFTS for hydrogenation residue

A DRIFT spectrum of coal sample is presented in Figure 5.14. The first region defined between 3800-3100 cm<sup>-1</sup>, includes OH-substituted inorganics and CH stretching vibration of aromatic structure. This region was removed during the hydrogenation processes. Similarly, the aliphatic C-H region observed at 2950- 2850 cm<sup>-1</sup> was also lost after hydrogenation. The disappearance of absorption bands at 1434, 916, and 695 cm<sup>-1</sup> indicates the CO<sub>3</sub><sup>=</sup> loss during the hydrogenation process. The absorption bands at 542 and 1036 cm<sup>-1</sup> were also dissipated. A new peak formation at 1560 cm<sup>-1</sup> may be due to the carboxylate anion and N-H groups. The absorption peaks at 872 and 707 cm<sup>-1</sup> associated with CO<sub>3</sub><sup>=</sup> indicate the presence of carbonates within pyrite (Wu, 1994). Wu (1994) also reported that sulfate has a very strong absorption band in the spectral region between 1130 and 1080 cm<sup>-1</sup> in the infrared Fourier transform spectroscopy spectra. In another study, Wang et. al. (2010) explained that the strong absorption peak near 1152 cm<sup>-1</sup> associated with the stretching vibration of SO<sub>4</sub><sup>=</sup> indicates that the oxidizing reaction of pyrite is accompanied by sulfate formation (Wang et al., 2010a, Wu, 1994).

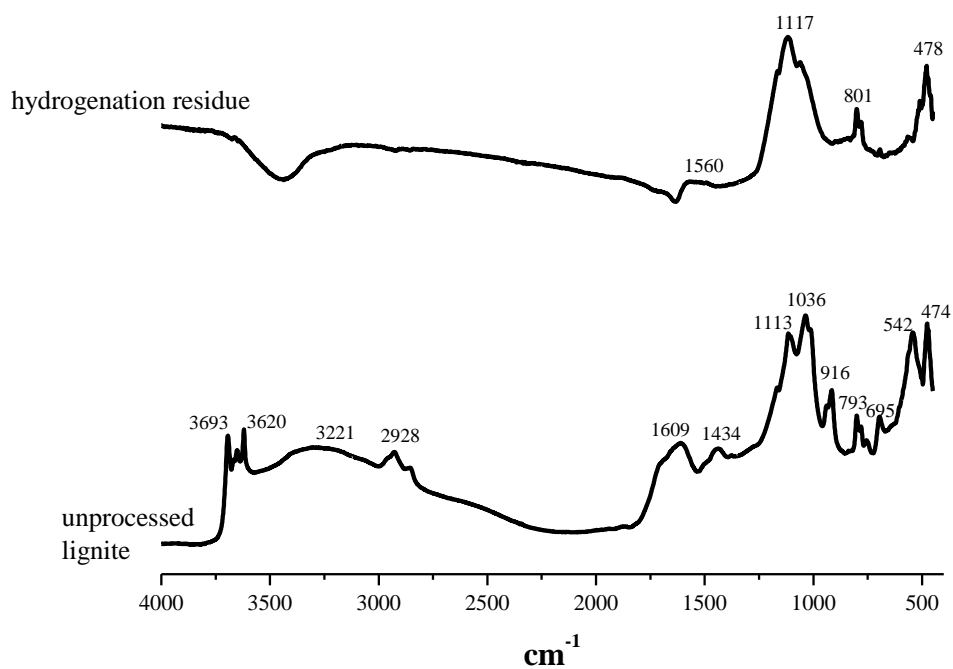


Figure 5.14. DRIFT spectra of unprocessed lignite and its hydrogenation residue.

#### 5.3.3.4 $^1\text{H}$ and $^{13}\text{C}$ (CP) MAS-NMR characterization of hydrogenation residue

It was not possible to obtain a proton signal beyond the background from  $^1\text{H}$  MAS NMR of the hydrogenation residue, as well as in the residues of pyrolysis and oxidation (Figure 5.15). Therefore,  $^{13}\text{C}$  (CP) MAS NMR experiment was not conducted for oxidation residue. This result reveals the absence of protonated structure after hydrogenation.

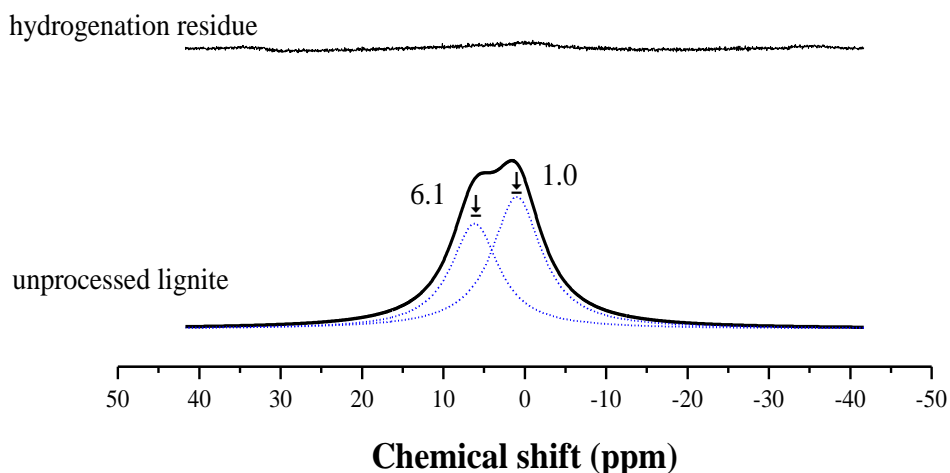


Figure 5.15.  $^1\text{H}$  NMR spectra of the unprocessed lignite and hydrogenated solid coal residue.

On the other hand, fatty and viscous liquid material known as tar was collected at the end of the quartz reactor during the hydrogenation process and it is defined as by-product of hydrogenation. This part of the quartz reactor was separated and crushed for NMR measurements. In Figure 5.16, the proton NMR spectra of the unprocessed coal sample and coal tar are compared. Two different types of proton in tar structure originate from aliphatic methylene protons at 0.5 ppm and aromatic proton at 6.2 ppm. In addition, four different types of carbon peaks are presented in Figure 5.17. Carbon signals on the solid-state  $^{13}\text{C}$  NMR spectrum of tar are assigned by aromatic carbon structure. Regarding to aromatic region, both protonated (123 ppm) and non-protonated (132 ppm) aromatic carbons are present in the tar structure. The other shoulders on the  $^{13}\text{C}$  NMR are caused by oxy-substituted (phenolic) at 154 ppm and carboxylic and amide carbons at 165 ppm (Peuravuori et al., 2006).

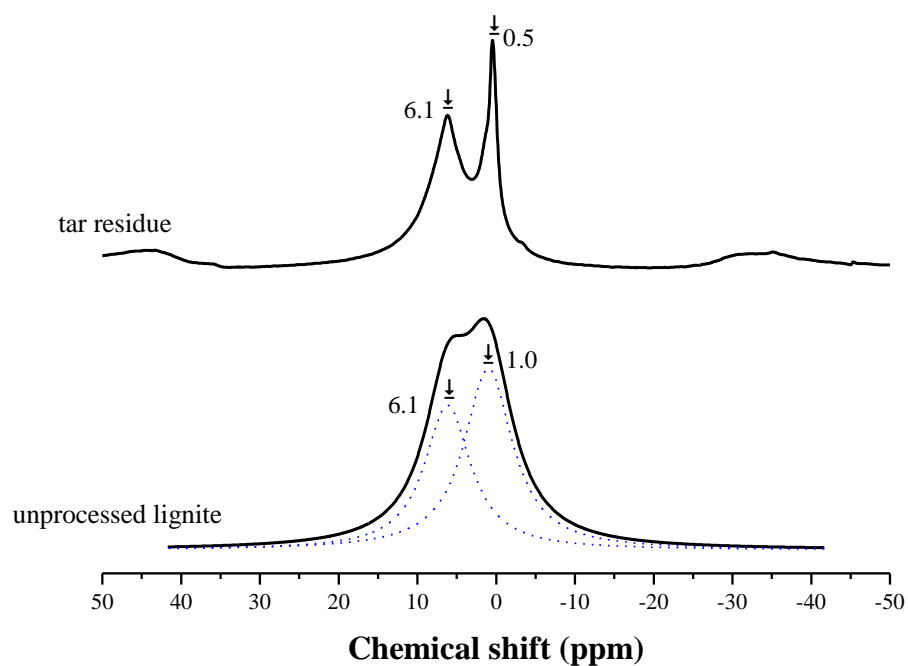


Figure 5.16.  $^1\text{H}$  NMR spectra of the unprocessed lignite and hydrogenated liquid coal residue.

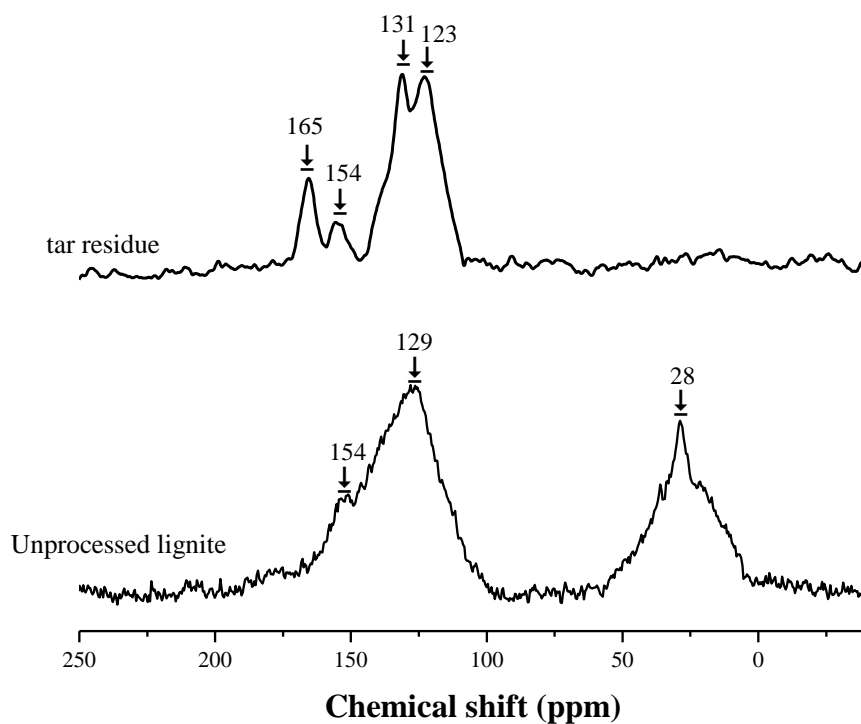


Figure 5.17.  $^{13}\text{C}$  NMR spectra of the unprocessed lignite and hydrogenated liquid coal residue.

### 5.3.3.6 Comparison of the residue of pyrolysis, oxidation, and hydrogenation processes

XRD, DRIFTS, and  $^1\text{H}$  and  $^{13}\text{C}$  (CP) MAS NMR characterization techniques were employed in order to compare the structural changes occurred during gasification and desulfurization processes. In order to evaluate the processes, XRD, DRIFTS, and  $^1\text{H}$  and  $^{13}\text{C}$  (CP) MAS-NMR results of the solid residues are combined in this section of the study.

Figure 5.18 demonstrates the X-ray diffraction patterns of pyrolysis, oxidation, and hydrogenation residues of Tuncbilek lignite together with unprocessed lignite sample. The important common properties of these processes can be summarized as:

Removal of kaolinite at  $13^\circ$ - $25^\circ$ , non-reactive carbons components at  $20^\circ$  and  $27^\circ$ , and the loss of the characteristic pyrite peaks after pyrolysis and hydrogenation.

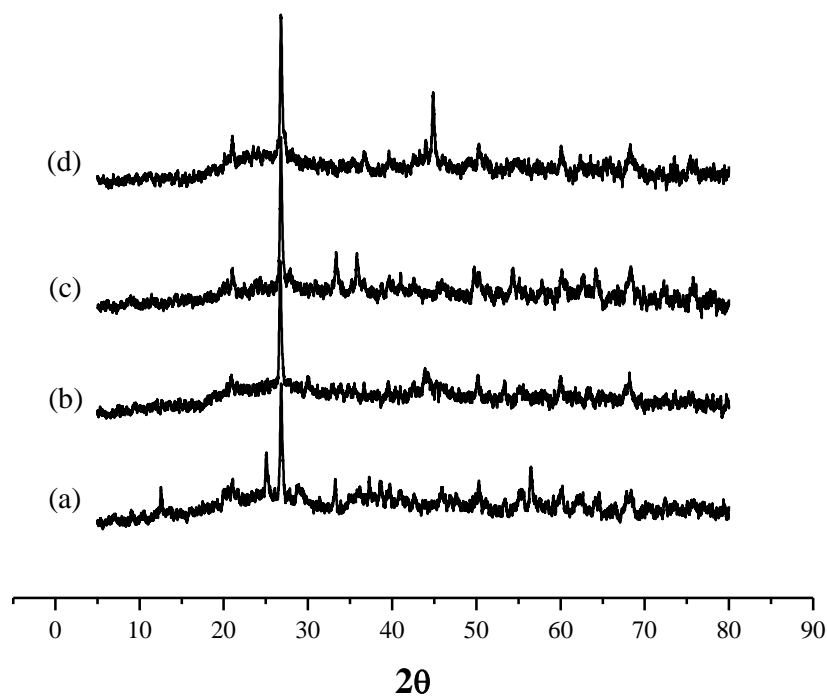


Figure 5.18. XRD patterns of (a) unprocessed lignite, (b) coal sample residue after pyrolysis, (c) coal sample residue after oxidation, (d) coal sample residue after hydrogenation Tuncbilek lignite.

DRIFTS,  $^1\text{H}$  MAS NMR, and  $^{13}\text{C}$  (CP) MAS-NMR characterization techniques were employed in order to compare the structural changes occurred during pyrolysis, air oxidation and hydrogenation processes. As seen in Figure 5.19, the absorption band at

2850-3000  $\text{cm}^{-1}$  originated from aliphatic C-H stretching (Figure 5.19a) was removed during the pyrolysis, oxidation and hydrogenation processes (Figure 5.19b, c, and d). The removal of the bands at 1434, 916, and 695  $\text{cm}^{-1}$  is due to the  $\text{CO}_3^{2-}$  substituted inorganic minerals of calcite, dolomite and pyrite.

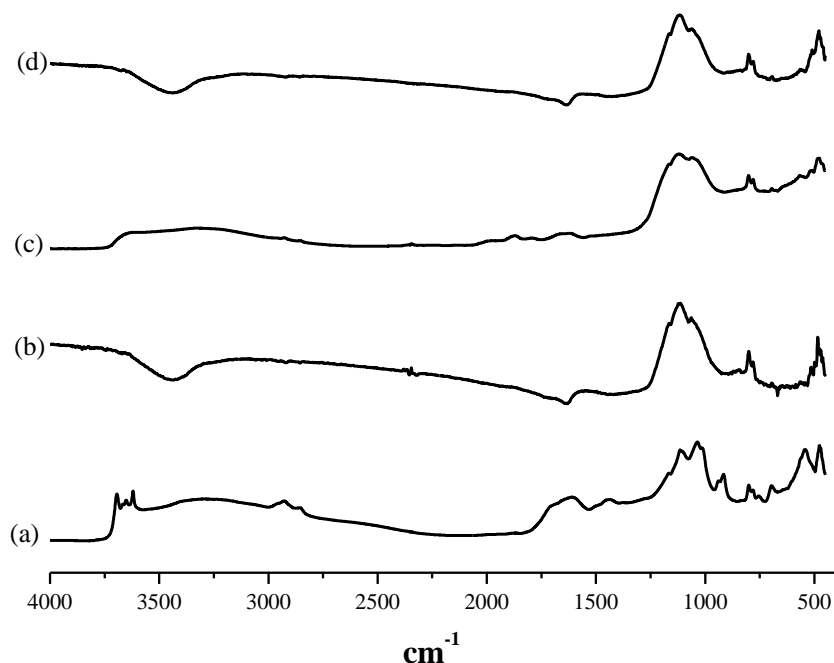


Figure 5.19. DRIFT spectra of (a) coal samples, (b) coal sample residue after pyrolysis, (c) coal sample residue after oxidation, (d) coal sample residue after hydrogenation Tuncbilek lignite.

Additionally, the absorption bands of -OH substituted inorganics and aromatics in the region 3700-3000  $\text{cm}^{-1}$  disappeared after pyrolysis and hydrogenation. The broad band still seen in Figure 5.19c indicates the steam formation during air oxidation.

Coal reactivity as monitored by NMR spectroscopy, can be summarized that all aliphatic structures were removed from coal sample by heating up to 800°C for 2.5 hours under inert atmosphere. After the pyrolysis process, there are two peaks (-0.7 and 6.5 ppm) in  $^1\text{H}$  NMR spectrum shown in Figure 5.20. These signals indicated the presence of alkyl protons at -0.6 ppm and aromatic protons at 6.7 ppm. On the other hand, no proton signal was detected beyond the background from  $^1\text{H}$  NMR of the oxidation and hydrogenation residues. This was also another indication of the disappearance of C-H bonds in the oxidation and hydrogenation residues as deduced from the DRIFTS spectra of the same samples.

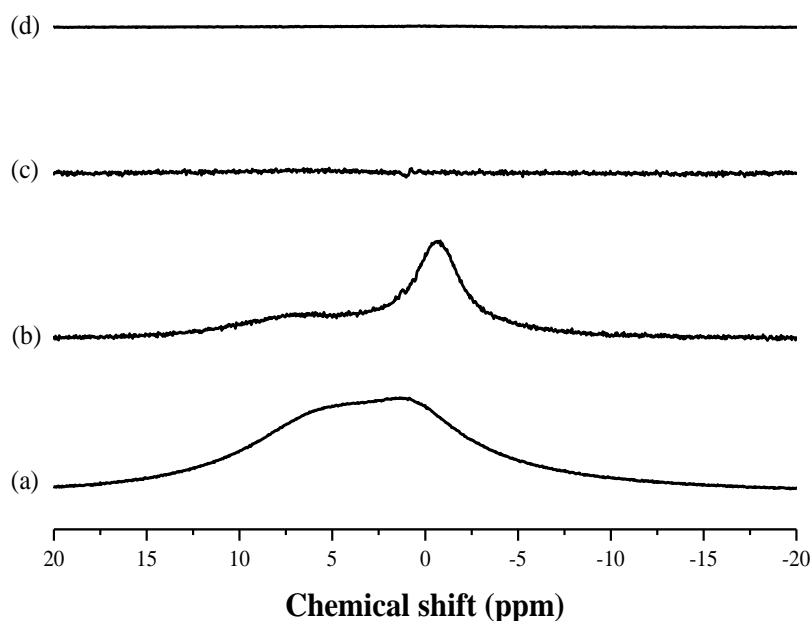


Figure 5.20.  $^1\text{H}$  MAS NMR spectra of (a) coal samples, (b) coal sample residue after pyrolysis, (c) coal sample residue after oxidation, (d) coal sample residue after hydrogenation Tuncbilek lignite.

In addition, coal structure after hydrogenation is quite similar to unprocessed coal but the relative amounts of coal components varied under the hydrogenation condition. The by-product of hydrogenation, tar represents the liquefaction product of coal formed by mostly aromatics.

The main change in aromatic carbon structure was recorded in the range of 100-200 ppm by  $^{13}\text{C}$ -NMR during pyrolysis (Figure 5.5). The sharp peak at 125 ppm -130 ppm was still present in pyrolysis residue, while the shoulder near 154 ppm was lost after the pyrolysis. As seen in Figures 5.20c and d, since proton signals were not obtained for oxidation and hydrogenation residues, it can be said that there is no protonated aromatic carbon in the oxidation and hydrogenation residues. The presence of non-protonated aromatic fraction was controlled by DRIFT spectra of coal and its residues (Figure 5.19). Especially, a new band appeared at about  $1850\text{ cm}^{-1}$  after oxidation, which was attributed to non-protonated anhydrides (Iglesias et al., 1998). An examination of the DRIFTS spectra in the range of  $2000\text{-}1300\text{ cm}^{-1}$  revealed two relatively broad aromatic C-O stretching bands near  $1600\text{-}1400\text{ cm}^{-1}$  for the pure lignite sample and its oxidation residue (Cetinkaya and Yurum, 2000).

### 5.3.4 Hydrothermal Desulfurization (Wet Air Oxidation) Experiments

#### 5.3.4.1 Elemental Analysis

Hydrothermal desulfurization or wet air oxidation experiments were conducted at three reaction parameters. Time is the first parameter to be tested and during the process, final temperature and pressure were maintained constant at 150°C and five bars, respectively. The remaining part after the experiments was filtrated and dried at 105°C. Total amount of sulfur in solid residue was determined by the Eschka analysis and a CHNS analyzer.  $\text{SO}_4^-$  analysis was performed for both solid and liquid residues, while pyritic sulfur was determined for solid residue. Moreover, heating values of solid residue were measured by bomb calorimeter. All these techniques were described in Chapter 3.

The results of the first experimental arrangement are presented in Table 5.9. In Table 5.9a, total sulfur contents of wet air oxidation residues, determined by two different ways, were tabulated together with their heating values. As mentioned in Chapter 4, total sulfur contents of Tuncbilek lignite was determined by ultimate analysis and Eschka method as  $5.4 \pm 0.6$  and  $3.9 \pm 0.6$ , respectively. Additionally, its calorific value is  $3680 \pm 60 \text{ cal/g}$ .

All these data tabulated in Table 5.9a show that, total sulfur amount of solid products after wet air oxidation experiments decreases by a small amount (~30% with respect to elemental analysis result of 15 min sample). However, this change is not dependent on duration. Therefore, 15 minutes was selected as duration for the other steps of the wet air oxidation experiments.

Types of sulfur present in both liquid and solid samples are also tabulated, as well as possible in Table 5.9b. Pyritic and sulfate compositions for some samples are not presented in this table, due to the problems that occur during the analysis. This table demonstrates that sulfur composition of liquid and solid products does not change with duration. The presence of  $\text{SO}_4^-$  anion in liquid residue confirms that the wet air oxidation reactions take place at 150°C and 5 bar.

Table 5.9a. Total sulfur composition and heating value of wet air oxidation products.

Duration at 5bar and 150°C	Heating value (cal/g)	Total S in solid residue by Ultimate analysis method (%)	Total S in solid residue by Eschka method (%)
0 min	3977	3.88	3.92
15 min	5249	3.87	3.67
30 min	4018	4.37	3.43
1 hr	3998	4.12	3.18
3 hr	3963	4.18	3.00
5 hr	3985	3.92	2.66
7 hr	4015	3.96	3.71

Table 5.9b. Pyritic sulfur composition of solid residue and  $-\text{SO}_4^-$  composition of solid and liquid residues.<sup>1</sup>

Duration at 5bar and 150°C	$\text{SO}_4$ in liquid solution (%)	$\text{SO}_4$ in solid residue (%) x	Pyritic Sulfur (%) x
0 min	0.48		
15 min	0.43	0.18	2.60
30 min	0.52	0.17	2.28
1 hr	0.57	0.17	2.64
3 hr	0.44	0.20	1.12
5 hr	0.62		
7 hr	0.54		

In addition, no structural change in inorganic coal structure was recorded by XRD. Figure 5.21 indicate the characteristic XRD pattern of coal inorganic structure.

<sup>1</sup>. The cells in x columns are left empty because the amount of the final residue is insufficient for measurement.

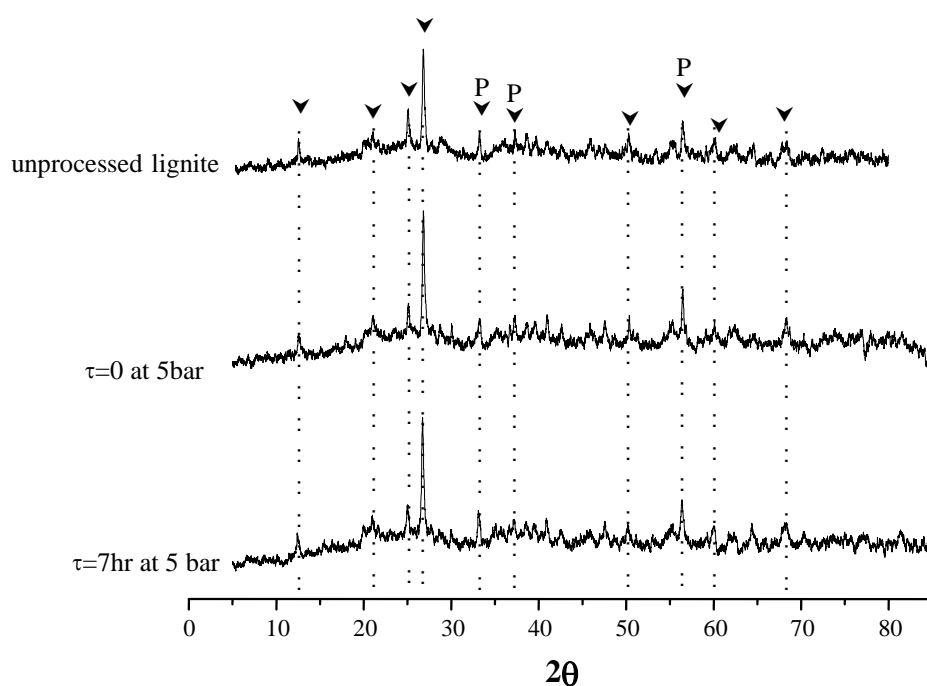


Figure 5.21. Inorganic structure of lignite residue after wet air oxidation for the longest and shortest duration.

After the evaluation of the time parameter, second reaction parameter, initial pressure effect was examined at 150°C and 15 min duration. The characterization results are shown in Table 5.9a and b. During the experiments, four initial pressure values of 2 atm, 3 atm, 6 atm, and 7 atm were tested in the presence of 50 ml water. As seen in Table 5.10a, sulfur removal is not high in the presence of high-pressure air and higher amount of water.

Table 5.10a. O<sub>2</sub> partial pressure effects at 150°C and in the presence of 50 cc water.

Initial pressure (bar)	Heating value (cal/g)	Total S in solid residue by Ultimate analysis method (%)	Total S in solid residue by Eschka method (%)
2	4003	4.26	3.06
3	4143	4.28	2.59
6	4049	4.19	2.65
7	4000	4.17	3.22

In this step, maximum sulfur percentage removed at 7 atm pressure is about 22%. As a result, no important improvement was obtained when air pressure is between 2 and 7

atm. Moreover, relative amount of  $\text{SO}_4^{=}$  in solid and liquid residues, seen in Table 5.10b, is lower at high-pressure condition than at atmospheric condition.

Table 5.10b.  $\text{O}_2$  partial pressure effect on pyritic sulfur and sulfate composition.

Initial pressure (bar)	$\text{SO}_4^{=}$ in liquid solution (%)	$\text{SO}_4^{=}$ in solid residue (%)	Pyritic Sulfur (%)
2	0.50	0.14	1.99
3	0.21	0.16	1.61
6	0.38	0.15	1.97
7	0.39	0.15	2.02

Inorganic structure stability of lignite residues after hydrothermal treatment at 1 bar and 7 bar air is indicated in Figure 5.22.

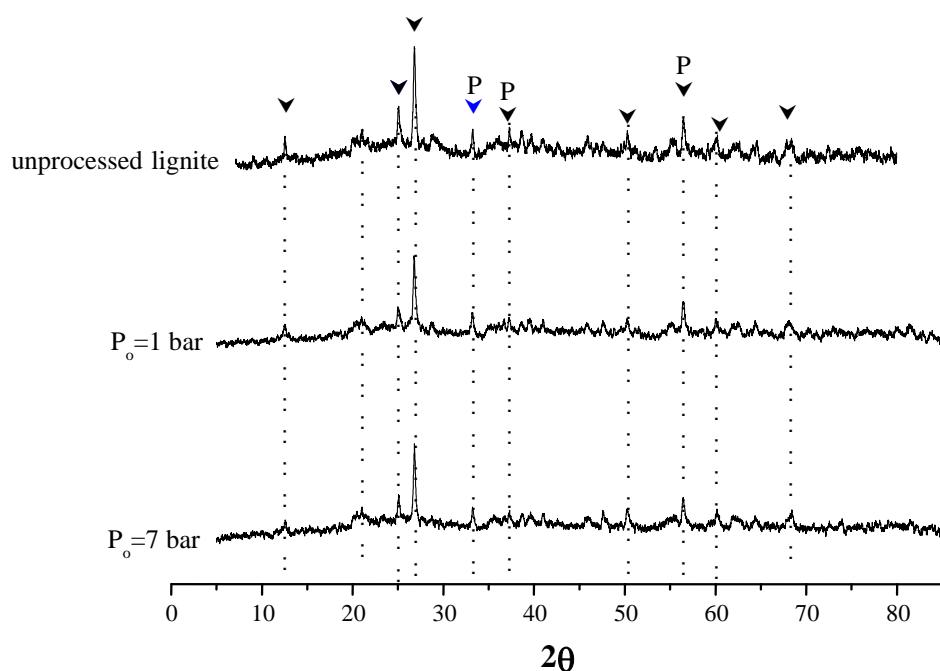


Figure 5.22. Inorganic structure of lignite residue after wet air oxidation at 1 bar and 7 bar.

The last step is the temperature effect measurements. These experiments were conducted at 5 bar initial pressure and 50 cc water. The sample was kept at the desired temperature for 15 minutes for each trial. After the final temperature was reached, it was kept there for 15 minutes for each measurement. The results of the experiments are presented in Table 5.10 a and b. According to information presented in Table 5.11a, heating values of the residues do not change with changing temperature. Relative amount of sulfur in

solid residue is lower than unprocessed lignite but this decrease is insufficient as expected.

Table 5.11a. Temperature effect at 5 bar and in the presence of 50 cc water.

T (°C)	Heating value (cal/g)	Total S in solid residue by Ultimate analysis method (%)	Total S in solid residue by Eschka method (%)
160	3919	4.41	2.81
166	3802	4.30	3.02
170	3979	4.33	3.13
180	4120	4.32	2.52

The sulfate and pyritic sulfur contents of coal residues in Table 5.11b give the similar results. Total sulfate percentage of lignite sample decreases in general. There is a small decrease in pyritic sulfur composition. Furthermore, sulfate composition of liquid residues is approximately 0.43%.

The structural comparison among the unprocessed and processed lignite sample indicates the stability of structure with increasing temperature. XRD patterns of unprocessed and processed samples in Figure 5.23 just indicate the small changes in intensity of characteristic pyrite peaks. On the other hand, peak positions remain the same with decreasing operation temperature.

Table 5.11b. Temperature effect at 5 bar and in the presence of 50 cc water.<sup>2</sup>

T (°C)	SO <sub>4</sub> <sup>=</sup> in liquid solution (%)	SO <sub>4</sub> <sup>=</sup> in solid residue (%)	Pyritic Sulfur (%) x
160	0.44	0.16	2.04
166	0.42	0.15	1.82
170	0.39	0.13	
180	0.46	0.17	1.21

<sup>2</sup> The cell in x column is left empty because the amount of the final residue is insufficient for measurement.

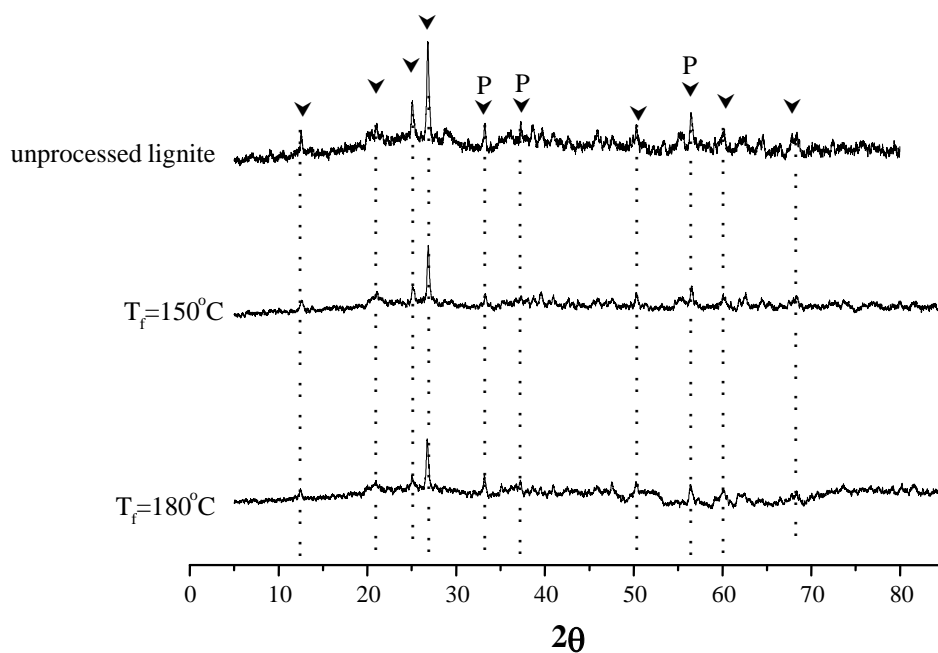


Figure 5.23. Inorganic structure of lignite residue after wet air oxidation at 150°C and 180°C.

In conclusion, wet air oxidation performance of Tuncbilek lignite was evaluated by changing three reaction parameters in high pressure batch reactor system. After no time dependence was determined, 15 min was accepted as duration. Then air initial pressure and final temperature were tested. Results revealed that sulfur removal was not sufficient at these experimental conditions.

The effect of subsequent desulfurization on the sulfur removal efficiency was tested at 150°C and 5 bar initial pressure. For this aim, wet air oxidation experiments were conducted for two samples. The experiments were repeated by fresh water and air for four times for sample 16 and 6 times for sample 17. The results of the experiments presented in Table 5.12 indicate that sulfate composition decreases dramatically, while pyritic sulfur removal is not sufficient.

Table 5.12. Repetition experiments at 150°C and 5 bar.

Sample	Repetition #	Heating value (cal/g)	Total S in solid residue by Eschka method (%)	SO <sub>4</sub> <sup>2-</sup> in solid residue (%)	Pyritic Sulfur (%)
Unprocessed lignite	0	3690	3.90	1.20	2.6
16	4	4205	2.89	0.08	1.79
17	6	4122	3.51	0.08	1.78

## 5.4 Conclusions

The structural changes of Tuncbilek lignite during pyrolysis, oxidation, and hydrogenation processes were indicated by XRD, DRIFTS, and solid-state  $^1\text{H}$  and  $^{13}\text{C}$  NMR spectroscopy. The results obtained from these techniques were consistent with each other. NMR and DRIFTS revealed the low carbon aromaticity indicating high reactivity of Tuncbilek lignite.

Approximately 28% volatiles, 5% moisture, 38% ash compositions were determined through both classical proximate analysis and TGA experiments.  $\text{SiO}_2$  ( $53.6 \pm 0.4$  wt%),  $\text{Al}_2\text{O}_3$  ( $24.9 \pm 0.2$  wt%) and  $\text{Fe}_2\text{O}_3$  ( $13.0 \pm 0.1$  wt%) were the main components of lignite ash. Sulfur composition was measured by ESCHKA ( $3.9 \pm 0.2\%$ ) and CHNS analyzer ( $5.4 \pm 0.6\%$ ). The  $^{13}\text{C}$  NMR (CP/MAS) results show that the relative amount of aliphatic carbon present in Tuncbilek lignite is higher than aromatic carbon. DRIFT and  $^{13}\text{C}$  (CP)-MAS NMR analyses of the samples indicate aliphatic, aromatic and C=O double bonds.

Sulfur adsorption ability of PbO and ZnO performed only during hydrogenation experiments was identified by XRD at ambient conditions.

Hydrothermal desulfurization or wet air oxidation experiments demonstrated that sulfate composition of coal can be decreased by this process. However, temperature and pressure tested during process are not sufficient in order to significant sulfur removal. Temperatures higher than  $180^\circ\text{C}$  and pressure higher than 7 bars are recommended to get the efficient sulfur capturing from high sulfur Tuncbilek lignite.



## CHAPTER 6

### UTILIZATION of Co-Pb METAL OXIDES AS OXYGEN CARRIER IN CHEMICAL LOOPING COMBUSTION

#### 6.1 Introduction

CO<sub>2</sub> capture is the most expensive part of the thermal power plants. It requires for both capital and operating cost. For example, in coal based IGCC system, CO<sub>2</sub> capturing increases the cost of electricity by 25% (Fan et al., 2008, Kim et al., 2013). One of the common carbon capture techniques in post-combustion plants is utilization of monoethanolamine (MEA) scrubber. In addition to capital and operating cost, this carbon capture technique decreases the plant efficiency by 10%. In IGCC plants, pre-combustion carbon capture decreases plant efficiency less than MEA, while capital cost is much higher than MEA (Kim et al., 2013). CO<sub>2</sub> capture processes are summarized in Figure 6.1.

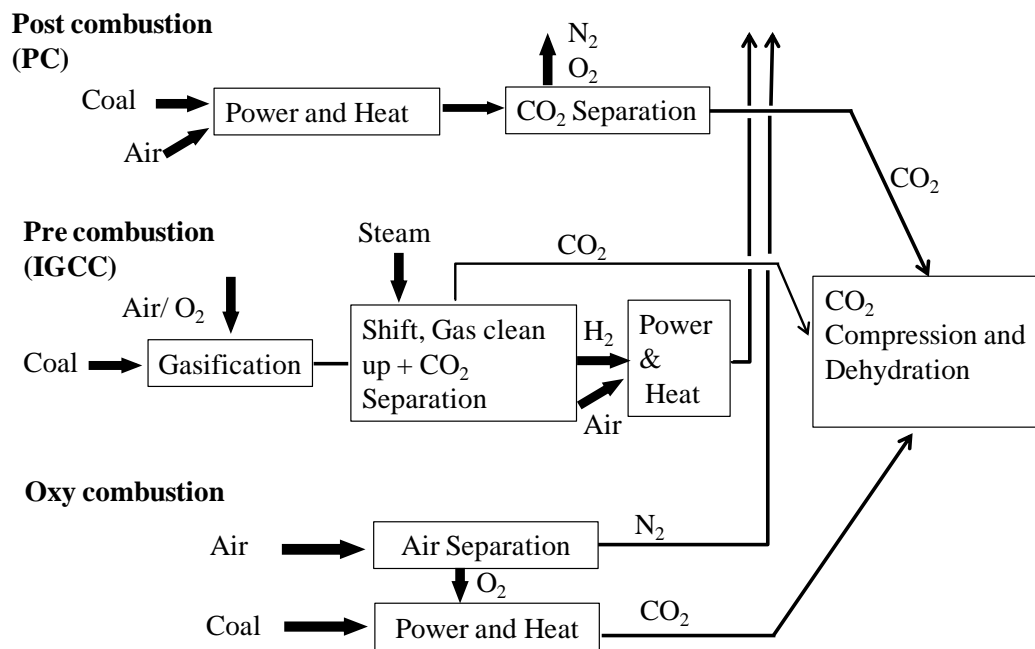


Figure 6.1. Three technologies for CO<sub>2</sub> capture from fossil fuels (GCCSI, 2012).

Unlike these air-combustion based carbon capture technologies, N<sub>2</sub>-free oxy-combustion technologies make ~100% carbon capture possible. Air separation unit (ASU), oxygen transport membrane (OTM) and oxygen carrier metals in a chemical looping system are the main N<sub>2</sub>-free oxygen sources for these systems. Among these resources, ASU

increases the cost of the electricity by 45%, while OTM needs high parasitic energy<sup>3</sup>. Chemical looping system, on the other hand, operates more efficiently and it allows the in situ CO<sub>2</sub> capture without an extra separation unit (Kim et al., 2013). The chemical looping technology gains importance recently for especially coal based fuel combustion process. Types of oxygen carriers and reactors become new research topics for people who are interested in carbon capture and sequestration. Calcium sulfate (CaSO<sub>4</sub>), copper oxide (CuO), and ilmenite (FeTiO<sub>3</sub>) in a fluidized-bed (Zafar et al., 2005) chemical looping system were developed by different research groups. In addition, counter current moving-bed reactor with iron based oxygen carrier was developed by the Ohio State University for coal direct chemical looping system (Fan et al., 2008, Kim et al., 2013). Their bench scale moving-bed reduction reactor provides the 99 vol.% CO<sub>2</sub> capture with high purity (Kim et al., 2013). Syngas chemical looping and Calcium looping systems are still studied (Fan et al., 2008).

The main operating steps of the Chemical Looping Combustion (CLC) in terms of MeO<sub>x</sub> are MeO<sub>x</sub> reduction in fuel reactor and oxidation of the reduced metal oxide in air reactor (Figure 6.2). In addition to oxygen transfer, steam and CO<sub>2</sub> separation is performed by steam condensation. Since there is no direct interaction between the coal and air, no nitrogen separation expending is necessary just like in common coal combustion. Metal oxides commonly used for the chemical looping combustion technology are iron, nickel, copper, and manganese oxides (Siriwardane et al., 2009).

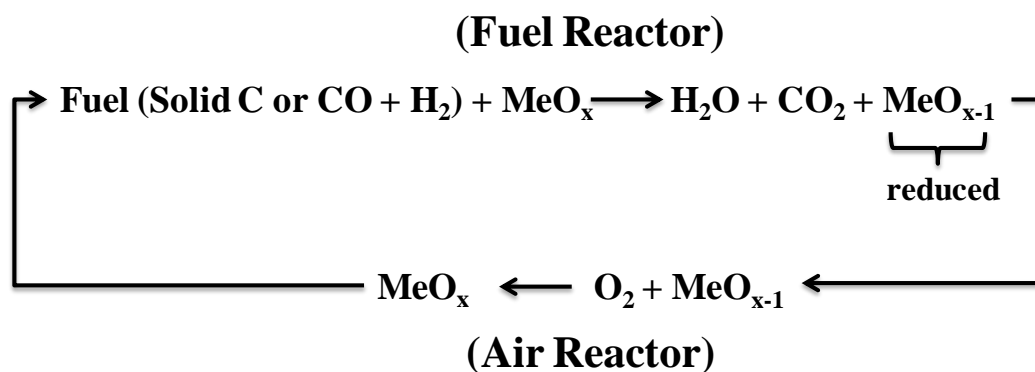
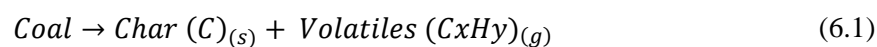


Figure 6.2. Chemical looping combustion system.

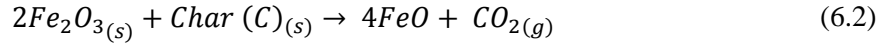
Fe<sub>2</sub>O<sub>3</sub>, for example, was examined for coal, petrocok and char gasification by several researchers (Siriwardane et al., 2009). Kim et al. (2013) listed the possible reactions taking place in the iron oxide based (Fe<sub>2</sub>O<sub>3</sub>) reduction reactor as:

- (i) Devolatilization of coal particles because of the high coal feed temperature.

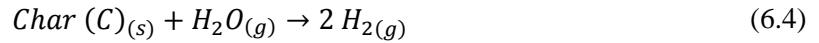
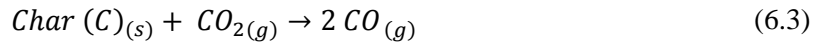


<sup>3</sup> The term parasitic energy is defined as anything that spoils the energy during the process.

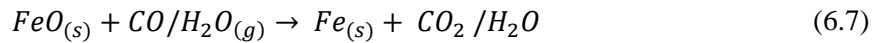
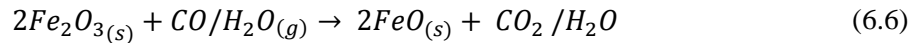
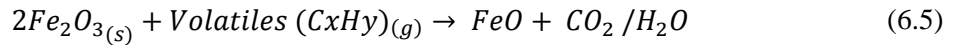
(ii) Char and Fe<sub>2</sub>O<sub>3</sub> solid-solid reaction,



(iii) Char gasification,



(iv) Fe<sub>2</sub>O<sub>3</sub> reduction,



Solid-solid reaction between the char and Fe<sub>2</sub>O<sub>3</sub> is the slowest reaction in the reduction part of the reactor. In this system, CO<sub>2</sub> and H<sub>2</sub>O are initially introduced to the system to increase the carbon conversion. After these gases (CO<sub>2</sub> and H<sub>2</sub>O) are reduced to CO and H<sub>2</sub> during char gasification, they are oxidized again by oxygen carrier, iron oxide (Kim et al., 2013).

The main hints of the CLC system are listed as, selection of suitable metal oxides with high oxygen exchange potential, high resistance against the abrasion, high and stable reactivity, and tolerated interaction with coal inorganics. The circulation of the high amount of ash and appropriate reactor design are mechanistic drawbacks about the CLC systems (Siriwardane et al., 2009, Zafar et al., 2005, Shen et al., 2007).

Siriwardane et al. (2009) tested the oxygen transfer abilities of CuO, Fe<sub>2</sub>O<sub>3</sub>, Mn<sub>2</sub>O<sub>3</sub>, and Co<sub>3</sub>O<sub>4</sub> in the presence of N<sub>2</sub> and/or CO<sub>2</sub>. They followed the interaction between the ash and metal oxide by thermodynamic calculations and XRD. Furthermore, reaction rate and combustion to oxidation ratio were investigated by TGA and fixed-bed reactor system. They found that these oxides have permanent oxidation ability at 700-1000°C. The best oxidation and reduction performance for CuO was obtained during the chemical looping combustion of coal. Low melting point of CuO makes coal chemical looping possible at low temperature (Siriwardane et al., 2009).

Cao and Pan (2006) investigated four types of oxygen carriers namely, Ni, Co, Cu, and Mn oxides, for CLC of solid fuels. Among them, Mn-based oxygen carrier showed a very poor performance because of its low oxygen exchange potential, high reduction

endothermicity, and thermodynamic limitation on CO<sub>2</sub> purification. The rest, on the other hand, show good reduction performance. Two applications were mentioned in this study. According to the first application, after solid fuels are gasified initially by pure O<sub>2</sub> in the gasifier, gaseous products (CH<sub>4</sub>, CO, and H<sub>2</sub>) are sent to the CLC system. Since utilization of the gasifier increases the capital cost, Cao and Pan considered that solid fuel could be sent to the CLC system without any pre-processes. Thus, both solid fuel and syngas oxidation take place in the fuel reactor. The main drawback of this utilization is described as the separation of the reduced metal from carbon char and fly ash. The best oxidation performance was recorded for CoO in this study (Cao and Pan, 2006).

Another challenge of the fossil fuels utilization is SO<sub>x</sub> emission. Sulfur is an unavoidable component in the fossil fuel sources. Garcia-Labiano et al. (2009) studied the effect of H<sub>2</sub>S composition on oxidation performance of the Ni-based oxygen carrier. They found that Ni-based oxygen carrier deactivates due to the presence of H<sub>2</sub>S. Although the new sulfur component of Ni<sub>3</sub>S<sub>2</sub> has a low melting temperature, they did not encounter any agglomeration problem. Ni<sub>3</sub>S<sub>2</sub> formation leads both to decrease sulfur emission and to increase the CO<sub>2</sub> purity in the fuel reactor of CLC system. Deactivation or regeneration capacity of the oxygen carrier is the determining parameter of CLC for high sulfur solid fuels (Garcia-Labiano et al., 2009).

In this part of the study, the effectiveness of Co-Pb metal oxides as oxygen chemical looping agent due to their high oxygen exchange potential is discussed. Thermodynamic calculations of the oxidation and reduction reactions are used to compare the operating temperatures of these types of metal oxides with others.

Since gasification is a partial oxidation process, exploitation of transition metal oxides improves the gasification kinetics and enhances the overall yields. Among all transition metal oxides, cobalt-lead (Co-Pb) mixed metal oxides can be used as an oxygen carrier due to their high oxygen exchange potential. Cobalt and lead based mixed oxide were employed as catalysts for soot oxidation (Uner et al., 2005, Genc et al., 2005). Uner et al. (2005) showed that lead oxides improve the contact between soot and catalyst by forming molten phase and these oxides have catalytic activity. Differential Scanning Calorimeter (DSC) thermograms obtained for pure lead oxide and Co-Pb mixed oxides prove the eutectic mixture formation of Co and Pb as well as molten phase formation. In order to determine the surface composition of catalyst, they used to XPS characterization methods. From the XPS results, cobalt composition was observed to be higher on the surface than in the bulk. They interpreted CoOx particles float on the Pb rich phases in molten and frozen states. Temperature programmed oxidation experiments were performed to test the catalytic activity of CoOx, PbOx, and Co-Pb mixed oxides. The decrease of peak temperature and the increase of reaction rate were observed in the presence of PbOx. CO<sub>2</sub> and CO evolution of TPO experiments carried out in inert atmosphere; indicated the utilization of catalyst lattice oxygen (Uner et al., 2005). Similarity between balance point temperature of onboard test and peak temperature of laboratory reactor test confirmed that the catalytic activity of monolith coated with CoPbOx catalyst are more useful than CoOx catalyst for onboard soot oxidation test

(Genc et al., 2005). Genc et al. (2005) concluded that Pb mobility causes formation of the molten phase at some points of the filter and it increases the catalytic activity for diesel soot oxidation.

Cobalt-Lead (Co-Pb) mixed metal oxides can be used as both oxygen carrier and catalyst due to their high oxygen exchange potential. A thermodynamic analysis on the redox capabilities of these metal oxide indicated superior performance for direct carbon and syngas chemical looping systems. TGA experiments at various coal to Co-Pb metal oxide ratios under inert atmosphere were performed in order to investigate the oxygen release in terms of weight loss. A semi-batch reactor system equipped with an on line gas chromatograph (GC) was used to test the reactivity of coal samples in the presence and in the absence of Co-Pb individual and mixed oxides during the oxidation/pyrolysis processes. In order to compare the performance of individual oxides with cobalt-lead (Co-Pb) mixed metal oxides, same experimental conditions and for coal to catalyst ratio of 10.

## 6.2 Materials and Methods

### 6.2.1 Preparation of Co-Pb individual and mixed metal oxides

Co-Pb metal oxide was prepared by incipient wetness method by combining  $C_4H_6O_4Pb \cdot 3H_2O$  (54.6 % wt Pb, Merck) precursor with  $CoO_x$  (90.8% wt Co, Ege Ferro) powder. The final oxide had a Co/Pb ratio of 1.6/1 by weight. The flow chart for preparing Co-Pb metal oxide is in Figure 6.3. The first step is the mixing of metal precursors in water for 3 hours. The mixture was dried overnight at  $105^\circ C$  and then it was calcined at  $450^\circ C$  for 4 hours. Commercial  $PbO$ ,  $CoO_x$  as received from the vendor and the mixed oxide were used during pyrolysis and oxidation experiments.

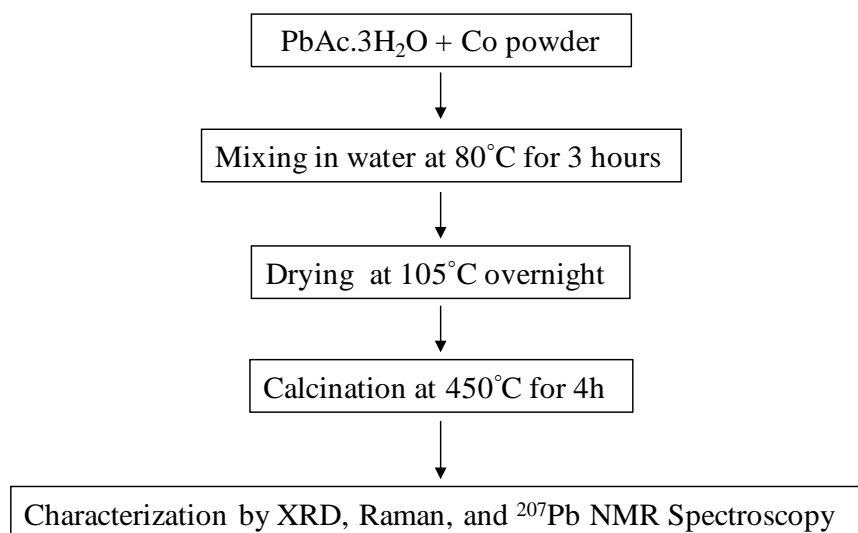


Figure 6.3. Co-Pb metal oxide preparation steps.

## 6.2.2 Characterization of Co-Pb individual and mixed metal oxides

XRD patterns were measured on a Philips model PW1840 (1729) X-ray diffractometer using Ni filtered Cu-K $\alpha$  radiation at a scan rate of 0.05°/sec.

Bruker IFS 66/S, FRA 106/S, HYPERION 1000, RAMANSCOPE II was used for Raman patterns.

A home built Lap-NMR spectrometer using an external magnetic field of 75MHz was employed for the  $^{207}\text{Pb}$  NMR experiments where CPC NMR Plus (1000 W 1-30 MHz) amplifier was also used for radio frequency pulses. All experiments were conducted at approximately 5 kHz MAS using a 4mm Doty Scientific XC probe.<sup>4</sup>

The visual images of the reactor after pyrolysis and oxidation were taken by HP-deskjet digital camera, while microscopic images were obtained by using Karl Suss PM5, 5X objective. The possible sulfur compounds of Pb were only characterized by XRD.

## 6.3 Results and Discussion

### 6.3.1 Oxidation and Reduction thermodynamics of Co-Pb metal oxides

The standard Gibbs free energy values of oxidation and reduction reactions of Co-Pb metal oxides were calculated as a function of temperature. The standard Gibbs free energies of formation data for components were obtained from literature and data are tabulated in Appendix A. The related equation is;

$$\Delta G_{rxn} = (\Delta G^f)_{products} - (\Delta G^f)_{reactants} \quad (6.8)$$

Figure 6.4 indicates the free energy changes of red-ox reactions in the presence of different reducing agents. The unusual representation of reaction 1 indicating the utilization of half a carbon to produce half a carbon dioxide is preferred in order to base the comparisons per mole of PbO (or CoO) compound. When temperature is higher than 970 K, the most favorable reaction is the partial oxidation of carbon reaction with PbO, while the best reducing agent is carbon monoxide when temperature is less than 970 K. Additionally, the minimum temperature value of 570 K is favorable for the partial oxidation of carbon. These reduction behaviors are compatible with the oxidation reactions.

---

<sup>4</sup>  $^{207}\text{Pb}$  NMR measurements were performed at University of California-Berkeley

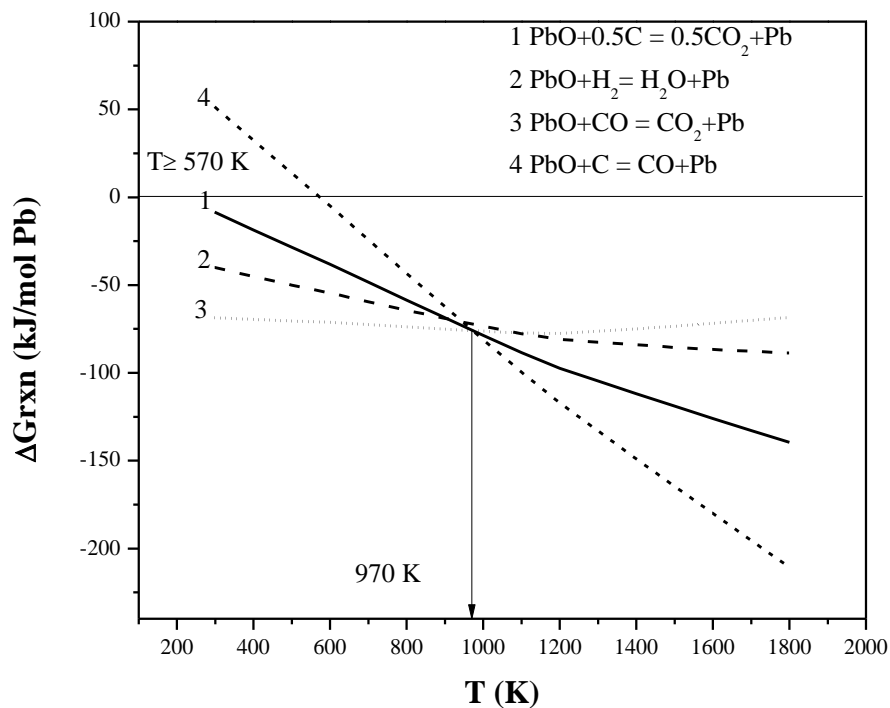


Figure 6.4. Standard Gibbs free energy change during lead oxide reduction.

The redox reactions of CoO with  $\text{H}_2$  and CO are shown in Figure 6.5. Similar to PbO, CoO reduction reaction with CO is the most favorable reaction when temperature is less than 977 K. On the other hand, carbon partial oxidation is the easiest reaction at temperatures higher than 977 K.

When we compare the reduction thermodynamics of CoO and PbO, we concluded that PbO can give its oxygen to both  $\text{H}_2$  and C easier than CoO (in Figure 6.6). The minimum free energies belong to Pb compounds at all temperatures. In order to determine the behavior of the mixed oxides, a series of experiments were performed. For example, TGA experiments under air and inert atmosphere give an idea about the oxygen intake and release processes.

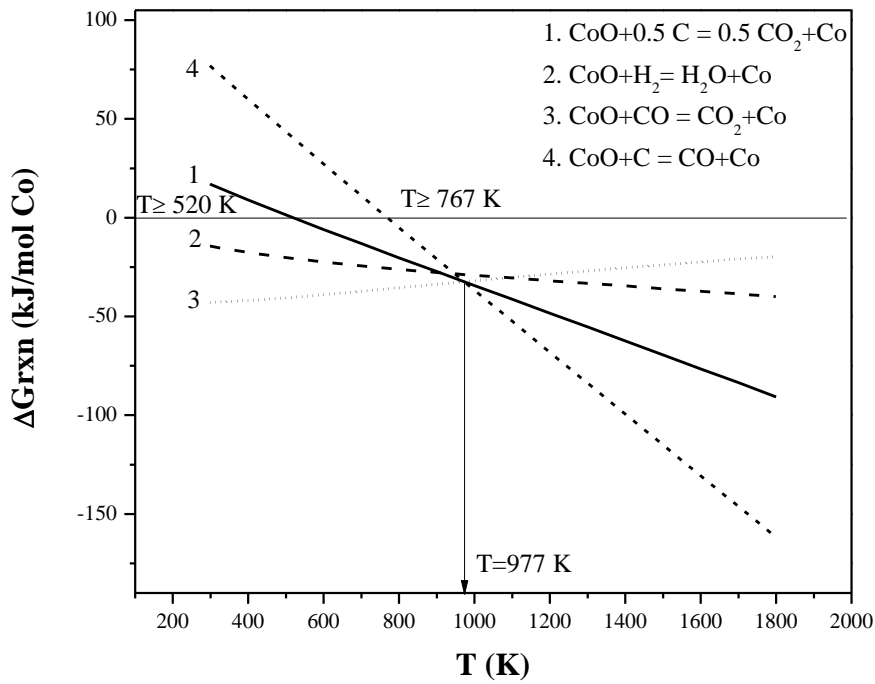


Figure 6.5. Standard Gibbs free energy change during Cobalt oxide reduction.

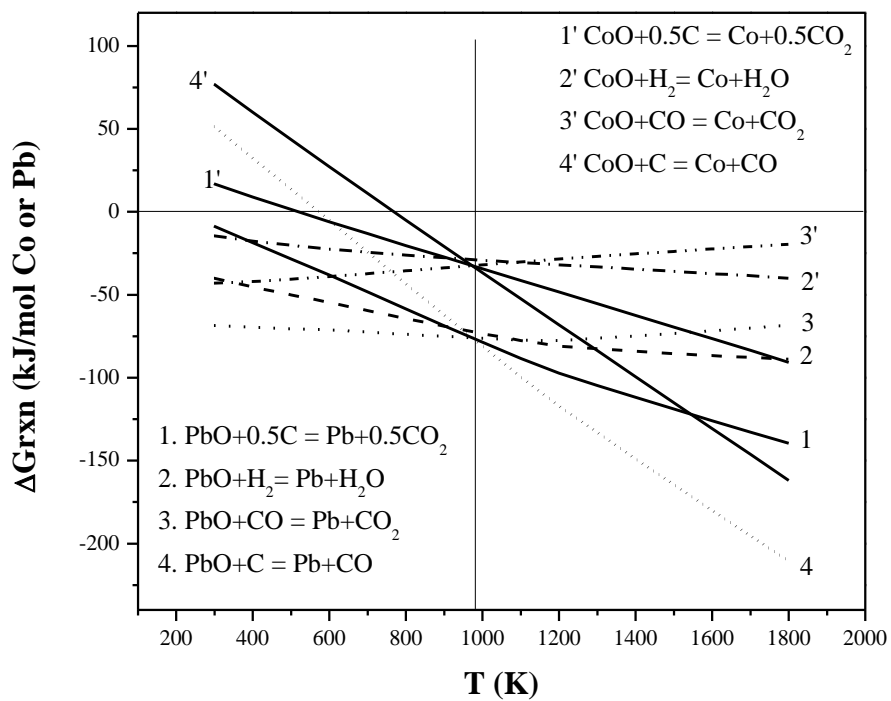


Figure 6.6. Comparison between the PbO and CoO reduction with Carbon, Hydrogen, and Carbon monoxide.

### 6.3.2 TGA experiments under inert atmosphere in various amount of Co-Pb metal oxide.

The coal: metal oxide mixtures were studied with TGA under inert atmosphere in order to determine their oxygen release activity. As seen in Figure 6.7, the peak oxidation temperatures of high loading (10 to 2 coal/ metal oxide ratios) coal/Co-Pb oxides are around 100°C higher than low loading (1 and 0.25) coal/Co-Pb oxides. When coal to metal oxides ratio is higher than 2 (Figure 6.7), only one peak is observed around 450°C. On the other hand, when the ratio of coal to Co-Pb metal oxides is less than 1, two distinct peaks are observed in the temperature range of 280-320°C, with a minor component left at around 450°C. As a result, the presence of Co-Pb metal oxides affects peak temperature. Co-Pb metal oxide utilization provides the high reaction rates by decreasing the reaction temperature.

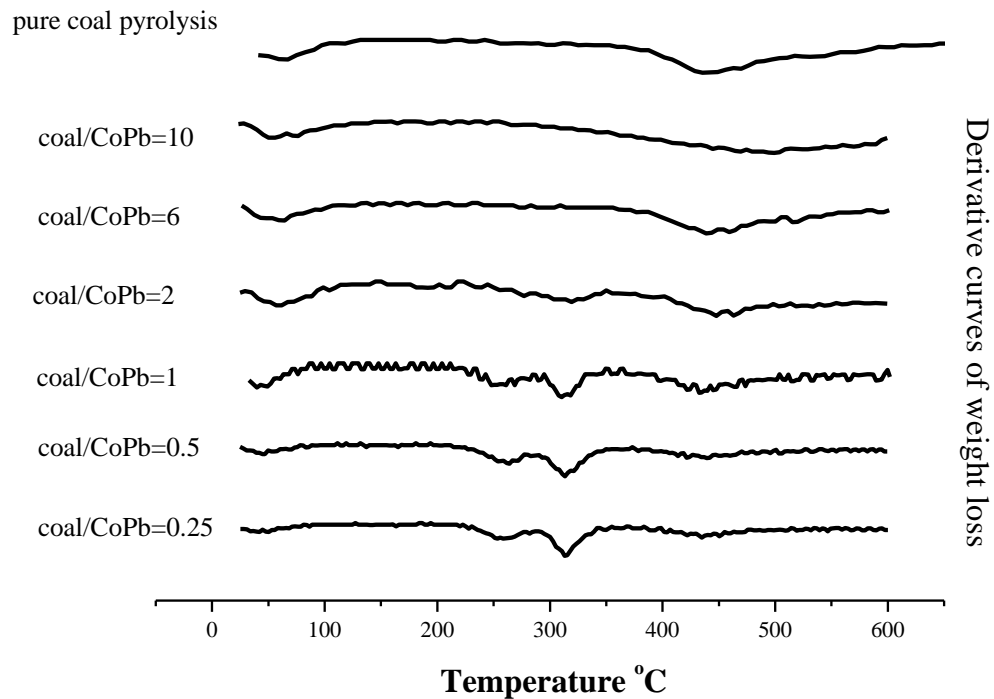


Figure 6.7. TGA pyrolysis thermograms of coal in the presence of different metal oxide contents.

### 6.3.2 Characterization of Co-Pb metal oxides

#### 6.3.2.1 XRD patterns of Co-Pb metal oxides

When all oxidation states of Pb and Co were investigated, possible oxide formations of Pb and Co such as PbO, PbO<sub>2</sub>, Pb<sub>3</sub>O<sub>4</sub>, and Pb<sub>2</sub>O<sub>3</sub>, CoO, Co<sub>2</sub>O<sub>3</sub> and Co<sub>3</sub>O<sub>4</sub> were checked within the XRD databank. PbO was determined as the only Pb oxide form while the

oxide form of Co was determined to be  $\text{Co}_3\text{O}_4$ . The specific  $\text{Co}_3\text{O}_4$  peak values was also monitored as approximately,  $37^\circ$ ,  $65^\circ$  and  $31^\circ$  in literature (Weidenthaler, 2011). Specific Bragg angle values of PbO and  $\text{Co}_3\text{O}_4$  are presented in Figure 6.8.

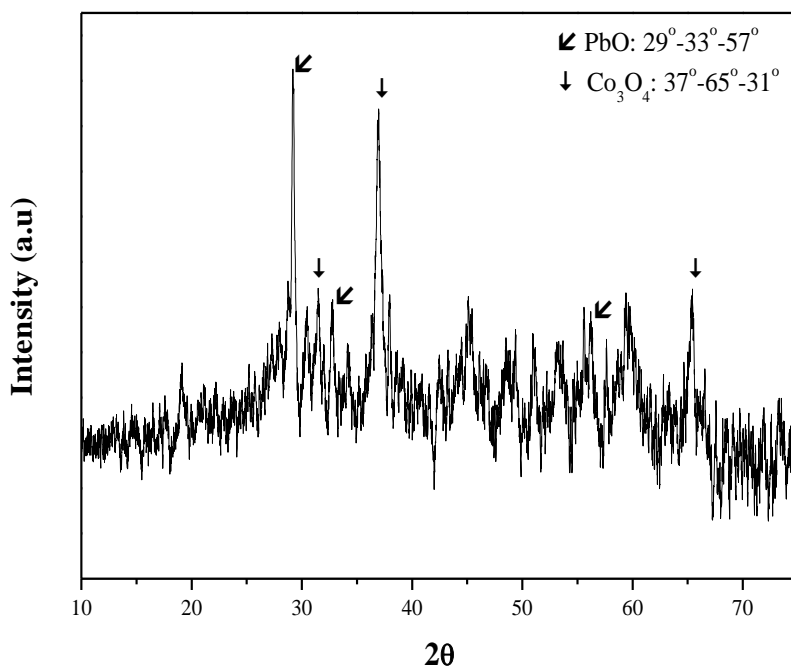


Figure 6.8. XRD patterns of Co-Pb based metal oxides.

### 6.3.2.2 Raman spectra of Co-Pb metal oxides

Raman spectrum of Co-Pb metal oxide is presented in Figure 6.9. The oxidation states of these metals are labeled on each spectrum. The characteristic Raman spectrum of  $\text{Co}_3\text{O}_4$  revealed peaks at around 196, 486, 524, 620 and  $697\text{ cm}^{-1}$  (Shen et al., 2008, Lopes et al., 2006, Yung et al., 2008). The experimental frequency values for the Pb oxide formation were reported as Pb–O–Pb bend  $124\text{ cm}^{-1}$ , Pb–O stretch  $386, 365, 290\text{ cm}^{-1}$  (Jensen, 2003). PbO appears in two geometrical structures, one is tetragonal litharge  $\alpha\text{-PbO}$  at  $145\text{ cm}^{-1}$  and the other is orthorhombic massicot  $\beta\text{-PbO}$  in  $285\text{ cm}^{-1}$  wavenumber (Jensen, 2003). The characteristic Raman bands of PbO and  $\text{Co}_3\text{O}_4$  obtained from related article are tabulated in Table 6.1.

Table 6.1. Characteristic Raman shifts of  $\text{Co}_3\text{O}_4$  and PbO.

Types of oxides	Raman Shifts ( $\text{cm}^{-1}$ )
$\text{Co}_3\text{O}_4$	196, 486, 524, 620, 695
PbO	145 for $\alpha\text{-PbO}$ and 285 for $\beta\text{-PbO}$

In conclusion, PbO and Co<sub>3</sub>O<sub>4</sub> formation are also confirmed by Raman spectroscopy.

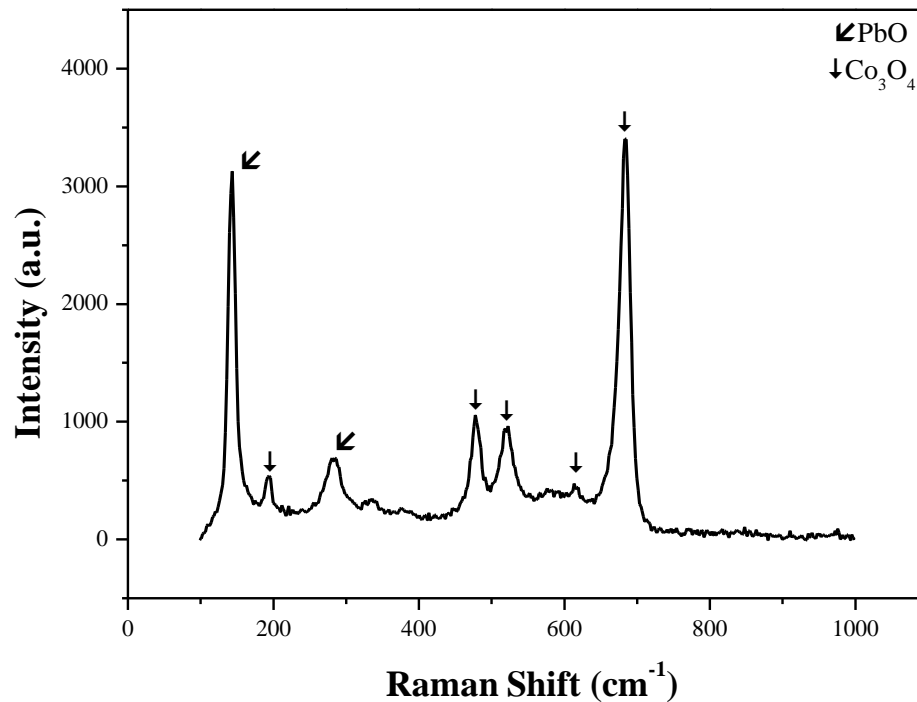


Figure 6.9. Raman spectra of Co-Pb metal oxide.

### 6.3.2.3 <sup>207</sup>Pb MAS-NMR spectra of Co-Pb metal oxides

Pb containing materials are used in optical and electrical applications even though they are known as toxic. For example, PbO can be used as radiation sensors because of its optical property (Glatfelter et al., 2011). Similarly, PbS, which is a semi-conductor with narrow band gap, is used for infrared lasers and detectors (Dybowski and Neue, 2002, Zhao et al., 1999). The NMR spectroscopy makes it possible to distinguish both materials from each other and different stages of a single material (Van Bramer et al., 2006).

Solid state <sup>207</sup>Pb NMR spectroscopy provides the structural and bonding information about the lead based materials. Although lead has four isotopes in nature, only <sup>207</sup>Pb isotope is NMR active because of the spin quantum number of 1/2 (Dybowski and Neue, 2002). The natural abundance of lead isotope (<sup>207</sup>Pb) is 22.1%. The reference compound of <sup>207</sup>Pb is lead tetramethyl for the NMR analysis ( $\delta_{iso}=0$ ). Pb(NO<sub>3</sub>)<sub>2</sub> is also used as a secondary reference, whose isotropic chemical shift is -3490 ppm at 25°C (Glatfelter et al., 2011). Chemical shift range is between -5500 to 6000 ppm.

One of the <sup>207</sup>Pb NMR limitations is broad line spectrum. In order to solve this problem, we used a lower field magnet (75MHz) which makes it possible to obtain the entire

spectrum with a single experiment. Although we did not obtain Pb signals for the samples unprocessed and processed Pb based materials,  $^{207}\text{Pb}$  MAS-NMR spectra of reference compounds ( $\text{PbO}$ ,  $\text{PbS}$ , and  $\text{PbSO}_4$ ) are presented in this section. Initially,  $\text{Pb}(\text{NO}_3)_2$  solid powder was mixed with reference Pb based compounds at a mol/mol ratio of 1/9. The referencel Pb-based materials were obtained from Aldrich Chemical Co. Inc. with a stated purity of 99.999 % for  $\text{PbO}$ , 99.995 % for  $\text{PbSO}_4$  and 99.9% for  $\text{PbS}$ .

### *PbO and Pb(NO<sub>3</sub>)<sub>2</sub> mixture*

The first experiment was conducted for the mixture of the  $\text{PbO-Pb}(\text{NO}_3)_2$ . This  $\text{PbO}$ , called as massicot, has orthorhombic unit cell (Zhao et al., 1999). Since  $\text{PbO}$  peak is very broad and relaxation delay is very high ( $\sim 25\text{s}$ ), experiments take long time. As seen in Figure 6.10, two signals were obtained at approximately 642 ppm for  $\text{PbO}$  and -5461 ppm for  $\text{Pb}(\text{NO}_3)_2$  in the presence of 15.506 MHz carrier frequency. When we compare the signal intensities, the signal intensity of  $\text{Pb}(\text{NO}_3)_2$  is very narrow, while  $\text{PbO}$  peak position highly broad.

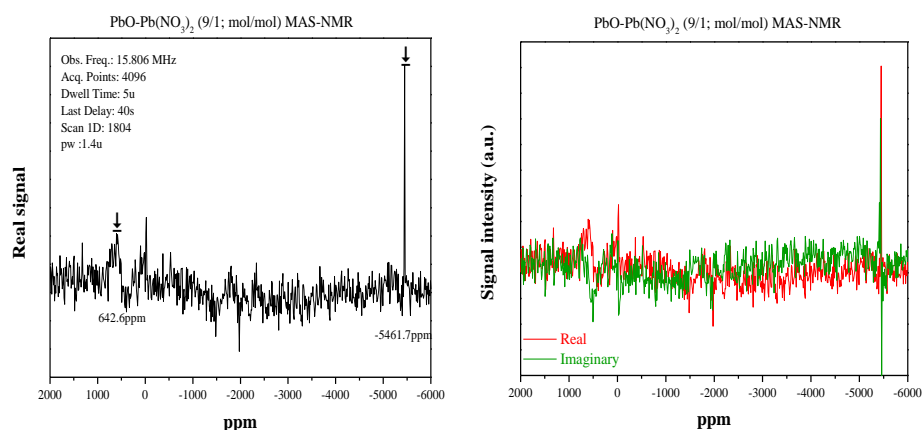


Figure 6.10. The  $^{207}\text{Pb}$  MAS spectrum of reference compounds of  $\text{PbO-Pb}(\text{NO}_3)_2$ .

### *PbS and Pb(NO<sub>3</sub>)<sub>2</sub> mixture*

This compound has a cubic structure like sodium chloride (Neue et al., 1996). In Figure 6.11,  $\text{PbS}$  signal is observed at 2106 ppm, while the peak position of  $\text{Pb}(\text{NO}_3)_2$  was evaluated as -2738 ppm at carrier magnetization of 15.763MHz.

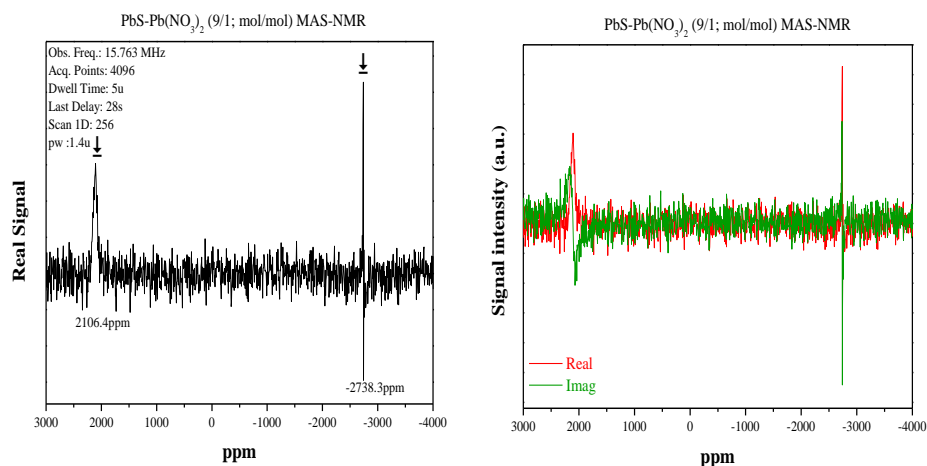


Figure 6.11. The  $^{207}\text{Pb}$  MAS spectrum of reference compounds of  $\text{PbS-Pb}(\text{NO}_3)_2$ .

### *PbSO<sub>4</sub> and Pb(NO<sub>3</sub>)<sub>2</sub> mixture*

The last experiment among the commercial Pb compounds was carried out with  $\text{PbSO}_4$ . The commercial  $\text{PbSO}_4$  was also mixed with  $\text{Pb}(\text{NO}_3)_2$  at the same molar ratio (9/1). As mentioned in literature  $\text{PbSO}_4$  and  $\text{Pb}(\text{NO}_3)_2$  are ionic components and their signals are very close to each other (Zhao et al., 1999). In this compound, a single lead site is present (Van Bramer et al., 2006). As seen in Figure 6.12, the peak position of the  $\text{Pb}(\text{NO}_3)_2$  and  $\text{PbSO}_4$  are -5449ppm and -5573 ppm, respectively.

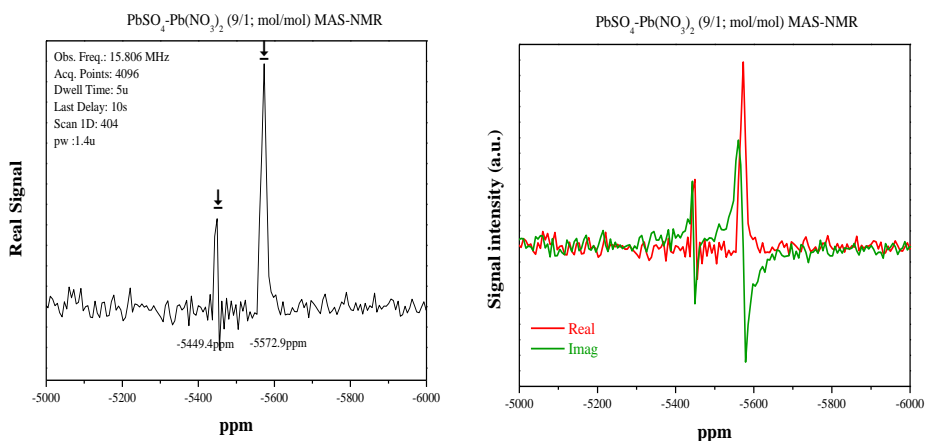


Figure 6.12. The  $^{207}\text{Pb}$  MAS spectrum of reference compounds of  $\text{PbSO}_4\text{-Pb}(\text{NO}_3)_2$ .

When  $^{207}\text{Pb}$  measurements were performed for unprocessed Co-Pb metal oxide,  $\text{Pb}(\text{NO}_3)_2$  was mixed with Pb based materials qualitatively.  $^{207}\text{Pb}$  chemical shifts were reported with respect to solid  $\text{Pb}(\text{NO}_3)_2$  as an external secondary standard. In addition,

spin-echo pulse sequence was used to decrease the effect of acoustic ringing. Thus, spin-echo pulse sequence experiment allows to check that the broad line is signal or ring down. The block diagram of the spin-echo pulse sequence is summarized on the real part of Figure 6.13. According to Figure 6.13, it is not possible to elucidate the peaks considered to be signals. Although signal from the samples could not be acquired, the results from the reference compounds still offer promise for the future work.

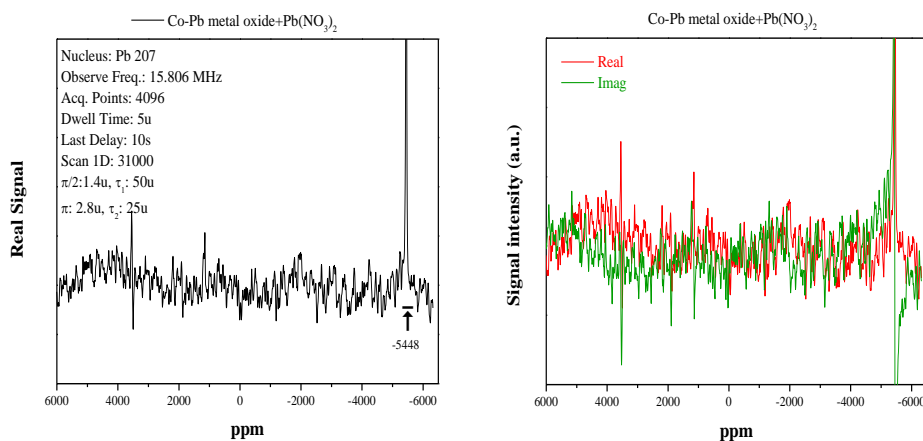


Figure 6.13. The  $^{207}\text{Pb}$  MAS spectrum of Co-Pb metal oxide-  $\text{Pb}(\text{NO}_3)_2$  with spin-echo.

### 6.3.3 Gasification performance of individual Co and Pb oxides and Co-Pb mixed metal oxides

#### 6.3.3.1 $\text{CH}_4$ and $\text{H}_2$ production under $\text{N}_2$ flow in the presence of Co-Pb individual and mixed metal oxides

$\text{CH}_4$ ,  $\text{H}_2$ ,  $\text{CO}$ , and  $\text{CO}_2$  were the main products observed during temperature-programmed experiments under  $\text{N}_2$  flow. The results are summarized in Figure 6.14 for  $\text{CH}_4$  formation rate and Figure 6.15 for  $\text{H}_2$  formation rate. In addition to  $\text{CH}_4$  and  $\text{H}_2$  formation rate vs temperature graph,  $\text{CO}_2$  formation rate is demonstrated in Figure 6.16. This figure verifies the oxygen transfer from the metal oxide structure when coal to metal oxide ratio is 1 (or metal oxide amount increased by 10).

Figure 6.14 shows that  $\text{CH}_4$  formation rate reaches maximum value at  $500^\circ\text{C}$ . However, the presence of Co-Pb metal oxides do not change  $\text{CH}_4$  formation rate. Both individual Co and Pb and also Co-Pb mixed oxide have the same effect on  $\text{CH}_4$  formation rate when coal to metal oxide ratio is 10.

As seen in Figure 6.15,  $\text{H}_2$  formation started at  $350^\circ\text{C}$  and reached its maximum value at around  $700^\circ\text{C}$ . Similar curves were obtained in the presence or absence of the metal oxides. As a result, the utilization of oxides does not have any influence on the production of  $\text{H}_2$  as well.

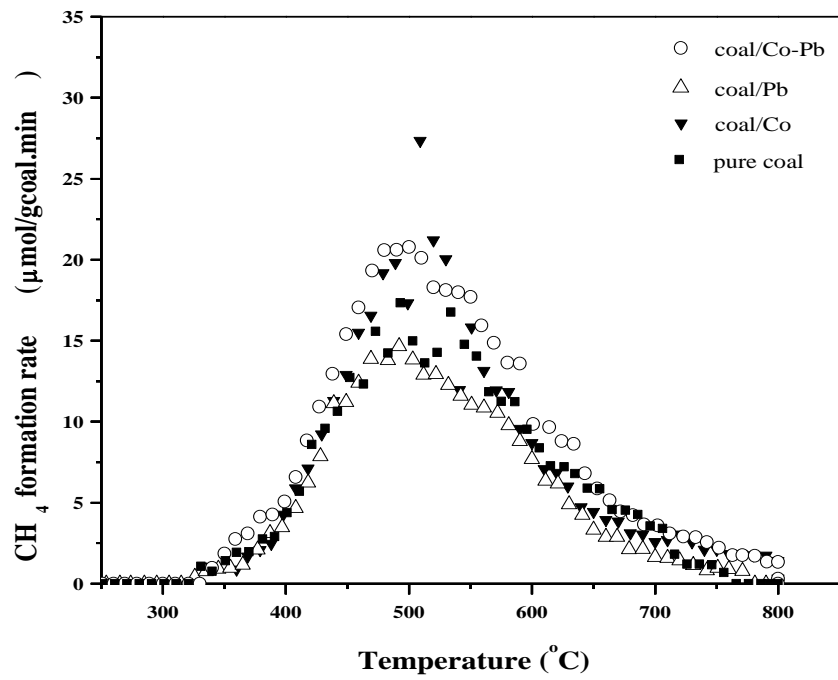


Figure 6.14. CH<sub>4</sub> formation rates under N<sub>2</sub> flow using the constant coal: metal oxide ratio of 10 (wt/wt).

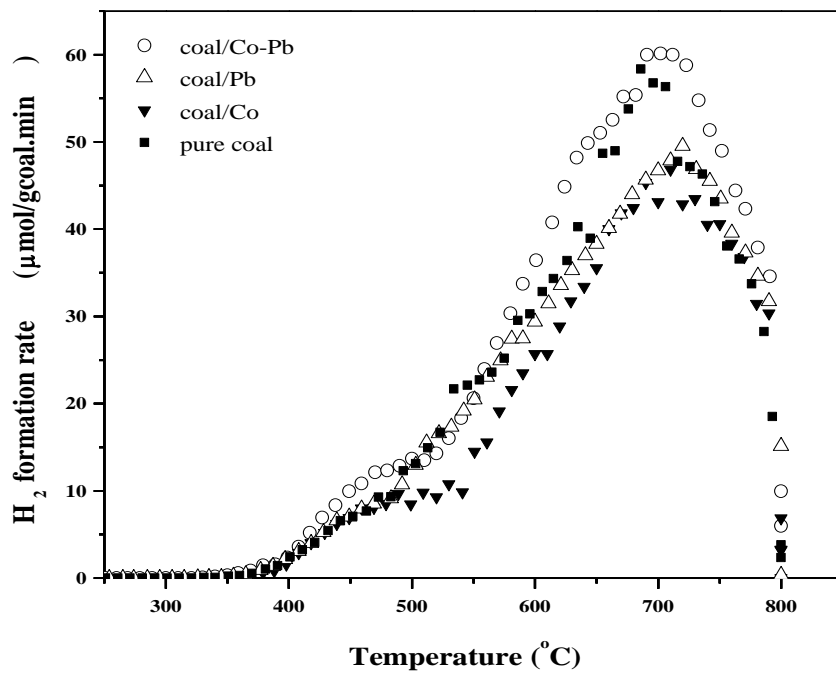


Figure 6.15. H<sub>2</sub> formation rates under N<sub>2</sub> flow using the constant coal: metal oxide ratio of 10 (wt/wt).

As seen in Figure 6.16, CO<sub>2</sub> formation rate increases significantly in the presence of high amount of Co-Pb metal oxide. When coal/Co-Pb metal oxide was 1, 6000 μmol CO<sub>2</sub>/gcoal (Table 6.2) was produced under N<sub>2</sub> atmosphere.

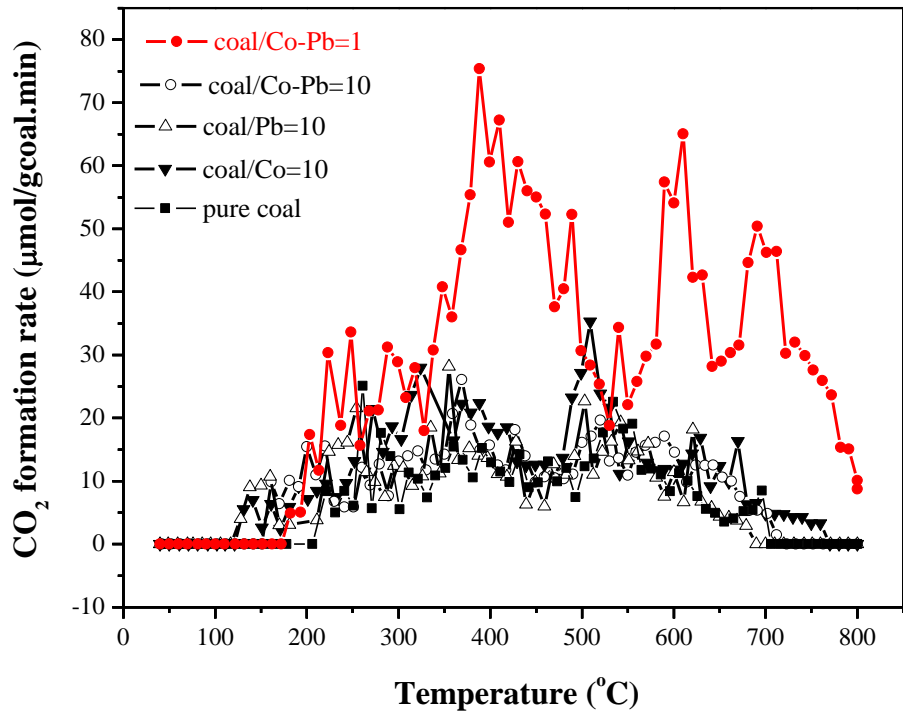


Figure 6.16. CO<sub>2</sub> formation rates under N<sub>2</sub> flow in the presence and absence of metal oxide.

Additionally, CO<sub>2</sub> formation rates of coal/Co-Pb =1 under N<sub>2</sub> flow and pure coal under air flow were compared in Figure 6.17. As seen in this figure, coal oxidation data was multiplied by 0.1 in order to compare the changes of CO<sub>2</sub> formation rates with temperature in both situations. CO<sub>2</sub> formation was completed at about 500°C during air oxidation, while CO<sub>2</sub> formation was observed up to 800°C during pyrolysis in the presence of Co-Pb mixed metal oxides. This result revealed that the presence of Co-Pb metal oxide may change the oxidation reaction mechanism of Tuncbilek lignite.

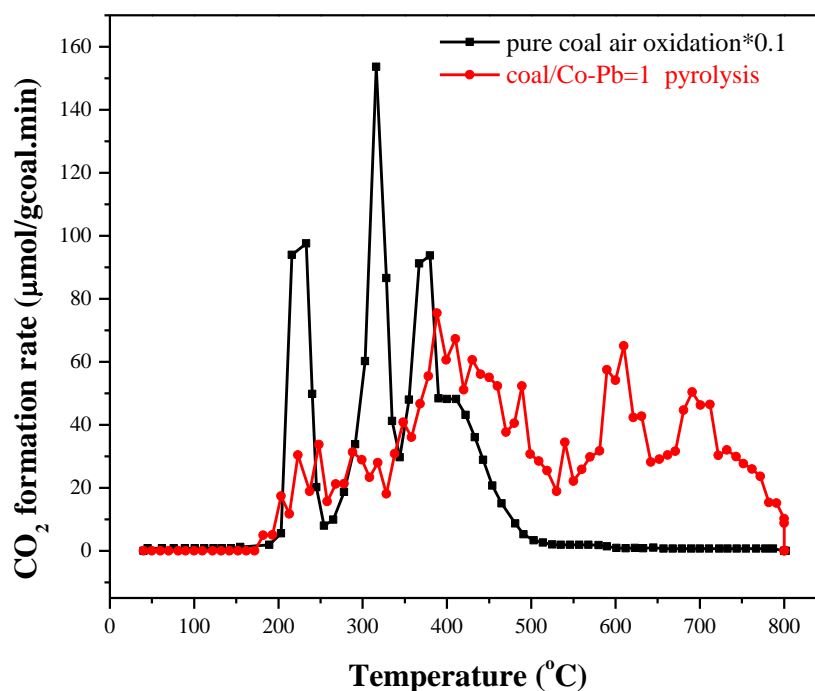


Figure 6.17. CO<sub>2</sub> formation rates of pure coal during air oxidation and coal/Co-Pb=1 during pyrolysis.

Total amounts of CH<sub>4</sub> and H<sub>2</sub> products during pyrolysis were tabulated in Table 6.2. It can be seen that the presence of individual and mixed metal oxide decreases the CH<sub>4</sub> and H<sub>2</sub> yields. Especially when coal to Co-Pb mixed metal oxide was 1, these products were in the lowest level. In order to check the formation of oxidation products, the same calculations were done for carbon-based products. The results are presented in Table 6.3.

Table 6.2. Total amount of CH<sub>4</sub> and H<sub>2</sub> formed under N<sub>2</sub> flow.

Sample name	CH <sub>4</sub> (µmol/gcoal)	H <sub>2</sub> (µmol/gcoal)
Coal/Co=10	985.4	1840.0
Coal/Pb=10	726.1	3043.5
Coal/Co-Pb=10	1119.4	3720.9
Coal/Co-Pb=1	570.3	1176.4
Pure Coal	1786.8	3376.7

As seen in Table 6.3, total amounts of oxidation products (CO and CO<sub>2</sub>) are higher for the sample of coal/Co-Pb =1 than for the other samples. Additionally, carbon conversion was calculated as 29.7% for this sample, while CH<sub>4</sub> formation was 570 μmol/gcoal.

Table 6.3. Total carbon conversion under N<sub>2</sub> flow.

Sample name	CH <sub>4</sub> (μmol/gcoal)	CO (μmol/gcoal)	CO <sub>2</sub> (μmol/gcoal)	C conversion (%)
Coal/Co=10	985.4	953.3	2229.6	12.5
Coal/Pb=10	726.1	994.9	1627.2	10.0
Coal/Co-Pb=10	1119.4	1192.4	1792.9	12.3
Coal/Co-Pb=1	570.3	3338.5	6000.9	29.7
Pure Coal	1786.8	1901.5	2909.9	19.8

In conclusion, pyrolysis data proves the oxidation ability of Co-Pb metal oxides under inert atmosphere at appropriate coal to metal oxide ratios.

### 6.3.3.2 CH<sub>4</sub> and H<sub>2</sub> production under air flow in the presence of Co-Pb individual and mixed metal oxides

During the air oxidation experiments, coal to Co and Pb individual and mixed oxides ratio was fixed to 10. The experiments were repeated twice and the average of the two experimental data was used in the graphs and calculations.

As seen in Figures 6.18 and 6.19, under air flow, the evolution of CH<sub>4</sub> and H<sub>2</sub> has started at lower temperatures than observed under N<sub>2</sub> flow (~200°C). We anticipate the local hot spots due to the combustion reactions and heat transfer resistances. Excess energy available including heat makes the decomposition of coal and removing of the volatiles easier. On the other hand, the maximum CH<sub>4</sub> and H<sub>2</sub> formation rates under air flow were obtained as one order of magnitude lower than under N<sub>2</sub> flow. In general, the presence of oxygen decreases the CH<sub>4</sub> and H<sub>2</sub> formation rates due to their subsequent oxidation.

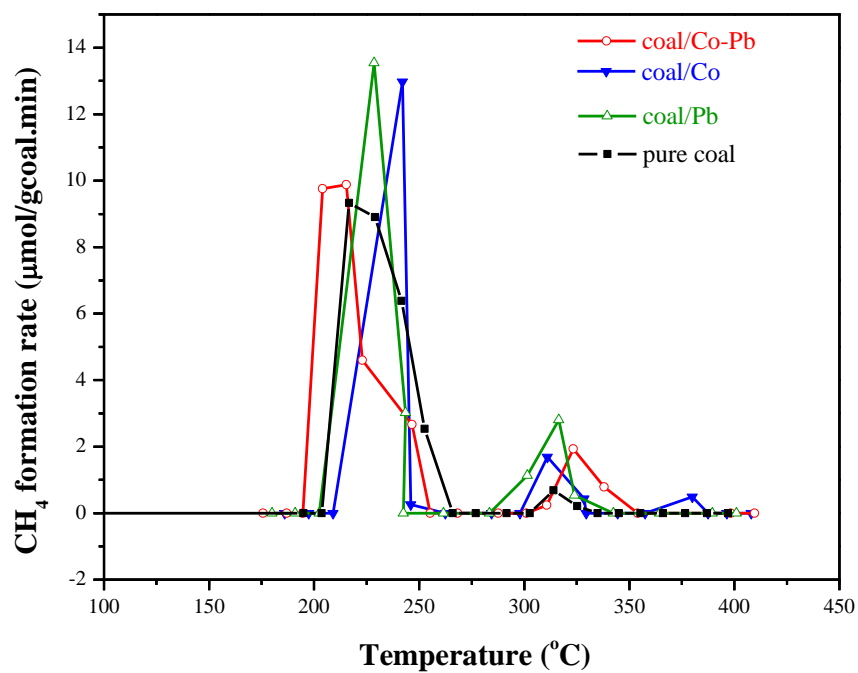


Figure 6.18. CH<sub>4</sub> formation rates under air flow using the constant coal: metal oxide ratio of 10 (wt:wt).

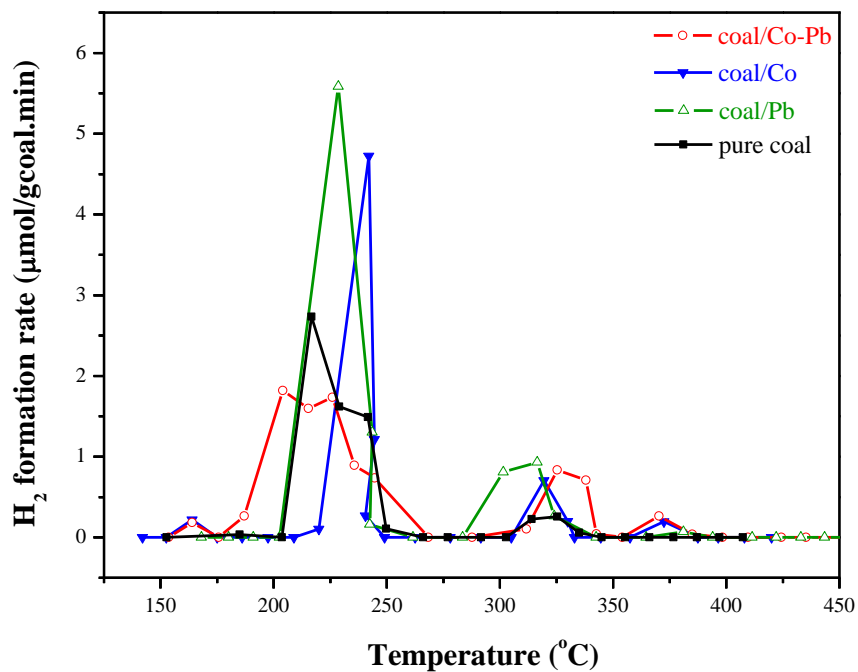


Figure 6.19. H<sub>2</sub> formation rates under air flow using the constant coal: metal oxide ratio of 10 (wt:wt).

CO<sub>2</sub> formation rate presented in Figure 6.20 does not show any variation in the presence of metal oxide. Both individual and mixed oxide causes the similar CO<sub>2</sub> emission behavior.

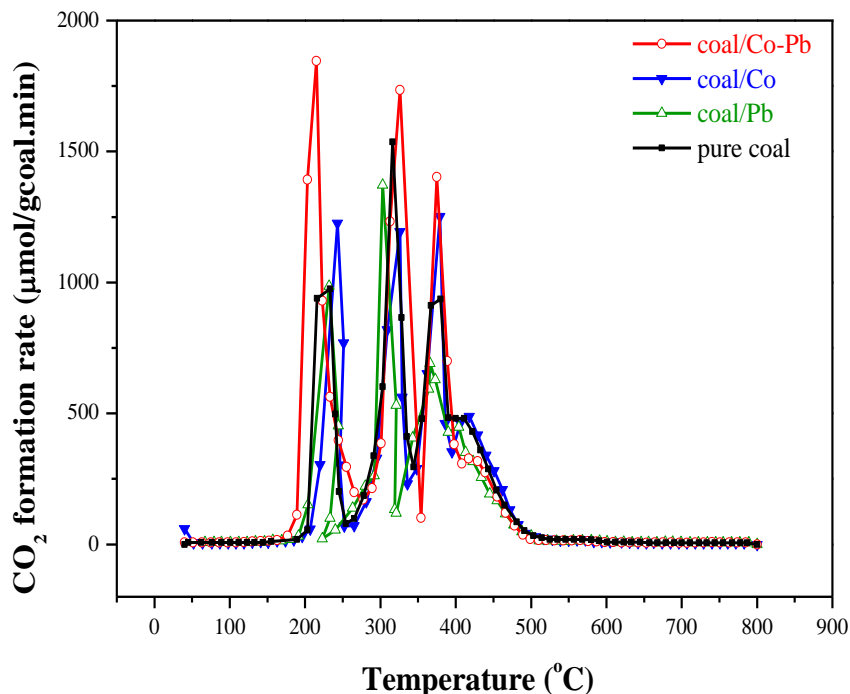


Figure 6.20. CO<sub>2</sub> formation rate in the presence and absence of metal oxides using the fix coal: metal oxide ratio of 10.

In order to show how oxidation takes place on char, pyrolysis residues of samples namely, pure coal, coal/ Co-Pb metal oxide =10, and coal/ Co-Pb metal oxide =1, were combusted under air flow. As seen in Figure 6.21, the combustion characteristic of pyrolysis residues changes when coal to Co-Pb metal oxide ratio is 1.

In order to compare the results, oxidation performance of all samples was collected in the same table. Integrated amounts of gaseous products (CH<sub>4</sub> and H<sub>2</sub>) throughout the measurements are given in Table 6.4. Similar oxidation behaviors were obtained in the presence and absence of metal oxides. Total amount of CH<sub>4</sub> and H<sub>2</sub> with respect to gram coal initially put in to the reactor indicates that Co and Pb metal oxides do not affect the CH<sub>4</sub> and H<sub>2</sub> formation.

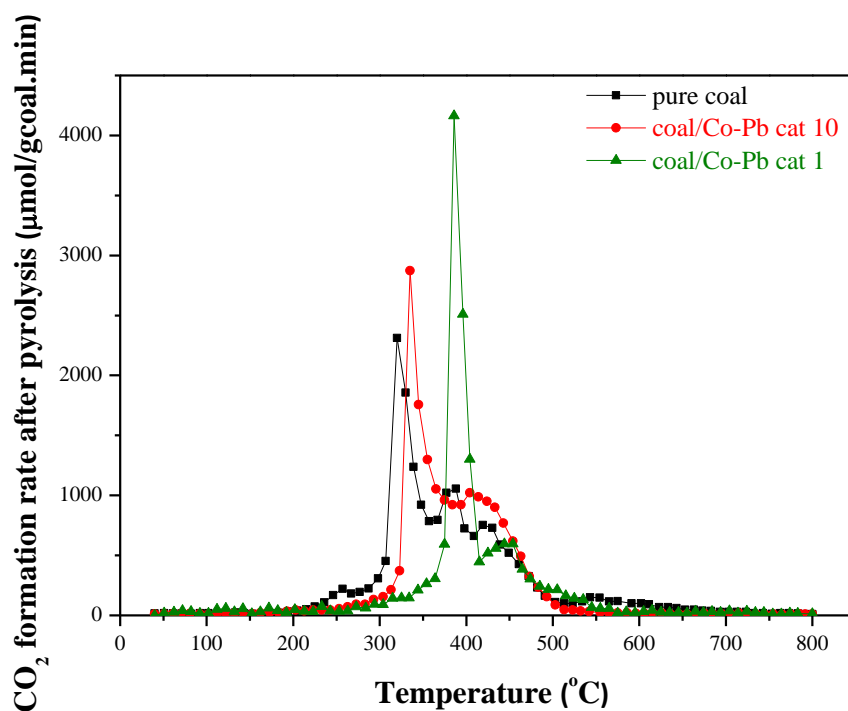


Figure 6.21. CO<sub>2</sub> emission during air oxidation of the pyrolysis residues.

Total amounts of CH<sub>4</sub>, CO, and CO<sub>2</sub> are summarized together with C conversion in Table 6.5. In order to determine the carbon conversion, total amount of CH<sub>4</sub>, CO and CO<sub>2</sub> are divided by the initial amount of carbon in coal structure. It can be seen that carbon conversion of coal is very high (>100%), and the utilization of Co-Pb based metal oxides has no important effect on carbon conversion. The excess of 100% is believed to be due to higher carbon fractions present in the particular coal sample than was measured by the elemental analysis.

Table 6.4. Total amount of CH<sub>4</sub> and H<sub>2</sub> formed under air flow.

Sample name	CH <sub>4</sub> (µmol/gcoal)	H <sub>2</sub> (µmol/gcoal)
Coal/Co	50.1	20.3
Coal/Co-Pb	92.1	27.4
Coal/Pb	56.8	24.7
Pure Coal	81.6	21.8

Table 6.5. Total carbon conversion under air flow.

Sample name	CH <sub>4</sub> ( $\mu\text{mol/gcoal}$ )	CO ( $\mu\text{mol/gcoal}$ )	CO <sub>2</sub> ( $\mu\text{mol/gcoal}$ )	C conversion (%)
Coal/Co	50.1	930.9	34332.8	106.0
Coal/Co-Pb	92.1	4924.6	38195.1	129.6
Coal/Pb	56.8	355.0	31486.0	95.7
Pure Coal	81.6	3316.4	37106.9	110.0

In conclusion, the utilization of Co-Pb individual and mixed oxides does not influence the pyrolysis and oxidation products of Tuncbilek, significantly at the coal to catalyst ratio of 10. At this point, the sulfur capture ability of this type oxide should be tested.

The high pyritic sulfur content of coal was already recognized in the literature as its role for the improved combustion and gasification rates upon the release of H<sub>2</sub>S (Artok et al., 1992). The aqueous oxidation of pyrite is highly exothermic and can provide the energy needed to ignite the rest of the coal (Lowson, 1982). However, during these processes, the sorption effect of these metal oxides on sulfur removal is unique. The mixed oxide characterization after both oxidation and pyrolysis processes revealed that galena (PbS) formation is inevitable. Therefore, PbO appears as a very good candidate to be used as an in situ or ex situ sulfur trap. Furthermore, the presence of metal oxides decreases the amount of tar collected at the inner walls of the quartz reactor.

#### 6.3.4 Pb-based materials for sulfur recovery

Lead based metal oxide can be preferred as sulfur trap during the pyrolysis, oxidation and hydrogenation processes. However, if PbO is placed separately from coal, molten metallic Pb formation can be observed at the end of the pyrolysis and oxidation experiments because of the high oxygen release potential of PbO and low melting point of the metallic lead. The molten metallic Pb migrated to the end of the reactor.

The visual images of Pb migration and microscopic images of PbO reduction to metallic Pb during pyrolysis and oxidation reactions can be seen in Figure 6.22.

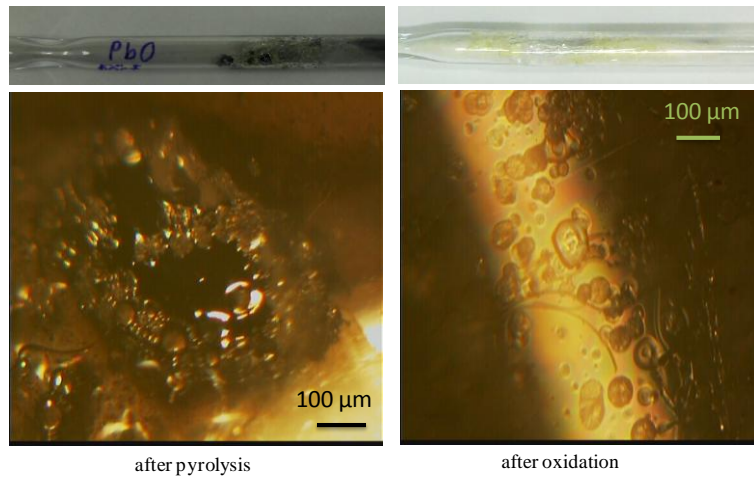


Figure 6.22. The visual and microscopic images of PbO reduction to metallic Pb during pyrolysis and oxidation reactions.

During oxidation experiments, similar observation was obtained for molten both PbO and metallic Pb. It can be concluded from these findings that it is not possible to hold up sulfur in coal structure if Pb based metal oxide is not mixed with coal. On the other hand, the presence of Co-Pb mixed oxides in coal structure allows the sulfur hold up for pyrolysis, oxidation, and hydrogenation processes. In Figure 6.23, XRD spectra obtained on the samples before and after pyrolysis and oxidation processes are presented. Star symbols on b, c, and d spectra represent the carbon residue after each process.

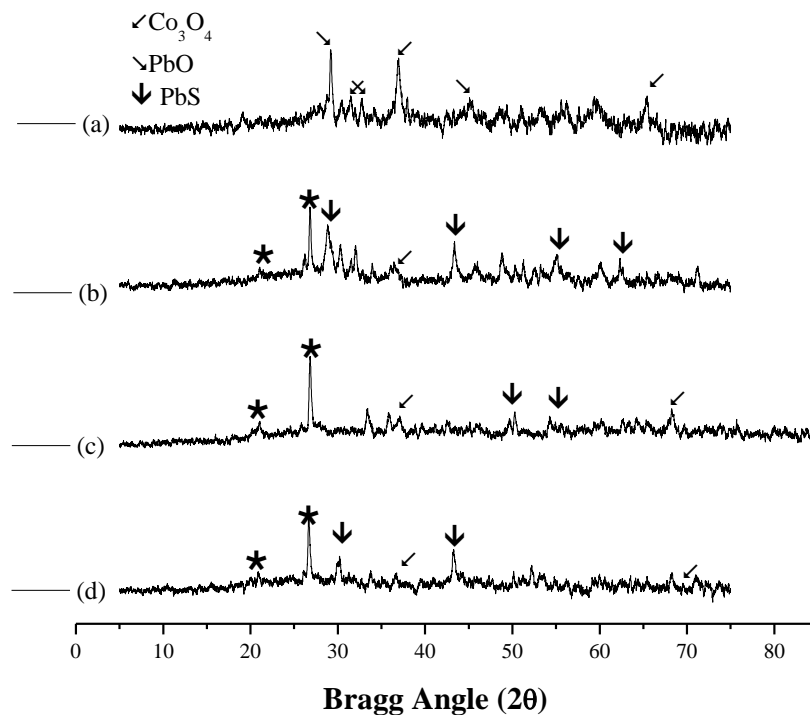


Figure 6.23. In-situ sulfur capture potential of PbO: (a) fresh Co-Pb metal oxide, (b) after pyrolysis, (c) after oxidation, and (d) after hydrogenation.

When PbS is considered as a target product, XRD patterns of pyrolysis, oxidation, and hydrogenation residues reveal clear peaks for PbS formation. The utilization of Co-Pb metal oxides allows the sulfur capture during these processes. Sulfidation products of the Co-Pb metal oxide, on the other hand, should be regenerated as the oxygen source of the chemical looping system.

In a chemical looping system, there is a fuel reactor and air reactor in order to loop oxidation agent. In the air reactor part, reduced metal coming from fuel reactor is oxidized by air. The major distinction proposed in this study is that MeS oxidation instead of metal. The thermodynamics of PbS oxidation with SO<sub>2</sub>, SO<sub>3</sub> and H<sub>2</sub>SO<sub>4</sub> as possible oxidation products were conducted. In addition to SO<sub>2</sub>, SO<sub>3</sub> compounds, H<sub>2</sub>SO<sub>4</sub> is synthesized if H<sub>2</sub>O is an oxidation product. Oxidation thermodynamics of PbS is demonstrated in Figure 6.24. According to the Figure 6.24, all reactions are possible and PbO formation is more favorable than metallic Pb. No thermodynamic limitations are available for Pb oxidation.

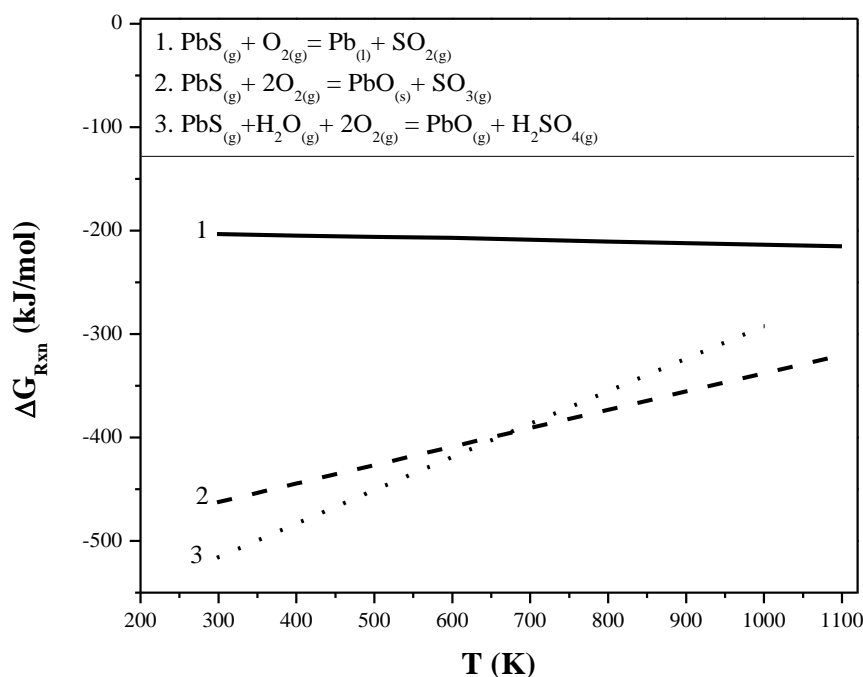


Figure 6.24. Oxidation thermodynamics of PbS.

As seen from the PbS oxidation reactions, chemical looping makes it possible to obtain three important raw materials especially for fertilizer industry. Thus, SO<sub>x</sub> capturing are provided in Co-Pb chemical looping system. Figure 6.25 is the schematic representation of the sulfur looping system.

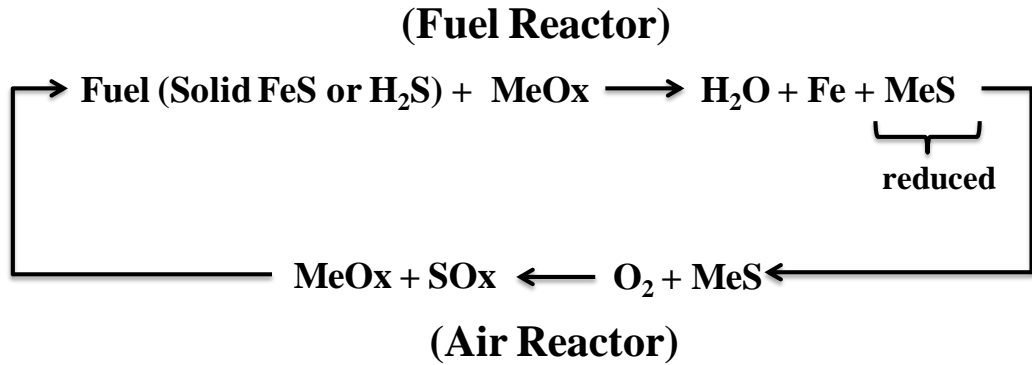


Figure 6.25. Sulfur looping flow diagram.

## 6.4 Conclusions

From the thermal gravimetric analysis results, Co-Pb mixed metal oxides decrease the peak oxidation temperature of Tuncbilek lignite from 450°C to 320°C in N<sub>2</sub> atmosphere. Under N<sub>2</sub> flow, the variation of oxidation products with metal oxide amount reveals that the lattice oxygen of the Co-Pb individual and mixed metal oxides is being used in the process. When coal:metal oxide ratio is 1, CO<sub>2</sub> formation becomes favorable. The oxides were used as oxidizing medium due to their high oxygen exchange potential. Thermodynamic calculations of oxidation reactions were carried out for CoO and PbO. Among the three main reactions for each oxide, char oxidation reaction by CoO oxygen carrier is favorable at temperatures higher than 520 K. On the other hand, there is no thermodynamic limitation for the rest reactions. The XRD and Raman results clearly indicate that Co and Pb are present in the oxide form of Co<sub>3</sub>O<sub>4</sub> and PbO. Although previous knowledge of the soot oxidation ability and lattice oxygen utilization in oxygen free conditions were proven, their relatively poor activity for lignite pyrolysis and oxidation processes was probably due to the already high activity of the coal in the presence of pyrite. Pyrolysis experiments under N<sub>2</sub> flow demonstrate that CH<sub>4</sub> and H<sub>2</sub> are important coal gasification products, and their formation begins at the temperatures higher than 350°C. In addition, Co-Pb based metal oxides do not influence CH<sub>4</sub> and H<sub>2</sub> formation rates during pyrolysis process. On the contrary, oxidation experiments under air flow indicate that the presence of O<sub>2</sub> makes CH<sub>4</sub> and H<sub>2</sub> formation possible at around 200°C most probably driven by the exothermic oxidation reactions ignited at these temperatures. Moreover, the amount of CH<sub>4</sub> and H<sub>2</sub> produced during the oxidation process was calculated as not much higher in the presence of metal oxides than in the absence of them. To sum up, pyrolysis and oxidation ability of Tuncbilek lignite are relatively high and the use of Co-Pb based metal oxides does not adversely affect the fate of these processes. The affinity PbO towards sulfur capture was confirmed.



## CHAPTER 7

### DISCUSSION AND CONCLUSIONS

The main approach of this study is to develop the fundamental understanding about both gasification and desulfurization characteristics of Tuncbilek lignite.

Conventional and advanced characterization techniques allow a better understanding of reactivity of Tuncbilek lignite. Approximately 28% volatiles, 5% moisture, and 38% ash contents were determined through both classical proximate analysis and TGA experiments. The CHNS analyzer determined elemental composition of Tuncbilek lignite as carbon ( $37.7 \pm 0.7$  wt%), hydrogen ( $3.6 \pm 0.1$  wt%), nitrogen ( $1.6 \pm 0.1$  wt%), and sulfur ( $5.4 \pm 0.6$  wt%). Sulfur composition was measured by ESCHKA ( $3.9 \pm 0.2$ ). Pyritic sulfur and sulfate were determined as  $2.6 \pm 0.1$  and  $1.2 \pm 0.1$ , respectively.  $\text{SiO}_2$  ( $53.6 \pm 0.4$  wt%),  $\text{Al}_2\text{O}_3$  ( $24.9 \pm 0.2$  wt%) and  $\text{Fe}_2\text{O}_3$  ( $13.0 \pm 0.1$  wt%) were the main inorganic components of lignite structure determined by XRF. XRD pattern of Tuncbilek lignite demonstrated that there is two characteristic carbon peaks associated with aliphatic carbon at  $20^\circ$  and inorganic carbon at  $27^\circ$ . The other inorganic components detected by XRD, can be listed as kaolinite ( $13^\circ$ ,  $25^\circ$ ), pyrite ( $33^\circ$ ,  $56^\circ$ , and  $47^\circ$ ), calcite, and dolomite ( $29^\circ$ ,  $41^\circ$ ). DRIFT spectrum of coal sample indicated aliphatic, aromatic and C=O double bond as well as  $^{13}\text{C}$  NMR (CP/MAS). Additionally, DRIFTS was also utilized in order to identify inorganic coal structure. The  $^{13}\text{C}$  NMR (CP/MAS) result shows that the relative amount of aliphatic carbon present in Tuncbilek coal is nearly twice higher than aromatic carbon. This finding reveals the low carbon aromaticity and high reactivity of Tuncbilek lignite. Consequently, Tuncbilek lignite is high in ash and sulfur but low in carbon and hydrogen contents.

Pyrolysis, air oxidation, hydrogenation, and wet air oxidation are the basic reactions taking place during gasification depending on the type of reactant. Therefore, these reactions were investigated separately in this study. In this context, X-ray Diffraction Spectroscopy, Diffuse Reflectance Infrared Fourier Transformation Spectroscopy and solid-state Proton and Carbon NMR spectroscopy were very informative on the structural changes of lignite samples after all these processes. Thus, these methods show that gasification processes are promising instruments to estimate coal reactivity.

Pyrolysis experiments under  $\text{N}_2$  flow demonstrated that  $\text{CH}_4$  and  $\text{H}_2$  are important gaseous pyrolysis products, and their formation began at the temperatures higher than  $350^\circ\text{C}$ . On the contrary, oxidation experiments under airflow indicated that the presence of  $\text{O}_2$  makes  $\text{CH}_4$  and  $\text{H}_2$  formation possible at around  $200^\circ\text{C}$  most probably driven by the exothermic oxidation reactions ignited at these temperatures. The integrated amount

of CH<sub>4</sub> and H<sub>2</sub> is a magnitude higher at pyrolysis condition than at oxidation condition. However, total carbon conversion was calculated as approximately 20% during pyrolysis, while >100% during oxidation.

XRD patterns of the pyrolysis, oxidation, and hydrogenation processes revealed that inorganic carbon structure of Tuncbilek lignite is non reactive. The possible reason may be considered that the presence of Si and Al molecules around carbon prevents the reactant gas and carbon interaction. The removal of kaolinite peaks was also another common observation of all processes. Since maximum sulfur removal was achieved during the hydrogenation process, sulfur capture ability of PbO and ZnO were tested at laboratory conditions and XRD results reveal the sulfur capture ability of these oxides. DRIFTS results also confirm the results of XRD. Common results of three processes can be listed as: inorganic –OH bands disappeared during all processes due to the thermal decomposition of the hydroxyl ions in organic and inorganic structure. The disappearance of absorption band around 2981cm<sup>-1</sup> is associated with CH stretching vibration band based on aliphatic chain. The reason of this extinction may be due to the high reactivity of aliphatic carbon structure. Another common property for three processes is that the removal of the bands at 1434, 916, and 695 cm<sup>-1</sup> is due to the CO<sub>3</sub><sup>=</sup> substituted inorganic minerals of calcite, dolomite and pyrite. <sup>1</sup>H and <sup>13</sup>C (CP) MAS NMR results revealed that there is no proton detected in carbon residue of oxidation and hydrogenation. However, <sup>1</sup>H NMR spectrum of pyrolysis residue demonstrated the similar peaks (-0.6 and 6.7 ppm) to that observed for unprocessed coal. This shows the aliphatic and aromatic protons are still present in coal pyrolysis residue. On the other hand, no proton signal was detected beyond the background from <sup>1</sup>H NMR of the oxidation and hydrogenation residues. This result was also another indication of the disappearance of C-H bonds in the oxidation and hydrogenation residues as deduced from the DRIFTS spectra of the same samples. <sup>13</sup>C-NMR spectra of coal pyrolysis residue revealed that the presence of aromatic carbon structure. The main structural change was the removal of the shoulder peak at 154 ppm associated with the oxy-substituted (phenolic) carbon structure. Since the chemical bonds in protonated carbons are weak, reaction tendency of protonated carbons is higher than nonprotonated carbons. <sup>1</sup>H and <sup>13</sup>C (CP) MAS NMR spectra of liquid hydrogenation products show the presence of similar types of protons and carbons together with phenolic, carboxylic and amide carbons. Elemental analysis results of coal pyrolysis and hydrogenation processes indicated that the 92% sulfur removal is possible under pure H<sub>2</sub> flow. On the other hand, the results of the hydrothermal treatment or wet air oxidation experiments revealed that sulfur contents of the Tuncbilek lignite did not change at the selected experimental conditions. In addition, the formation of characteristic XRD PbS and ZnS peaks during the hydrogenation process revealed that PbO and ZnO can be used for sulfur adsorption at ambient condition.

The chemical looping technology gains importance recently for especially coal based fuel combustion process. Types of oxygen carriers are new research topics for people who are interested in carbon capture and sequestration. The oxygen exchange potential of Cobalt-Lead (Co-Pb) based metal oxides were tested in both pyrolysis and oxidation processes. Moreover, the affinity PbO and Co<sub>3</sub>O<sub>4</sub> towards sulfur capture was examined

for all processes. It was found that Cobalt-Lead (Co-Pb) based metal oxides are the good candidates for oxygen transfer. Thermodynamic calculations showed that reduction reactions of CoO and PbO are favorable above 520 K. Derivative curves of TGA indicated that the presence of Co-Pb metal oxides affects both peak formation temperature and the contents of products. Peak positions are dependent on coal to Co-Pb metal oxides ratio. High amount of Co-Pb metal oxides utilization allows the two peaks formation at low temperature. The XRD and Raman data clearly indicate that Co and Pb are present in the oxide form of  $\text{Co}_3\text{O}_4$  and PbO. Another advanced characterization technique; solid state  $^{207}\text{Pb}$  NMR measurements were conducted in order to characterize the lead based materials, synthesized and used for pyrolysis, oxidation, and hydrogenation processes. Although lead signals were obtained for the reference compounds, namely PbO, PbS and  $\text{PbSO}_4$ , no Pb NMR signal was recorded for our samples. Additionally, the use of Co-Pb based metal oxides does not adversely affect methane and hydrogen formation rate during the pyrolysis and oxidation of Tuncbilek lignite. On the contrary, the utilization of appropriate amounts of Co-Pb metal oxide proves the oxidation ability of these oxides. The affinity of PbO towards sulfur capture was confirmed by XRD.

Finally, characteristics of coal, the utilization aim of the product gases, operation conditions and environmental regulations are determining parameters for the more effective and environmentally friendly coal utilization. In this context, there is a gap between the science and technology. In order to eliminate this gap, applied research can be conducted in coal utilization technologies.

As a future work, the utilization of Co-Pb based metal oxides seems very promising chemical looping agent for both oxygen transfer and sulfur capturing. Therefore, chemical looping systems based on these materials can be analyzed in detail in terms of the system economics.



## REFERENCES

- Arenillas, A., Rubiera, F., Pevida, C., Ania, C. O., Pis, J. J. 2004. Relationship between structure and reactivity of carbonaceous materials. *Journal of Thermal Analysis and Calorimetry*, 76, 593-602.
- Arenillas, A., Rubiera, F., Pis, J. J., Cuesta, M. J., Iglesias, M. J., Jimenez, A., Suarez-Ruis, I. 2003. Thermal behaviour during the pyrolysis of low rank perhydrous coals. *Journal of Analytical and Applied Pyrolysis*, 68-9, 371-385.
- Artok, L., Schobert, H. H., Davis, A. 1992. Temperature -staged liquefaction of coals impregnated with ferrous sulfate. *Fuel Processing Technology*, 32, 87-100.
- Ashwini, K., Pandurangappa, C., Nagabhushana, B. M. 2012. Synthesis and optical properties of undoped and Eu-doped ZnS nanoparticles. *Physica Scripta*, 85.
- Azik, M., Yurum, Y., Gaines, A. F. 1993. Air oxidation of Turkish Beypazari lignite .1. Change of structural characteristics in oxidation reactions at 150-degrees-c. *Energy & Fuels*, 7, 367-372.
- Balaz, P., Balintova, M., Bastl, Z., Briancin, J., Sepelak, V. 1997. Characterization and reactivity of zinc sulphide prepared by mechanochemical synthesis. *Solid State Ionics*, 101, 45-51.
- Balaz, P., Pourghahramani, P., Achimovicova, M., Dutkova, E., Kovac, J., Satka, A., Jiang, J. Z. 2011. Mechanochemical synthesis and reactivity of PbS nanocrystals. *Journal of Crystal Growth*, 332, 1-6.
- Barin, I. (ed.) 1989. *Thermochemical data of pure substances*. New York : VCH, 1989.
- Baruah, B. P., Khare, P. 2007. Pyrolysis of high sulfur Indian coals. *Energy & Fuels*, 21, 3346-3352.
- Batchelder, H. R., Busche, R.M., Armstrong, W. P. 1953. Kinetics of Coal Gasification Proposed Mechanism of Gasification. *Ind. and Eng. Chem*, 45.
- Bois, L., Maquet, J., Babonneau, F., Mutin, H., Bahloul, D. 1994. Structural characterization of sol-gel derived oxycarbide glasses .1. Study of the pyrolysis process. *Chemistry of Materials*, 6, 796-802.
- Breen, C., Clegg, F., Herron, M. M., Hild, G. P., Hillier, S., Hughes, T. L., Jones, T. G. J., Matteson, A., Yarwood, J. 2008. Bulk mineralogical characterisation of oilfield reservoir rocks and sandstones using Diffuse Reflectance Infrared Fourier Transform Spectroscopy and Partial Least Squares analysis. *Journal of Petroleum Science and Engineering*, 60, 1-17.

- Cakal, G. O., Yucel, H., Guruz, A. G. 2007. Physical and chemical properties of selected Turkish lignites and their pyrolysis and gasification rates determined by thermogravimetric analysis. *Journal of Analytical and Applied Pyrolysis*, 80, 262-268.
- Calkins, W. H. 1994. The chemical forms of sulfur in coal - a review. *Fuel*, 73, 475-484.
- Cao, Y., Pan, W. P. 2006. Investigation of chemical looping combustion by solid fuels. 1. Process analysis. *Energy & Fuels*, 20, 1836-1844.
- Cetinkaya, S., Yurum, Y. 2000. Oxidative pyrolysis of Turkish lignites in air up to 500 degrees C. *Fuel Processing Technology*, 67, 177-189.
- Chin, A. K., Camlibel, I., Sheng, T. T., Bonner, W. A. 1983. Extremely rapid out diffusion of sulfur in INP. *Applied Physics Letters* 43 495-497.
- Conte, P., Piccolo, A., van Lagen, B., Buurman, P., Hemminga, M. A. 2002. Elemental quantitation of natural organic matter by CPMAS C-13 NMR spectroscopy. *Solid State Nuclear Magnetic Resonance*, 21, 158-170.
- Cook, R. L., Langford, C. H., Yamdagni, R., Preston, C. M. 1996. A modified cross-polarization magic angle spinning C-13 NMR procedure for the study of humic materials. *Analytical Chemistry*, 68, 3979-3986.
- Damen, K., van Troost, M., Faaij, A., Turkenburg, W. 2006. A comparison of electricity and hydrogen production systems with CO<sub>2</sub> capture and storage. Part A: Review and selection of promising conversion and capture technologies. *Progress in Energy and Combustion Science*, 32, 215-246.
- Delarosa, L., PruskI, M., Lang, D., Gerstein, B., Solomon, P. 1992. Characterization of the Argonne premium coals by using H-1 and C-13 NMR and FT-IR Spectroscopies. *Energy & Fuels*, 6, 460-468.
- Demirbas, A., Balat, M. 2004. Coal desulfurization via different methods. *Energy Sources*, 26, 541-550.
- Descamps, C., Bouallou, C., Kanneche, M. 2008. Efficiency of an Integrated Gasification Combined Cycle (IGCC) power plant including CO<sub>2</sub> removal. *Energy*, 33, 874-881.
- Di Blasi, C. 2009. Combustion and gasification rates of lignocellulosic chars. *Progress in Energy and Combustion Science*, 35, 121-140.
- Diaz, C., Blanco, C. G. 2003. NMR: A powerful tool in the characterization of coal tar pitch. *Energy & Fuels*, 17, 907-913.
- Dybowski, C., Neue, G. 2002. Solid state Pb-207 NMR spectroscopy. *Progress in Nuclear Magnetic Resonance Spectroscopy*, 41, 153-170.
- EURACOAL. 2013. Country Profiles-Turkey. [Online]. [Accessed July 2013]. <http://www.euracoal.be/pages/layout1sp.php?idpage=475^>.

- Fan, L. S., Jadhav, R. A. 2002. Clean coal technologies: Oscar and Carbonox commercial demonstrations. *Aiche Journal*, 48, 2115-2123.
- Fan, L. S., Li, F. X., Ramkumar, S. 2008. Utilization of chemical looping strategy in coal gasification processes. *Particuology*, 6, 131-142.
- Fang, Z., Lin, X., Fan, Y. T., Liu, Y. F., Ni, Y. H., Wei, X. W. 2010. One-pot synthesis of PbSO<sub>4</sub>-sheathed PbS butterfly-like microstructures with high luminescence property. *Journal of Alloys and Compounds*, 493, L25-L28.
- Feng, B., Bhatia, S. K., Barry, J. C. 2003. Variation of the crystalline structure of coal char during gasification. *Energy & Fuels*, 17, 744-754.
- Francioso O., M. D. 2007. Diffuse reflectance Fourier transform spectroscopy and thermal analysis applied to humic substances. *Opt. Pura Apl.*, 40 207-213.
- Furlong, L. E., Nahas N. C. 1978. Exxon catalytic coal gasification process predevelopment. *Proceedings of the Tenth Synthetic Pipeline Gas Symposium*, October 1978.
- Gallagher, J. E., Marshall J R., H. A. 1978. Production of SNG from Illinois Coal via Catalytic Gasification A.I.Ch.E. Symposium on Reaction Engineering in Processing Solid Fossil Fuels, November 1978.
- Garcia-Labiano, F., De Diego, L. F., Gayan, P., Adanez, J., Abad, A., Dueso, C. 2009. Effect of fuel gas composition in chemical-looping combustion with ni-based oxygen carriers. 1. Fate of sulfur. *Industrial & Engineering Chemistry Research*, 48, 2499-2508.
- GASIFIPEDIA. 2013. Applications of Gasification [Online]. [Accessed July 2013]. [http://www.netl.doe.gov/technologies/coalpower/gasification/gasifipedia/6-apps/6-9\\_igfc.html](http://www.netl.doe.gov/technologies/coalpower/gasification/gasifipedia/6-apps/6-9_igfc.html).
- GCCSI. 2012. Brief description of major technologies for CO<sub>2</sub> capture, [Online]. [Accessed September 2013]. <http://www.globalccsinstitute.com/publications/technology-options-co2-capture/online/55316>.
- Genc, V. E., Altay, F. E., Uner, D. 2005. Testing molten metal oxide catalysts over structured ceramic substrates for diesel soot oxidation. *Catalysis Today*, 105, 537-543.
- Glatfelter, A., Bai, S., Dmitrenko, O., Perry, D. L., van Bramer, S. E., Dybowski, C. 2011. Solid-state Pb-207 nuclear magnetic resonance studies of adducts of 1,10-phenanthroline with lead(II) halides. *Canadian Journal of Chemistry-Revue Canadienne De Chimie*, 89, 863-869.
- Gue, E. 2012. Look Overseas For Growth in Coal [Online]. [Accessed July 2013]. <http://www.resourceinvestor.com/2012/06/15/look-overseas-for-growth-in-coal^>.

- Guin, J. A., Tarrer, A. R., Prather, J. W., Johnson, D. R., Lee, J. M. 1978. Effects of coal minerals on hydrogenation, desulfurization, and solvent-extraction of coal. *Industrial & Engineering Chemistry Process Design and Development*, 17, 118-126.
- Gunasekaran, S., Anbalagan, G. 2007. Thermal decomposition of natural dolomite. *Bulletin of Materials Science*, 30, 339-344.
- Gupta, R. 2007. Advanced coal characterization: A review. *Energy & Fuels*, 21, 451-460.
- Hinckley, M. 2013. The History of Coal Energy [Online]. [Accessed July, 2013]. [http://www.ehow.com/about\\_5455825\\_history-coal-energy.html](http://www.ehow.com/about_5455825_history-coal-energy.html)<sup>^</sup>
- Hippo, E. J., Tandon, D. 1996. Low temperature steam-coal gasification catalysts. *Abstracts of Papers of the American Chemical Society*, 211, 57-FUEL.
- Hirsch, R. L., Gallagher, J. E., Lessard, R. R., Wesselhoft, R. D. 1982. Catalytic coal-gasification - An emerging technology. *Science*, 215, 121-127.
- Hook, M., Aleklett, K. 2010. A review on coal-to-liquid fuels and its coal consumption. *International Journal of Energy Research*, 34, 848-864.
- IEA-International Energy Agency. 2012. Energy technology perspectives 2012. Pathways to a clean energy system
- Iglesias, M. J., De La Puente, G., Fuente, E., Pis, J. J. 1998. Compositional and structural changes during aerial oxidation of coal and their relations with technological properties. *Vibrational Spectroscopy*, 17, 41-52.
- Jensen, J. O. 2003. Vibrational frequencies and structural determinations of Pb<sub>6</sub>O(OH)(6)(4+). *Journal of Molecular Structure-Theochem*, 635, 11-24.
- Journal of Physical Chemistry Reference Data, Monograph.
- Kabe, T., Ishihara, A., Qian, E. W., Sutrisna, I. P., Kabe, Y. 2004a. Coal and coal-related compounds - Structures, reactivity and catalytic reactions. *Studies in Surface Science and Catalysis*
- Kabe, T., Ishihara, A., Qian, E. W., Sutrisna, I. P., Kabe, Y. 2004b. Gasification of Coal. *Studies in Surface Science and Catalysis*
- Kalaitzidis, S., Georgakopoulos, A., Christanis, K., Iordanidis, A. 2006. Early coalification features as approached by solid state C-13 CP/MAS NMR spectroscopy. *Geochimica Et Cosmochimica Acta*, 70, 947-959.
- Kalina, T., Nahas N. C., 1978. Exxon catalytic coal gasification process research and development. Final Project Report (5360-001GF), December 1978.
- Kar, S., Chaudhuri, S. 2005. Synthesis of highly oriented iron sulfide nanowires through solvothermal process. *Materials Letters*, 59, 289-292.

- Karakosta, C., C. Pappas, 2013. Renewable energy and nuclear power towards sustainable development: Characteristics and prospects. *Renewable and Sustainable Energy Reviews* 22, 187–197.
- Keeler, C., Maciel, G. E. 2000. <sup>13</sup>C NMR spectral editing of humic material. *Journal of Molecular Structure*, 550, 297-305.
- Kelemen, S. R., Afeworki, M., Gorbaty, M. L., Cohen, A. D. 2002. Characterization of organically bound oxygen forms in lignites, peats, and pyrolyzed peats by X-ray photoelectron spectroscopy (XPS) and solid-state C-13 NMR methods. *Energy & Fuels*, 16, 1450-1462.
- Kim, H. R., Wang, D. W., Zeng, L., Bayham, S., Tong, A., Chung, E., Kathe, M. V., Luo, S. W., McGivern, O., Wang, A. N., Sun, Z. C., Chen, D., Fan, L. S. 2013. Coal direct chemical looping combustion process: Design and operation of a 25-kW(th) sub-pilot unit. *Fuel*, 108, 370-384.
- Kirk-Othmer 2002a. *Coal*. Encyclopedia of Chemical Technology. John Wiley & Sons.
- Kirk-Othmer 2002b. *Coal Gasification* Encyclopedia of Chemical Technology. John Wiley & Sons.
- Kovacik, G., Chambers, A., Ozum, B. 1991. CO<sub>2</sub> gasification kinetics of 2 Alberta coal chars. *Canadian Journal of Chemical Engineering*, 69, 811-815.
- Kucukbayrak, S., Haykiri-Acma, H., Ersoy-Mericboyu, A., Yaman, S. 2001. Effect of lignite properties on reactivity of lignite. *Energy Conversion and Management*, 42, 613-626.
- Kuznetsov, B. N. 2009. Catalytic methods in coal processing to syn-gas, carboneous and liquid fuels contributing to sustainable development. *International Journal of Hydrogen Energy*, 34, 7057-7063.
- Lavat, A., Grasselli, M. C., Lovecchio, E. G. 2011. Characterization of the Firing Steps and Phases Formed in Mg-Zr-Containing Refractory Dolomitic Materials. In: SIKALIDIS, P. C. (ed.) *Advances in Ceramics - Characterization, Raw Materials, Processing, Properties, Degradation and Healing*.
- Lee, S. J. G. S., Loyalka, S. K. 2007. *Gasification of Coal*. (ed.) Handbook of Alternative Fuel Technology. CRC Press 2007.
- Li, L. G., Tang, Y. 2007. Controllable synthesis of ZnS holey microspheres in solution containing ethylenediamine and CS<sub>2</sub>. *Journal of Materials Science*, 42, 7245-7250.
- Li, W., Doblinger, M., Vaneski, A., Rogach, A. L., Jackel, F., Feldmann, J. 2011. Pyrite nanocrystals: Shape-controlled synthesis and tunable optical properties via reversible self-assembly. *Journal of Materials Chemistry*, 21, 17946-17952.
- Li, Y., Cao, X. Y., Zhu, D. Q., Chappell, M. A., Miller, L. F., Mao, J. D. 2012. Characterization of coals and their laboratory-prepared black carbon using advanced solid-state C-13 nuclear magnetic resonance spectroscopy. *Fuel Processing Technology*, 96, 56-64.

- Liu, Y. H., Meng, L., Zhang, L. 2005. Optical and electrical properties of FeS<sub>2</sub> thin films with different thickness prepared by sulfurizing evaporated iron. *Thin Solid Films*, 479, 83-88.
- Lopes, I., El Hassan, N., Guerba, H., Wallez, G., Davidson, A. 2006. Size-induced structural modifications affecting Co<sub>3</sub>O<sub>4</sub> nanoparticles patterned in SBA-15 silicas. *Chemistry of Materials*, 18, 5826-5828.
- Lowson, R. T. 1982. Aqueous oxidation of pyrite by molecular-oxygen. *Chemical Reviews*, 82, 461-497.
- Lu, L. M., Kong, C. H., Sahajwalla, V., Harris, D. 2002. Char structural ordering during pyrolysis and combustion and its influence on char reactivity. *Fuel*, 81, 1215-1225.
- Lu, L. M., Sahajwalla, V. & Harris, D. 2001. Coal char reactivity and structural evolution during combustion - Factors influencing blast furnace pulverized coal injection operation. *Metallurgical and Materials Transactions B-Process Metallurgy and Materials Processing Science*, 32, 811-820.
- Maity, S., Mukherjee, P. 2006. X-ray structural parameters of some Indian coals. *Current Science*, 91, 337-340.
- Mao, J. D., Schimmelmann, A., Mastalerz, M., Hatcher, P. G., Li, Y. 2010. Structural features of a bituminous coal and their changes during low-temperature oxidation and loss of volatiles investigated by advanced solid-state NMR spectroscopy. *Energy & Fuels*, 24, 2536-2544.
- Maurstad, O. 2005. An Overview of Coal based Integrated Gasification Combined Cycle (IGCC) Technology [Online]. [http://sequestration.mit.edu/pdf/LFEE\\_2005-002\\_WP.pdf](http://sequestration.mit.edu/pdf/LFEE_2005-002_WP.pdf) [Accessed July, 2013].
- Meng, L., Liu, Y. H., Tian, L. 2003. Evolutions of structure, composition and optical absorption behavior of pyrite films formed by sulfurating iron. *Materials Research Bulletin*, 38, 941-948.
- Meyers, R. (ed.) 1982. *Coal Structure*: New York: Academic Press
- Minchener, A. J. 2005. Coal gasification for advanced power generation. *Fuel*, 84, 2222-2235.
- Mishra, V. S., Mahajani, V. V., Joshi, J. B. 1995. Wet air oxidation. *Industrial & Engineering Chemistry Research*, 34, 2-48.
- Molina, A., Mondragon, F. 1998. Reactivity of coal gasification with steam and CO<sub>2</sub>. *Fuel*, 77, 1831-1839.
- Mursito, A. T., Hirajima, T., Sasaki, K. 2011. Alkaline hydrothermal de-ashing and desulfurization of low quality coal and its application to hydrogen-rich gas generation. *Energy Conversion and Management*, 52, 762-769.

- Nahas, N. C. 1983. Exxon catalytic coal-gasification process - Fundamentals to flowsheets. *Fuel*, 62, 239-241.
- Nahas, N. C., Gallagher J. E. 1978. Catalytic gasification predevelopment research. Exxon Research and Engineering Company, August 1978.
- Nanda, J., Sapra, S., Sarma, D. D., Chandrasekharan, N., Hodes, G. 2000. Size-selected zinc sulfide nanocrystallites: Synthesis, structure, and optical studies. *Chemistry of Materials*, 12, 1018-1024.
- NETL. 2010. Worldwide Gasification Database [Online]. [Accessed July 2013]. [http://www.netl.doe.gov/technologies/coalpower/gasification/worlddatabase/2010\\_Worldwide\\_Gasification\\_Database.pdf](http://www.netl.doe.gov/technologies/coalpower/gasification/worlddatabase/2010_Worldwide_Gasification_Database.pdf).
- Neue, G., Dybowski, C., Smith, M. L., Hepp, M. A., Perry, D. L. 1996. Determination of Pb-207(2+) chemical shift tensors from precise powder lineshape analysis. *Solid State Nuclear Magnetic Resonance*, 6, 241-250.
- Orem, W. H., Neuzil, S. G., Lerch, H. E., Cecil, C. B. 1996. Experimental early-stage coalification of a peat sample and a peatified wood sample from Indonesia. *Organic Geochemistry*, 24, 111-125.
- Pawar, S. B., Shaikh, J. S., Devan, R. S., Ma, Y. R., Haranath, D., Bhosale, P. N., Patil, P. S. 2011. Facile and low cost chemosynthesis of nanostructured PbS with tunable optical properties. *Applied Surface Science*, 258, 1869-1875.
- Peuravuori, J., Zbankova, P., Pihlaja, K. 2006. Aspects of structural features in lignite and lignite humic acids. *Fuel Processing Technology*, 87, 829-839.
- Robinson, K. K. 2009. Reaction Engineering of Direct Coal Liquefaction. *Energies*, 2, 976-1006.
- Saikia, B. K., Boruah, R. K., Gogoi, P. K. 2007a. FT-IR and XRD analysis of coal from Makum coalfield of Assam. *Journal of Earth System Science*, 116, 575-579.
- Saikia, B. K., Boruah, R. K., Gogoi, P. K. 2007b. XRD and FT-IR investigations of sub-bituminous Assam coals. *Bulletin of Materials Science*, 30, 421-426.
- Sekine, Y., Ishikawa, K., Kikuchi, E., Matsukata, M., Akimoto, A. 2006. Reactivity and structural change of coal char during steam gasification. *Fuel*, 85, 122-126.
- Sharma, A., Saito, I., Takanohashi, T. 2009. Effect of steam partial pressure on gasification rate and gas composition of product gas from catalytic steam gasification of hypercoal. *Energy & Fuels*, 23, 4887-4892.
- Sharma, A., Takanohashi, T., Morishita, K., Takarada, T., Saito, I. 2008. Low temperature catalytic steam gasification of HyperCoal to produce H<sub>2</sub> and synthesis gas. *Fuel*, 87, 491-497.
- Shen, L. H., Zheng, M., Xiao, J., Zhang, H., Xiao, R. 2007. Chemical looping combustion of coal in interconnected fluidized beds. *Science in China Series E-Technological Sciences*, 50, 230-240.

- Shen, X. P., Miao, H. J., Zhao, H., Xu, Z. 2008. Synthesis, characterization and magnetic properties of  $\text{Co}_3\text{O}_4$  nanotubes. *Applied Physics a-Materials Science & Processing*, 91, 47-51.
- Sheth, A., Yeboah, Y. D., Godavarty, A., Xu, Y., Agrawal, P. K. 2003. Catalytic gasification of coal using eutectic salts: reaction kinetics with binary and ternary eutectic catalysts. *Fuel*, 82, 305-317.
- Simpson, M. J., Hatcher, P. G. 2004. Determination of black carbon in natural organic matter by chemical oxidation and solid-state C-13 Nuclear Magnetic Resonance spectroscopy. *Organic Geochemistry*, 35, 923-935.
- Siriwardane, R., Tian, H. J., Richards, G., Simonyi, T., Poston, J. 2009. Chemical-looping combustion of coal with metal oxide oxygen carriers. *Energy & Fuels*, 23, 3885-3892.
- Skodras, G., Sakellaropoulos, G. P. 2002. Mineral matter effects in lignite gasification. *Fuel Processing Technology*, 77, 151-158.
- Speight, J. G. 2005. *Handbook of Coal Analysis*, New Jersey, Hoboken Wiley-Interscience.
- Spitz, N. 2004. Coal Combustion [Online]. [Accessed September 2013].  
[http://www.slidefinder.net/c/coal\\_combustion/presentation12jan04/15510467](http://www.slidefinder.net/c/coal_combustion/presentation12jan04/15510467).
- Sutcu, H., Toroglu, I., Piskin, S. 2005. Structural characterization of oil component of high temperature pyrolysis tars. *Energy Sources*, 27, 521-534.
- Uner, D., Demirkol, M. K., Dernaika, B. 2005. A novel catalyst for diesel soot oxidation. *Applied Catalysis B-Environmental*, 61, 334-345.
- Van Bramer, S. E., Glatfelter, A., Bai, S., Dybowski, C., Neue, G., Perry, D. L. 2006. Solid-state Pb-207 NMR studies of lead-group 16 and mixed transition-metal/lead-group 16 element-containing materials. *Magnetic Resonance in Chemistry*, 44, 357-365.
- Van Dyk, J. C., Keyser, M. J., Coertzen, A. 2006. Syngas production from South African coal sources using Sasol-Lurgi gasifiers. *International Journal of Coal Geology*, 65, 243-253.
- Van heek, K. H. 2000. Progress of coal science in the 20th century. *Fuel*, 79, 1-26.
- Veras, C. C., Ja; Ferreira, Ma 2002 The chemical percolation devolatilization model applied to the devolatilization of coal in high intensity acoustic fields. *Journal of the Brazilian Chemical Society*, 13, 358-367.
- Wan, D. Y., Wang, B. Y., Wang, Y. T., Sun, H., Zhang, R. G., Wei, L. 2003. Effects of the sulfur pressure on pyrite  $\text{FeS}_2$  films prepared by sulfurizing thermally iron films. *Journal of Crystal Growth*, 257, 286-292.

- Wang, C. L., Zhang, P., Chen, Y. H., Pan, J. Y., Wang, J., Qi, J. Y., Li, X. P., Liu, J. A. 2010a. Study on the purification property of pyrite and its spectra on the processing of metal-bearing wastewater. *Environmental Earth Sciences*, 61, 939-945.
- Wang, H., Dlugogorski, B. Z., Kennedy, E. M. 2003. Coal oxidation at low temperatures: oxygen consumption, oxidation products, reaction mechanism and kinetic modelling. *Progress in Energy and Combustion Science* 29, 487-513.
- Wang, J., Yao, Y. H., Cao, J. Q., Jiang, M. Q. 2010b. Enhanced catalysis of  $K_2CO_3$  for steam gasification of coal char by using  $Ca(OH)_2$  in char preparation. *Fuel*, 89, 310-317.
- Weidenthaler, C. 2011. Pitfalls in the characterization of nanoporous and nanosized materials. *Nanoscale*, 3, 792-810.
- Weller, S., Pelipetz, M. G. 1951. Coal hydrogenation catalysts - studies of catalyst distribution. *Industrial and Engineering Chemistry*, 43, 1243-1246.
- Weller, S., Pelipetz, M. G., Friedman, S. 1951. Kinetics of coal hydrogenation - conversion of asphalt. *Industrial and Engineering Chemistry*, 43, 1572-1575.
- Weller, S., Pelipetz, M. G., Friedman, S., Storch, H. H. 1950. Coal hydrogenation catalysts - batch autoclave tests. *Industrial and Engineering Chemistry*, 42, 330-334.
- Wilson, M. J. 1987. *A handbook of determinative methods in clay mineralogy*. , New York, Blackie & Son Ltd.
- Wu, J. G. 1994. *Technology and application of modern FTIR spectroscopy*. Science and Technology Literature Press. Beijing, Chinese.
- Xiang, J. H., Yu, S. H., Geng, X., Liu, B. H., Xu, Y. 2005. Growth of  $PbSO_4$  single-crystal nanorods and optical properties by a microemulsion approach. *Crystal Growth & Design*, 5, 1157-1161.
- Xu, W. C., Kumagai, M. 2003. Sulfur transformation during rapid hydrolysis of coal under high pressure by using a continuous free fall pyrolyzer. *Fuel*, 82, 245-254.
- Yaman, S., Kucukbayrak, S. 1997. Sulfur removal from lignite by oxydesulfurization using fly ash. *Fuel*, 76, 73-77.
- Yeboah, Y. D., Sheth A., Agrawal P. 1998. Catalytic gasification of coal using eutectic salt mixtures. *Semi-Annual Report October 1997 - March 1998*.
- Yeboah, Y. D., Xu, Y., Sheth, A., Godavarty, A., Agrawal, P. K. 2003. Catalytic gasification of coal using eutectic salts: identification of eutectics. *Carbon*, 41, 203-214.
- Yung, M. M., Zhao, Z. K., Woods, M. P., Ozkan, U. S. 2008. Preferential oxidation of carbon monoxide on  $CoO_x/ZrO_2$ . *Journal of Molecular Catalysis a-Chemical*, 279, 1-9.

- Zafar, Q., Mattisson, T., Gevert, B. 2005. Integrated hydrogen and power production with CO<sub>2</sub> capture using chemical-looping reforming-redox reactivity of particles of CuO, Mn<sub>2</sub>O<sub>3</sub>, NiO, and Fe<sub>2</sub>O<sub>3</sub> using SiO<sub>2</sub> as a support. *Industrial & Engineering Chemistry Research*, 44, 3485-3496.
- Zhang, J. G., Lund, J. C., Cirignano, L., Shah, K. S., Squillante, M. R. 1994. Lead sulfate scintillator crystal-growth for pet applications. *Ieee Transactions on Nuclear Science*, 41, 669-674.
- Zhang, Y., Ashizawa, M., Kajitani, S., Hara, S. 2010. A new approach to catalytic coal gasification: The recovery and reuse of calcium using biomass derived crude vinegars. *Fuel*, 89, 417-422.
- Zhang, Y. H., Guo, L., Yin, P. G., Zhang, R., Zhang, Q., Yang, S. H. 2007. A highly regular hexapod structure of lead sulfide: Solution synthesis and Raman spectroscopy. *Chemistry-a European Journal*, 13, 2903-2907.
- Zhao, P. D., Prasad, S., Huang, J., Fitzgerald, J. J., Shore, J. S. 1999. Lead-207 NMR spectroscopic study of lead-based electronic materials and related lead oxides. *Journal of Physical Chemistry B*, 103, 10617-10626.

## APPENDIX A

### STANDARD GIBBS FREE ENERGY OF FORMATION DATA FOR RELEVANT COMPOUNDS

Table A.1. Standard Gibbs free energy of formation CoO, CO, H<sub>2</sub>O, CO<sub>2</sub>, and PbO.

(Journal of Physical Chemistry Reference Data)

T (K)	$\Delta G^f$ (J/mol) (CoO)	$\Delta G^f$ (CO)	$\Delta G^f$ (H <sub>2</sub> O)	$\Delta G^f$ (CO <sub>2</sub> )	$\Delta G^f$ (PbO)
298,15	-214.2	-137.2	-228.6	-394.4	-188.6
300	-214.1	-137.3	-228.5	-394.4	-188.5
400	-206.3	-146.4	-224.0	-394.6	-178.7
500	-198.9	-155.4	-219.1	-394.9	-169.0
600	-191.6	-164.5	-214.1	-395.1	-159.5
700	-184.5	-173.5	-208.9	-395.3	-149.3
800	-177.5	-182.5	-203.6	-395.5	-139.2
900	-170.5	-191.4	-198.2	-395.7	-129.2
1000	-163.5	-200.3	-192.7	-395.8	-119.3
1100	-156.6	-209.1	-187.2	-395.9	-109.5
1200	-149.7	-217.8	-181.6	-396.0	-100.7
1300	-142.7	-226.5	-175.9	-396.1	-93.4
1400	-135.7	-235.1	-170.3	-396.1	-86.2
1500	-128.6	-243.7	-164.6	-396.2	-79.1
1600	-121.6	-252.3	-158.8	-396.2	-72.2
1700	-114.6	-260.8	-153.1	-396.2	-65.3
1800	-107.3	-269.2	-147.3	-396.2	-58.6

Table A.2. Standard Gibbs free energy of formation of SO<sub>3</sub>, SO<sub>2</sub>, and PbS.

(Journal of Physical Chemistry Reference Data)

T (K)	$\Delta G^f$ (kJ/mol) (SO <sub>3</sub> )	$\Delta G^f$ (SO <sub>2</sub> )	$\Delta G^f$ (PbS)
298,15	-300.1	-371.0	-97.0
300	-300.1	-370.9	-96.9
400	-300.9	-362.2	-96.3
500	-300.8	-352.7	-95.0
600	-300.2	-342.7	-93.4
700	-299.4	-332.4	-90.7
800	-298.4	-321.9	-87.9
900	-295.9	-310.2	-83.9
1000	-288.6	-293.5	-75.0
1100	-281.3	-277.0	-66.2

## APPENDIX B

### MASS TRANSFER EFFECT

#### B.1. Pore diffusion effects: Constant $N_2$ flow rate $v=200$ cc/min

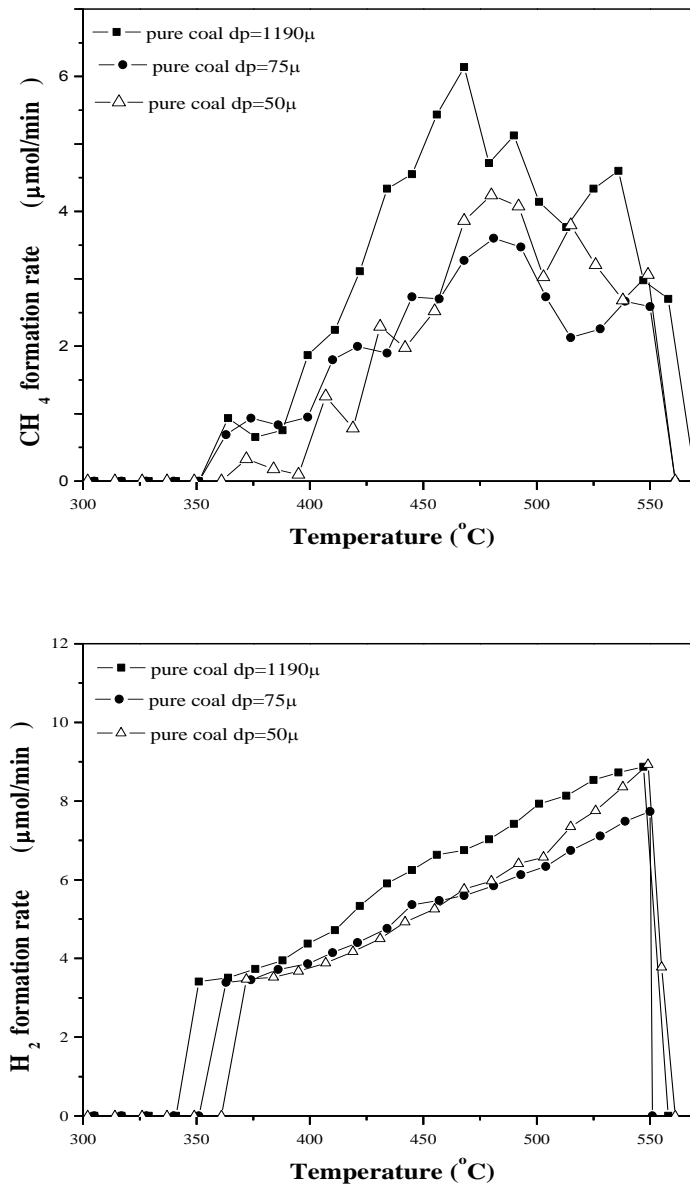


Figure B.1. Pore diffusion effects on  $CH_4$  (a) and  $H_2$  (b) formation rates for different particle sizes.

In order to investigate the pore diffusion effect, different particle size experiments were performed. In Figure B.1, CH<sub>4</sub> and H<sub>2</sub> formation rates were shown under non-isothermal condition for three different particle sizes. Especially H<sub>2</sub> formation rate vs. time graph exhibits that pore diffusion effect is unimportant.

### B.2. External mass transfer effects

External mass transfer effect was investigated in the temperature range of 300 to 550°C for 75μ particle size. Figure B.2a, similar to Figure B.2b, demonstrates that volumetric flow rate of 200 cc/min. is relatively best one.

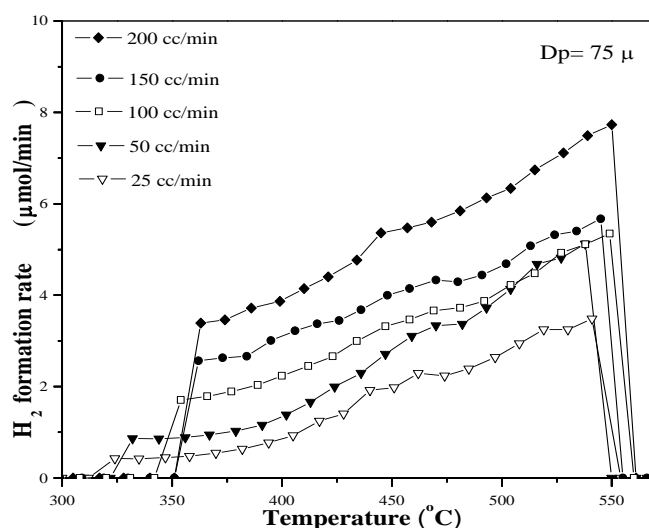
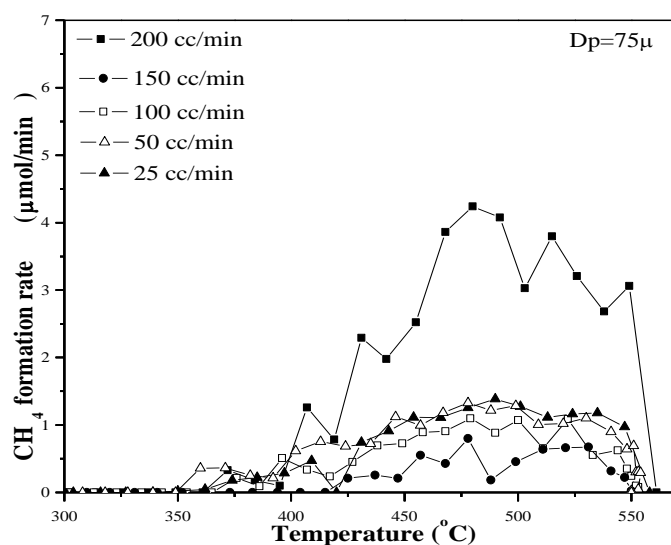


Figure B.2. (a) CH<sub>4</sub> and (b) H<sub>2</sub> formation rates under non-isothermal condition and different flow rates.

## APPENDIX C

### CURVE FITTING

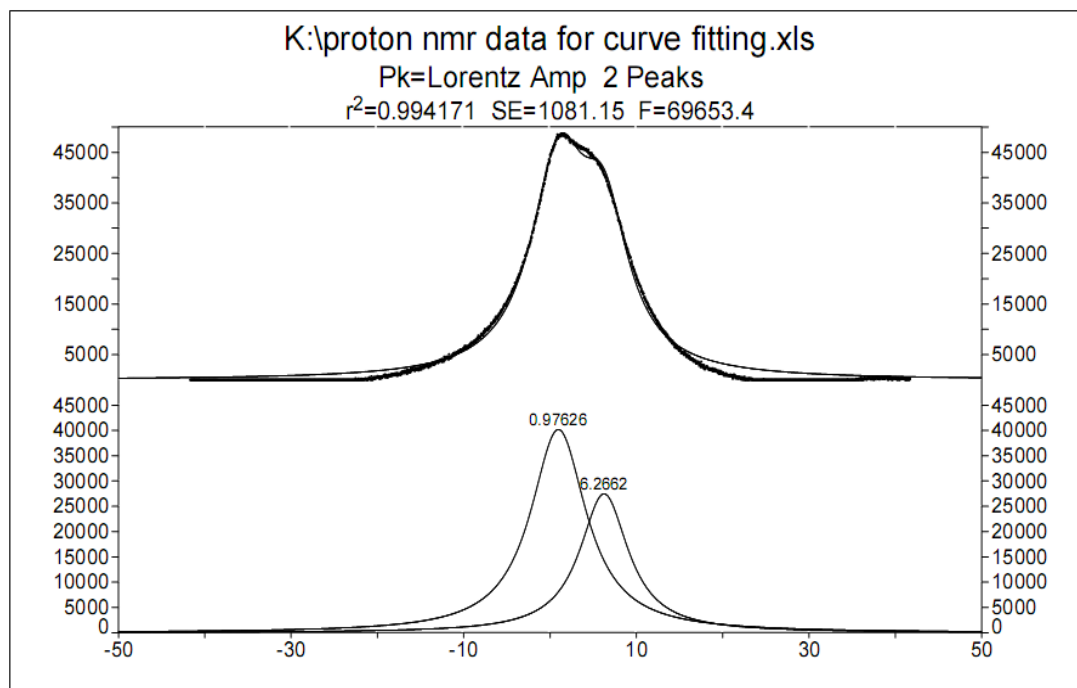


Figure C.1. Curve fitting data for proton NMR data of unprocessed Tuncbilek lignites.

Description: K:\proton nmr data for curve fitting.xls  
 File Source: k:\proton nmr data for curve fitting.xls

#### Fitted Parameters

r <sup>2</sup>	Coef Det	DF	Adj r <sup>2</sup>	Fit Std Err	F-value
0.99417086	0.99415373			1081.15165	69653.4490
Peak	Type	a <sub>0</sub>	a <sub>1</sub>	a <sub>2</sub>	
1	Lorentz Amp	40194.9018	0.97625930	3.92637799	
2	Lorentz Amp	27485.3990	6.26624950	3.42442739	

#### Measured Values

Peak	Type	Amplitude	Center	FWHM	Asym50	Int Area	% Area
1	Lorentz Amp	40194.9018	0.97625927	7.85275597	1.00000001	4.6614e+05	62.4812806
2	Lorentz Amp	27485.3990	6.26624950	6.84885479	1.00000000	2.7991e+05	37.5187194
Total						7.4605e+05	100.000000

<sup>1</sup>H-NMR spectrum of unprocessed coal was obtained by fitting the experimental data to Lorentz equation. Coefficients of the equation were reported under the fitted parameters title.

## APPENDIX D

### $^{207}\text{Pb}$ -NMR SPECTROSCOPY

#### $^{207}\text{Pb}$ MAS-NMR for the Determination of the Pulse Width and Spin-Lattice Relaxation Time

The  $^{207}\text{Pb}$  NMR experiment was performed on a Lap-NMR spectrometer using an external magnetic field of 1.8 T. Spin lattice relaxation time was calculated to be 7.4 s, while pulse length was determined as 1.4  $\mu\text{s}$  for the  $\text{Pb}(\text{NO}_3)_2$  powder.

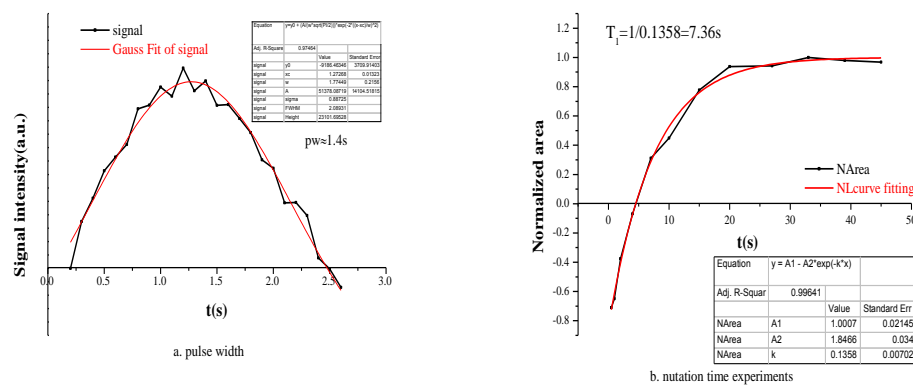


Figure D.1. Pulse length (a) and nutation time (b) experiments.

## APPENDIX E

### SAMPLE CALCULATION FOR SULFUR COMPOSITION

Total sulfur of Tuncbilek lignite by Eschka method:

Initial weight of sample (g)	Weight of BaSO <sub>4</sub> (g)
1.04	0.31
1.01	0.28

$$\text{Total sulfur \%} = \frac{\text{Weight of BaSO}_4 \text{ (g)}}{\text{Weight of coal sample (g)}} \times \frac{32 \text{ g/mol sulfur}}{234 \text{ g/mol BaSO}_4} \times 100 \dots\dots(\text{Eqn. 1})$$

S% of sample 1 = 4.09%

S% of sample 2 = 3.81%

Average sulfur% of two measurements = 3.9%

Sulfate content of Tuncbilek lignite:

Initial weight of sample (g)	Weight of BaSO <sub>4</sub> (g)
1.73	0.16
1.59	0.13

$$\text{Total sulfur \%} = \frac{\text{Weight of BaSO}_4 \text{ (s)}}{\text{Weight of coal sample (g)}} \times \frac{32 \text{ g/mol sulfur}}{234 \text{ g/mol BaSO}_4} \times 100 \dots\dots(\text{Eqn. 1})$$

Sulfate% of sample 1 = 1.26%

Sulfate% of sample 2 = 1.14%

Average sulfate% of two measurements = 1.2%

Pyritic sulfur content of Tuncbilek lignite:

Initial weight of sample (g)	Titrant (KMnO <sub>4</sub> ) volume (ml)
1.73	33.5
1.59	33.8

$$\text{Pyritic sulfur \%} = \frac{V_{\text{KMnO}_4} \times 10^{-3}(\text{l}) \times N_{\text{KMnO}_4}}{\text{Weight of coal sample (g)}} \times \frac{56 \text{ g Fe}}{1 \text{ N KMnO}_4} \times \frac{64 \text{ g S}_2}{56 \text{ g Fe}} \times 100 \dots\dots(\text{Eqn. 2})$$

$N_{KMnO_4} = 0.02$

Pyritic sulfur% of sample 1 = 2.48%

Pyritic sulfur% of sample 2 = 2.72%

Average pyritic sulfur% of two measurements = 2.6%

Organic sulfur content of Tuncbilek lignite:

Organic sulfur % = total sulfur – (pyritic sulfur + sulfate) ... (Eqn. 3)

Average organic sulfur% of two measurements =  $3.9 - (2.6 + 1.2) = 0.1\%$

## APPENDIX F

### SAMPLE CALCULATION FOR CARBON CONVERSION

Sample calculation is conducted for Tuncbilek lignite sample during air oxidation.

Sample name	CH <sub>4</sub> ( $\mu\text{mol/gcoal}$ )	CO ( $\mu\text{mol/gcoal}$ )	CO <sub>2</sub> ( $\mu\text{mol/gcoal}$ )	$\Sigma$ C ( $\mu\text{mol/gcoal}$ )	C conversion (%)
Pure Coal	81.6	3316.4	37106.9	40504.9	121.5

Initial amount of coal= 0.502g

Total carbon percentages of coal  $\approx$  40% (37.7  $\pm$  0.7% carbon in Table 4.3)

Final amount of carbon = 40504.9  $\mu\text{molC/gcoal}$  \* 12.10<sup>-6</sup> g C/ $\mu\text{mol C}$  =

0.486 gC/gcoal

Carbon conversion = (0.486:0.40) \* 100 = 121.5%

## CURRICULUM VITAE

### PERSONAL INFORMATION

Surname, Name: Kanca, Arzu

Nationality: Turkish (TC)

Date and place of Birth: 13.07.1977 (Erzurum, Turkey)

Phone: +90 (505) 4688048

Email Address: akanca@metu.edu.tr

### EDUCATION

Degree	Institution/ Department	Year of Graduation
M. Sc.	Atatürk University, Department of Chemistry Education	2003
B. Sc.	Atatürk University, Department of Chemical Engineering	2000

### WORK EXPERIENCE

Enrollment	Institution/ Department	Year
Teaching assistant	METU-Chemical Engineering Department	2004-present

### Languages

English

Turkish (mother language)

### Publications

Articles in preparation

A.Kanca, D.Uner, Chemical Looping Characteristic of Co-Pb mixed metal oxides.

A. Kanca, D. Uner, Sulfur Removal Characteristics of Tuncbilek Lignite in the Presence and Absence of PbO and ZnO.

A. Kanca, M. Datt, J. A. Reimer, and D. Uner, An Advanced Spectroscopic Approach for the Characterization of Structure and Reactivity of Tuncbilek Lignite.

#### **Presented at international conferences**

**A. Kanca**, D. Uner, “Sulfur Removal of Tuncbilek Lignite by Pyrolysis and Hydrogenation”, Eighth Mediterranean Combustion Symposium, September 8-13, 2013, Çeşme, Izmir, Turkey,

**A. Kanca**, D. Uner, “Desulfurization Behavior of Turkish Lignite By Hydrogenation and Hydrothermal Processes”, 2012 International Pittsburgh Coal Conference, October 15 - 18, 2012 Pittsburgh, PA, USA.

**A. Kanca**, A. Çalışan, D. Uner, “N<sub>2</sub> gasification and CO<sub>2</sub> Reforming of Turkish Lignite in the Presence of Co and Pb Based Catalyst”, EuropaCat X, August 28- Sept 2, 2011, Glasgow, Scotland.

M.Can, **A. Kanca**, C. Hess, D. Uner, “Raman Characterization of Co-Pb Based Catalyst”, Energy Challenges for Advanced Materials and Processes: Harvesting, Storage and Efficient Utilization, May 25-29, 2011, Dedeman Hotel-Cappadocia, Turkey.

**A. Kanca**, D. Uner, “Catalytic Activity of Co-Pb Mixed Metal Oxide on the Lignite Gasification”, 9<sup>th</sup> Novel Gas Conversion Symposium, May 30- June 3, 2010, Cité Internationale Congress Center, Lyon, France.

**A. Kanca**, D. Uner, “The Selection of Reaction Parameters on the Gasification Products Selectivity”, EFCATS summer school, September 13-19, 2010, Gumuldur Izmir, Turkey.

**A. Kanca**, D. Uner, “Catalytic CO<sub>2</sub> reforming of Turkish Coal”, 6<sup>th</sup> Chemical Engineering Conference for Collaborative Research in Eastern Mediterranean Countries (EMCC-6), March 7-12, 2010, Atlantis Hotel, Belek, Antalya, Turkey.

**A. Kanca**, D. Uner, “Catalytic Gasification of Turkish Coal”, EuropaCat IX, August 30, September 4, 2009, Salamanca, Spain.

#### **Presented at national conferences**

**A. Kanca**, D. Uner, “Oxidation and Desulfurization Behaviors of Turkish Lignite in the Presence of Co-Pb Based Metal Oxide Catalysts”, 4<sup>th</sup> National Catalysis Conference (NCC 4), March 21-24, 2012, Kocaeli, Turkey.

**A. Kanca**, D. Uner, “Catalytic Synergy between the Cobalt and Lead Oxides during Gasification of Turkish Lignites”, 3<sup>rd</sup> National Catalysis Conference (NCC 3), April 28-May 1, 2010, Zonguldak, Turkey.

**A. Kanca**, D. Uner, “Intrinsic and Extrinsic Catalysis for Lignite Gasification”, 2<sup>nd</sup> National Catalysis Conference (NCC 2), June 18-21, 2008, Palan Hotel, Palandöken, Turkey.

**A. Kanca**, D. Uner, “Thermodynamics of Catalytic Coal Gasification with Co-Pb Mixed Metal Oxides”, 1<sup>st</sup> National Catalysis Conference (NCC 1), January 17-21, 2007, Güzelyurt, Northern Cyprus.

## **References**

Prof. Dr. Deniz Üner  
Department of Chemical Engineering, METU  
06800 Çankaya, Ankara, Turkey  
Tel: + 90 (312) 210 2601  
Fax: +90 (312) 210 2600  
e-mail: uner@metu.edu.tr

Prof. Dr. İsmail Tosun  
Department of Chemical Engineering, METU  
06800 Çankaya, Ankara, Turkey  
Tel: + 90 (312) 210 2637  
Fax: +90 (312) 210 2600  
e-mail: itosun@metu.edu.tr